UC Riverside

UC Riverside Electronic Theses and Dissertations

Title

Plasma-Induced Surface Engineering of Magnesium Nanoparticles for Designing Nano-Energetics with Specific Chemistry

Permalink

https://escholarship.org/uc/item/1w217397

Author

Wagner, Brandon

Publication Date

2024

Supplemental Material

https://escholarship.org/uc/item/1w217397#supplemental

Peer reviewed|Thesis/dissertation

eScholarship.org Powered by the California Digital Library
University of California

UNIVERSITY OF CALIFORNIA
RIVERSIDE

Plasma-Induced Surface Engineering of Magnesium Nanoparticles for Designing Nano-Energetics with Specific Chemistry

A Dissertation submitted in partial satisfaction
of the requirements for the degree of

Doctor of Philosophy

in

Materials Science and Engineering

by

Brandon Alan Wagner

September 2024

Dissertation Committee:
Dr. Lorenzo Mangolini, Chairperson
Dr. Michael R. Zachariah
Dr. Huinan Liu

Copyright by
Brandon Alan Wagner
2024

The Dissertation of Brandon Alan Wagner is approved:

_____

_____

_____

Committee Chairperson

University of California, Riverside

Acknowledgements:

Thank you to:

My Fiancée and soon to be wife for always providing me the love and support I needed throughout my graduate academic life and giving me the confidence to accomplish my goals.

My family for always being proud of my accomplishments and being there for me through the hard times.

My labmate Minseok Kim for being not only a person to lean on in the lab, but for the cherishable times we shared throughout our journey in the PhD program.

My labmate Emmanuel Vidales for being the engineer sergeant that helped with many tasks in the lab, and for being a close friend to talk to.

My senior labmate Joseph Schwan for giving me guidance to become independent within the lab.

My collaborators Pankaj Ghildiyal, Feiyu Xu, and Mahbub Chowdhury for being mentors as well as awesome partners on the energetic experiments.

I am sincerely thankful for the collaboration established with Dr. Michael R. Zachariah, in which I have learned a lot about energetics from him and his lab students, providing me with the necessary fundamentals to carry out my experiments.

I am deeply grateful to my mentor and PhD advisor, Dr. Lorenzo Mangolini, for taking a chance on me as a PhD student, for providing me with the necessary skills to conduct research and contribute to the scientific community, and for being the ideal mentor I needed to become a professional.

I acknowledge the financial support from the University of California, Riverside via the Dean's Distinguished Fellowship, the Graduate Assistance in Areas of National Need (GAAN) Fellowship, and the Dissertation Completion Fellowship Award (DCFA).

I acknowledge the financial support from the Defense Threat Reduction Agency (DTRA) and Materials Science in Extreme Environments (MSEE) grant and collaboration.

Acknowledgement of Previously Published Papers:

The text of this dissertation contains works, in part or in full, reprinted from the following materials:

In-Flight Synthesis of Core–Shell Mg/Si–SiO_x Particles with Greatly Reduced Ignition Temperature published in *2023* within *Advanced Functional Materials*, Volume 33, Issue 21. I share primary co-authorship with *Pankaj Ghildiyal*. The co-authors are *Prithhwish Biswas, Mahbub Chowdhury, Michael R. Zachariah, and Lorenzo Mangolini*. The research has been entirely reprinted and adapted within the dissertation as **Section 3**.[1]

Enhancing the Combustion of Magnesium Nanoparticles via Low-Temperature Plasma-Induced Hydrogenation published in *2023* within *ACS Applied Materials and Interfaces*, Volume 15, Issue 44. I share primary co-authorship with *Minseok Kim*. The co-authors are *Mahbub Chowdhury, Emmanuel Vidales Pasos, Kimberly Hizon, Pankaj Ghildiyal, Michal R. Zachariah, and Lorenzo Mangolini*. The research has been entirely reprinted and adapted within the dissertation as **Section 4**.[2]

ABSTRACT OF THE DISSERTATION

Plasma-Induced Surface Engineering of Magnesium Nanoparticles for Designing Nano-Energetics with Specific Chemistry

by

Brandon Alan Wagner

Doctor of Philosophy, Graduate Program in Materials Science and Engineering
University of California, Riverside, September 2024
Dr. Lorenzo Mangolini, Chairperson

Non-thermal plasmas are non-equilibrium plasmas in which the temperature of the electrons is substantially hotter than ions and neutral species. With sufficient kinetic energy, collisions of free electrons accelerated by an external electric field ionize gas molecules to create reactive precursors, valuable reactants for surface treatment and modification of thin films and nanoparticles. Plasma modification of materials is particularly useful for engineering energetic materials because the contingent surface chemical reactions directly impact the ignition properties and kinetics. Magnesium (Mg) is a desirable fuel for energetics because of its high reactivity and high energy density. However, the boiling point of its native oxide layer is greater than Mg, forcing ignition to proceed via a diffusion-limited mechanism. This dissertation focuses on plasma-induced surface engineering of Mg nanoparticles to improve their reactivity by manipulating the surface chemistry relevant for ignition. Part 1 of this dissertation describes a silicon (Si) coating applied to

Mg to prevent oxide layer formation and passivate the material. In addition to surface passivation, the Si shell reacts with the Mg core upon heating to form an intermetallic alloy and provide supplemental heat release, accelerating ignition kinetics. Partial oxidation of the Si shell results in a nanothermite interface, which further increases the reactivity and supplemental heat release of the Mg nanoparticles. Part 2 will discuss how magnesium hydride (MgH_2) is formed by subjecting Mg nanoparticles to hydrogen plasma treatment. MgH_2 releases hydrogen gas upon heating which generates pressure to push nanoparticles apart and prevent agglomeration and sintering, but the released hydrogen can also serve as a gaseous fuel and release heat. Thus, hydrogenating the surface of Mg alters its ignition mechanism while accelerating the ignition kinetics via supplemental heating. Overall, this dissertation highlights the potential of low-temperature plasmas to engineer reactive nanoparticle surfaces in-flight for energetic applications.

Table of Contents:

Section 1: Introduction and Background (Plasma)

1.1: Plasma Definition……..….1

1.2: Types of Plasma……..1

1.3: Background for Non-Thermal Plasma……...3

1.3.1: Nanoparticles in Non-Thermal Plasmas…….....6

1.3.2: Nucleation and Growth of Nanoparticles……8

1.4: Applications of Non-Thermal Plasma Processing…….....9

Section 2: Introduction and Background (Energetics)

2.1: Energetic Materials……..13

2.2: Applications of Energetic Materials……19

2.3: Core-Shell Nanoparticles……22

2.4: Plasma-Induced Functionalization of Nanoparticles for Energetics……29

2.4.1: Plasma-Induced Coatings of Energetic Materials…….29

2.4.2: Plasma Treatment of Energetic Materials…….32

Section 3: Magnesium/Silicon-Based Core-Shell Nanoparticles[1]

3.1: Introduction……..35

3.2: Experimental Methods……38

3.3: Materials Characterization……..40

3.4: Energetic Performance……49

3.5: Summary…….59

Section 4: Plasma-Induced Hydrogenation of Magnesium[2]

4.1: Introduction…….60

4.2: Experimental Methods……63

4.3: Materials Characterization……..67

4.4: Plasma Characterization……..81

4.5: Energetic Performance……88

4.6: Summary…….94

Final Conclusions:…….……..96

Bibliography:……...99

List of Figures:

Figure 1: Concept of sheath formation and negative charging of the reactor walls within a plasma in order to establish quasineutrality, important to sustain a plasma by repelling electrons to the plasma bulk and balancing ionization as well as losses to the walls of the reactor. ……5

Figure 2: A similar concept of sheath formation on particle surfaces, important for the electrostatic repulsion of particles that prevent particle agglomeration within the plasma……..6

Figure 3: Bar graph showing the volumetric and gravimetric oxidation enthalpies of various metals. ……...14

Figure 4: A photograph of the system that produces Mg nanoparticles with simultaneous Si coatings. Resistive heating utilizing a tungsten boat is used to sublimate Mg precursors as shown in the evaporation source on the right. An orifice allows acceleration of the Mg particles into the plasma reactor where the in-flight functionalization occurs. Reprinted with permission from [1]. Copyright (2023) Wiley-VCH……..39

Figure 5: Schematic of the experimental setup specifying the dimensions and properties of each component. Reprinted with permission from [1]. Copyright (2023) Wiley-VCH…..39

Figure 6: SEM images of Mg particles produced by thermal evaporation followed by gas-condensation using a) 80 A, b) 75 A, and c) 72 A of DC current with their correlated size distributions d–f). Reprinted with permission from [1]. Copyright (2023) Wiley-VCH….42

Figure 7: X-ray diffraction pattern of magnesium nanoparticles synthesized by thermal evaporation-gas condensation method showing hexagonal crystal structure. Reprinted with permission from [1]. Copyright (2023) Wiley-VCH. ……44

Figure 8: Transmission electron microscopy images of (a) uncoated Mg nanoparticles and (b) Si-coated Mg nanoparticles. Lognormal size distributions of (c) uncoated Mg nanoparticles and (b) Si-coated Mg nanoparticles. Reprinted with permission from [1]. Copyright (2023) Wiley-VCH. ……..45

Figure 9: (a) Scanning electron microscopy image of Si-coated Mg nanoparticles. (b) Layered energy dispersive x-ray spectroscopy image of the Mg, O, and Si signals. (c) Mg, (d) O, and (e) Si images of the aforementioned signal. Reprinted with permission from [1]. Copyright (2023) Wiley-VCH. ……..45

Figure 10: HAADF and STEM/EDS images of (a) uncoated Mg nanoparticles displaying a MgO shell and (b) Si-coated Mg nanoparticles displaying a partially oxidized Si coating. Reprinted with permission from [1]. Copyright (2023) Wiley-VCH. ……47

Figure 11: XPS of the Mg/Si–SiO_x particles, Mg control, and Si control showing the a) O 1*s* peaks, b) Si 2*p* peaks, and c) Mg 2*p* peaks. Reprinted with permission from [1]. Copyright (2023) Wiley-VCH. ……..49

Figure 12: a) Tjump-TOFMS full spectrum data for the Mg/Si–SiO_x nanoparticles. b) Timed spectra for Mg/Si–SiO_x nanoparticles, Mg control, and Si control samples showing the evolution of Mg (m/z = 24) release. The c) Mg release profiles, and the d) Bi release profiles for Mg/Si–SiO_x nanoparticles, Si control, and Mg control. Reprinted with permission from [1]. Copyright (2023) Wiley-VCH. ……51

Figure 13: Ignition snapshots from the Tjump visualized from a high-speed camera for (a) Si nanoparticles, (b) uncoated Mg nanoparticles, and (c) Si-coated Mg nanoparticles. All samples were mixed separately with Bi_2O_3 to create nanothermite composite mixtures. Reprinted with permission from [1]. Copyright (2023) Wiley-VCH. ……53

Figure 14: a) DSC profile for Mg/Si–SiO_x particles performed in ultra-high purity Ar. b) XRD of the Mg/Si–SiO_x samples heated to 400 and 1000 °C and analyzed against an unheated sample. The blue circles, black squares, purple triangles, and orange diamonds indicate Si, Mg, MgO, and Mg_2Si, respectively. Reprinted with permission from [1]. Copyright (2023) Wiley-VCH. ……..54

Figure 15: In situ TEM micrographs of a) Mg/Si–SiO_x nanoparticles and b) Mg nanoparticles under a heating rate of 10 °C min^{-1}. c) Schematic showing the ignition pathways for Mg and Mg/Si–SiO_x particles. Reprinted with permission from [1]. Copyright (2023) Wiley-VCH. ……...58

Figure 16: Photograph and schematic of the thermal evaporation and nonthermal hydrogen plasma system. Gas-condensation of thermally evaporated Mg nucleates Mg nanoparticles. A hydrogen plasma is utilized to create atomic hydrogen that continues on to diffuse into the Mg lattice and form crystalline domains of MgH_2. Reprinted with permission from [2]. Copyright (2023) American Chemical Society. ……65

Figure 17: XRD patterns of h-Mg nanoparticles produced using (a) an RF power of 40–100 W and (c) partial pressure of H_2 and their respective H content (b, d). XRD patterns of nanoparticles made with low (80 A) and high (90 A) currents are shown in panel (e). Red circles denote MgH_2 planes, and black squares denote Mg planes in the XRD patterns. Reprinted with permission from [2]. Copyright (2023) American Chemical Society. ……69

Figure 18: TPD of 55 mg h-Mg nanoparticles with a heating rate of 10 ^{o}C min^{-1}. The integrated area underneath the curve yielded the volume of H_2 gas. Reprinted with permission from [2]. Copyright (2023) American Chemical Society. ……72

Figure 19: (a) Production rates of h-Mg nanoparticles with RF power varied from 40 W to 100 W. (b) A photograph of the plasma reactor before synthesis. Photographs of the plasma reactor after synthesis at (c) 80 W and (d) 100 W of RF power. Reprinted with permission from [2]. Copyright (2023) American Chemical Society. ……..73

Figure 20: Particle size distributions of h-Mg nanoparticles synthesized using (a) 80 A and (b) 90 A of current. Reprinted with permission from [2]. Copyright (2023) American Chemical Society. ……..73

Figure 21: (a) Size distribution of 1000 h of Mg NPs from TEM. (b, c) TEM images representative of the size distribution of h-Mg NPs. (d) Size distribution of 1000 Mg NPs from TEM. (e, f) TEM images representative of the size distribution of Mg NPs. Reprinted with permission from [2]. Copyright (2023) American Chemical Society. ……74

Figure 22: HR-TEM of (a) a 300 nm particle, (b) a 100 nm particle, and (c) a 30 nm particle, along with their respective FFT diffraction patterns. Blue arrows indicate the MgO lattice plane; yellow arrows indicate the MgH_2 lattice plane; and red arrows indicate the Mg lattice plane. Reprinted with permission from [2]. Copyright (2023) American Chemical Society. ……77

Figure 23: (a) h-Mg nanoparticles synthesized with decreasing total flow rate of gases while maintaining a constant partial pressure of H_2 (0.237 torr). (b) h-Mg nanoparticles synthesized by decreasing the particle size of the Mg crystallites as well as reducing the total flow rate of gases and keeping a constant partial pressure. The red circles indicate the MgH_2 planes of the tetragonal crystal lattice while the black squares indicate the Mg phases of the hexagonal crystal lattice. ……80

Figure 24: (a) OES spectra of the plasma. (b) Actinometry was used to obtain the atomic H density according to the RF power. The integrated area ratio of the Mg 570 nm and Ar 763 nm lines were obtained from the OES spectra to gain insight into the atomic Mg density at different plasma powers (c). Reprinted with permission from [2]. Copyright (2023) American Chemical Society. ……84

Figure 25: OES measurements showing the emission lines of (a) Mg 570 nm, (b) H 656 nm, and (c) Ar 763 nm. Reprinted with permission from [2]. Copyright (2023) American Chemical Society. ……..85

Figure 26: Graph of nanoparticle temperature based on the particle energy balance approach when assuming an electron temperature of 5 eV and two gas temperatures of 300 and 400 K. The area in blue is the range of H_2 desorption temperatures as obtained by TPD. Reprinted with permission from [2]. Copyright (2023) American Chemical Society..…..88

Figure 27: (a) Mass spectrometry spectra of h-Mg and Mg NPs and (b) Mg release profiles from T-jump/TOFMS for h-Mg/$KClO_4$ and Mg/$KClO_4$. (c) High-speed camera images of ignited Mg/$KClO_4$ and h-Mg/$KClO_4$ thermite mixtures. Reprinted with permission from [2]. Copyright (2023) American Chemical Society. ……...90

Figure 28: Hydrogen, oxygen, and magnesium release profiles from T-jump/TOFMS for h-Mg and Mg NPs during ignition with $KClO_4$. The yellow dashed line indicates the ignition temperature of h-Mg NPs, while the blue dashed line denotes the ignition temperature of Mg NPs. Reprinted with permission from [2]. Copyright (2023) American Chemical Society. ……..92

Figure 29: Pressure-cell tests of 8 wt. %, 25 wt. % MgH_2/Mg composites, and untreated Mg nanoparticles. The results indicate that hydrogen incorporation significantly impacts the (a) peak pressure, (b) pressurization rate, and (c) burn time of Mg. ……..94

List of Equations:

Equation 1: Creation of free electrons from ionization of Ar due to electron collisions.……4

Equation 2: Ratio of electrical power absorbed by ions and electrons. ……..6

Equation 3: Silane reaction with silicon surface. Surface Si = Si(S); bulk silicon = Si(B).....7

Equation 4: Silyl reaction with silicon surface. Surface Si = Si(S); bulk silicon = Si(B).....8

Equation 5: Silylene reaction with silicon surface. Bulk silicon = Si(B)…….8

Equation 6: The heat release from Mg_2Si alloy formation…….55

Equation 7: The heat release according to the magnesiothermic reduction of silica……..55

Equation 8: Calculation for converting the wt. % of MgH_2 within the sample to at. %.....72

Equation 9: Calculation for converting the weight of h-Mg nanoparticles loaded into the furnace for the TPD measurement to weight of MgH_2……72

Equation 10: Calculation for converting the weight of MgH_2 to mmol of H_2 within h-Mg……..72

Equation 11: Calculation of the experimental data for volume of H_2 analyzed by the RGA to mmol of H_2…….72

Equation 12: The relationship between the atomic densities of the gas species to the intensities of the light emission from the atoms, excitation rates, and transition probabilities for optically allowed transitions from excited states of the atoms……..81

Equation 13: Particle energy balance equation using the hydrogen recombination and electron-ion recombination reactions as the heating terms. The cooling term is thermal conduction to the background gas……..87

Equation 14: The additive particle heating term calculations. The hydrogen density (n_H), surface area (S), gas temperature (T_{gas}), Boltzmann constant (k_B), hydrogen mass (m_H), electron temperature (T_{e-}), and argon mass (m_{Ar}) are used in these equations……87

Equation 15: The cooling term calculation that the heating terms are balanced in order to find the particle temperature (T_p) by isolating it…….88

Equation 16: The gravimetric oxidation enthalpy of Mg reaction with $KClO_4$ oxidizer….91
Equation 17: The gravimetric oxidation enthalpy of MgH_2 reaction with $KClO_4$ oxidizer……..91

Section 1: Introduction and Background (Plasma)

1.1: Plasma Definition

The most common states of matter known are solid, liquid, and gas states, in which a solid is the lowest energy state while a gas is in a higher energy state. By applying thermal energy from a solid, melting occurs to reach the liquid state, and the gas state can be attained by further applying energy to evaporate a liquid. Plasmas are considered to be the fourth state of matter because most of the universe exists in the plasma state.[3] In order to reach this state of matter, applying high enough energy to a gas results in the ionization of atoms and the dissociation of molecules, leading to a gaseous mixture of electrons, ions, and neutral atoms or molecules. This electrically conductive gas is considered to be electrically neutral, meaning the negatively charged electrons and ions are balanced by positively charged ions within the plasma bulk.[4, 5] One of the most well-known forms of plasma are flames, which are weakly ionized gas because the fractional number of ions are low. Lightning is another form of plasma that occurs naturally where the degree of ionization is almost 10^{10} m^{-3} larger.[3] Both plasmas are observable due to the photons emitted from excited molecules and atoms when electrons relax to the ground state or lower energy levels.

1.2: Types of Plasma

Two main types of plasmas exist: a thermal plasma (equilibrium plasma) and a non-thermal plasma (non-equilibrium plasma). Thermal plasmas are deemed “hot” and equilibrium plasmas due to the temperature of the electrons and the heavy species

(molecules, atoms, and ions) are in thermal equilibrium and have temperatures on the order of 10^3 K.[6] By contrast, non-thermal plasmas are deemed "cold" and non-equilibrium plasmas because the electrons and heavy species deviate from thermal equilibrium, in which the electron temperature (T_e) is tens of thousands of Kelvins while the temperature of heavy species (T_h) is ~300 K or room temperature.[7]

Thermal and non-thermal plasmas can be produced through man-made methods. The most common and familiar non-thermal plasma is a fluorescent light bulb where a noble gas (i.e. neon) is mixed with mercury vapor and subjected to an applied electric field to break down the gas and sustain a plasma emitting light.[8, 9] A recognizable example of a man-made thermal plasma is a DC plasma torch for cutting or welding. This tool contains a cathode and an anode in which an electric arc is used to breakdown a plasma-forming gas, generating a hot plasma jet.[10]

For the scope of this dissertation, nanoparticle growth and surface modification are important research topics for synthesizing nano-energetics with engineered surface chemistry. Both non-thermal and thermal plasmas can be employed to synthesize nanomaterials. Inductively coupled plasmas (ICP) and capacitively coupled plasmas (CCP) are two techniques to synthesize nanoparticles and functionalize their surfaces. ICPs typically generate plasma using a helical coil with RF current supplied to induce an applied electric field and typically produces thermal plasmas.[11] This configuration contains regions of high ion density and regions of low ion density, in which particles can form in the latter regions although too low of an ion and electron density prevents electrostatic stabilization, resulting in particle agglomeration and large size distributions.[7, 12] In contrast, CCP reactors

consist of two electrodes in which RF current is supplied to create an electric field and are typically used to produce non-thermal plasmas. Particles are confined within the plasma bulk due to sufficient negative charging to prevent particle agglomeration and produce nanoparticles with narrow size distributions.[7]

1.3: Background for Non-Thermal Plasma

In order to form a plasma, breakdown of neutral gas is necessary. There are various ways to input energy into a neutral gas to propagate ionization and form a plasma. One method is to supply thermal energy via exothermic chemical reactions of the molecules, which produces a flame plasma. Photoionization is another method to breakdown a gas involving photons from light with sufficient energy to extract electrons from the gas.[13] The work outlined in this dissertation primarily uses electron impaction with neutral gas molecules and atoms to instigate ionization and form a non-thermal or low-temperature plasma. Electrical energy is supplied to the system to establish an electric field that accelerates "seed" electrons—free electrons produced from background radiation or UV light from the sun, ionizing gas molecules and atoms within the atmosphere—to ionize gas molecules and atoms due to electron collisions. A plasma is sustained once an avalanche of electrons freed from their constituents are available for continual ionization of the neutral gas. **Equation 1** shows the creation of electrons from seed electrons through ionization of argon (Ar) gas, propagating an avalanche of electrons and therefore, gas breakdown.[7, 13]

$$Ar + e^-_{fast} \rightarrow Ar^+ + 2e^-_{slow}$$

Equation 1: Creation of free electrons from ionization of Ar due to electron collisions.

If there was constant ionization of the neutral gas without any other perturbations, the entire gas would breakdown, which changes the plasma characteristics due to the ion and electron densities being extremely high. A natural balance of the ions and electrons occurs through diffusional losses to the reactor walls and electron-ion recombination within the plasma bulk. **Equation 2** shows the relationship between the electrical power and the mobilities of electrons and ions. The electrical power is absorbed by the electrons and ions, however the mobilities of the electrons and ions differ because electrons have much lower mass (10^{-31} kg) than ions ($\geq 10^{-26}$), allowing electrons to be accelerated faster than heavy species within the plasma.[14] Consequentially, electron loss is faster than ions to the walls of the reactor, which charges the walls negative and establishes a sheath near the wall boundary. The sheath has a length, established as the Debye length (λ_D), in which the electric potential changes from the edge of the sheath to the walls of the plasma reactor (**Figure 1**). Electrons are eventually repelled from the sheath near the wall due to the buildup of negative charge causing the electrical potential of the wall to become increasingly negative in comparison to the plasma bulk. These electrons are repelled from the walls and confined within the plasma bulk, which initiates another cycle of ionization—regenerating more electrons and ions. Subsequently, the ions are accelerated to the wall due to the negative potential. Once the Bohm velocity is reached (v_b), the minimum drift velocity of ions near the sheath boundary that is necessary to overcome the electric field

generated by the sheath, ions reach the walls of the reactor at a rate that establishes a sufficiently negative potential to balance the electron and ion currents to the walls. This process is necessary for maintaining quasineutrality within the plasma, in which the electron and ion densities are similar. The sheath is required to repel electrons back into the plasma to continue ionization and electron-ion recombination while attracting ions at a specific rate to maintain equal electron and ion densities ($n_e \approx n_i$) within the plasma bulk. In cases where the electric potential is overly positive, excessive amounts of electrons would be accelerated to the reactor walls and electrons are scarce within the plasma bulk, preventing plasma generation. If the electric potential is extremely negative, the electron density is too large within the bulk, causing excessive ionization and instabilities of the plasma.[5, 7, 14]

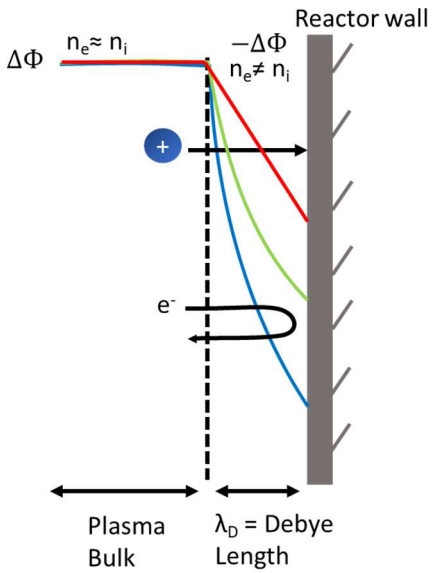


Figure 1: Concept of sheath formation and negative charging of the reactor walls within a plasma in order to establish quasineutrality, important to sustain a plasma by repelling electrons to the plasma bulk and balancing ionization as well as losses to the walls of the reactor. The electron and ion densities are denoted with the blue and green lines, respectively.

$$\frac{P_e}{P_i} = \frac{\mu_e}{\mu_i} = \frac{m_i v_i}{m_e v_e}$$

Equation 2: Ratio of electrical power absorbed by ions and electrons.

1.3.1: Nanoparticles in Non-Thermal Plasmas

Nanoparticles are 3-dimensional objects that contain surfaces. It is important to emphasize that subjecting nanoparticles to a non-thermal plasma inevitably form sheaths at particle surfaces. Similar to reactor wall surfaces, nanoparticles acquire negative charge through electron attachment,[15] resulting in a negative potential and therefore, the same principles of quasineutrality are applied to nanoparticles as well. **Figure 2** depicts the electrostatic repulsion of nanoparticles within a non-thermal plasma due to a formation of a sheath from electron attachment. The electron and ion currents at particle surfaces are balanced once the negative potential becomes sufficiently negative.[7] Overall, nanoparticles experience negative charge buildup that results in their heightened reactivity within a non-thermal plasma because neutral and positively charged species potentially react at their surface.

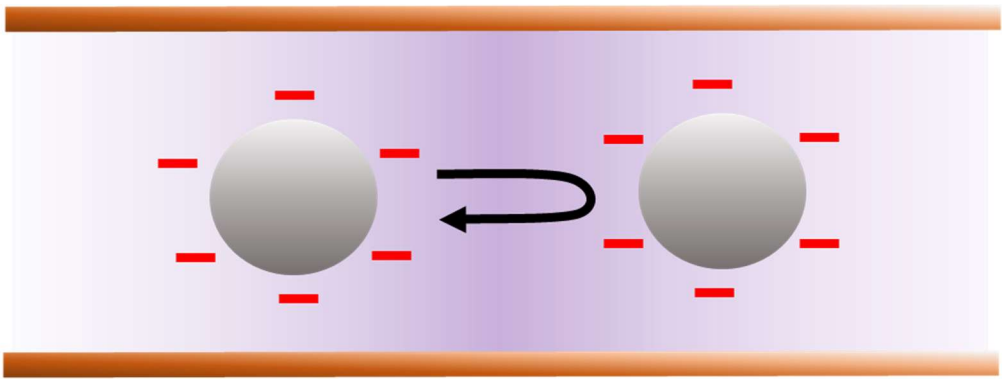


Figure 2: A similar concept of sheath formation on particle surfaces, important for the electrostatic repulsion of particles that prevent particle agglomeration within the plasma.

There are two possible routes for surface growth of nanoparticles in a non-thermal plasma: physical vapor deposition (PVD) and chemical vapor deposition (CVD). PVD is a process involving the vaporization of material in the solid or liquid state and the vapor condenses onto a surface.[16] Such a process is particularly evident in the surface growth of elemental metal nanoparticles in plasmas. Since non-thermal plasmas are usually operated at low pressures (a few torr), the ratio of the molecular mean free path to particle radius, or the Knudsen number, is large and particle growth proceeds in the free molecular regime.[17] Thus, surface growth of particles by PVD is initiated through collisions between the vapor and the nanoparticles, which is enhanced by the induced dipoles created between the negatively charged particles and neutral vapor.[7]

In the case of CVD, dissociated gas precursors are responsible for the surface growth of nanoparticles within a low-temperature plasma. For example, **Equation 3-5** outline the processes for silane (SiH_4), silyl (SiH_3), and silylene (SiH_2) molecules reacting with the surface of bulk silicon.[18] A heterogeneous chemical reaction occurs between these molecules and Si nanoparticles in order to grow Si into larger particles while releasing hydrogen gas (H_2) during the reaction. Anions generated from the plasma would be prevented from contributing to surface growth due to their repulsion from the sheath formation at particle surfaces. Positive ions are likely to contribute to surface growth due to their enhanced attraction to negatively charged particles, although ion densities are typically much smaller than neutral species within a non-thermal plasma.[7, 18]

$$SiH_4\,(g) + 2Si\,(S) \rightarrow 2SiH\,(S) + Si\,(B) + H_2\,(g)$$

Equation 3: Silane reaction with silicon surface. Surface Si = Si(S); bulk silicon = Si(B)

$$SiH_3\ (g) + Si\ (s) \rightarrow SiH\ (S) + Si\ (B) + H_2\ (g)$$

Equation 4: Silyl reaction with silicon surface. Surface Si = Si(S); bulk silicon = Si(B)

$$SiH_2\ (g) \rightarrow Si\ (B) + H_2\ (g)$$

Equation 5: Silylene reaction with silicon surface. Bulk silicon = Si(B)

1.3.2: Nucleation and Growth of Nanoparticles

This dissertation focuses on the surface engineering of nanoparticles; therefore, the process of nucleation and growth of nanoparticles within a non-thermal plasma will be discussed briefly. There are three stages with respect to nucleation and growth of nanoparticles in a low-temperature plasma: cluster and nanoparticle nucleation, coagulation, and surface growth.[7]

1. Nucleation of Clusters and Nanoparticles

For thermal plasmas, nucleation of nanoparticles occurs by a process known as homogeneous nucleation, in which neutral particle clusters are generated through condensation of a supersaturated vapor.[19] Particles nucleate by neutral-neutral clustering in this manner.[20] By contrast, nucleation in nonthermal plasmas is carried out by ion-neutral clustering. Cluster formation is dominated by chemical reactions because ion-neutral reaction kinetics is faster than neutral-neutral cluster formation. Neutral and positively charged species diffuse out of the plasma bulk while anions are confined within the plasma. Consequently, the residing anions within the plasma contribute to nucleation as opposed to positively charged species.[21]

2. Coagulation

For non-equilibrium plasmas, the growth of nanoparticles ensuing nucleation occurs by ion-neutral coagulation rather than neutral-neutral coagulation evident in other gas-phase methods. The attraction of opposite charges may cause some coagulation; however, positively charged ions contribute little to coagulation since they are typically burdened by diffusional losses to the plasma reactor walls, leading to neutral species mainly participating in the coagulation process.[22, 23] An image potential is induced when large, negatively charged particles approach smaller, neutral nuclei and protoparticles, which is significant in their coagulation. Coagulation ceases when small nuclei are scavenged, and the particle density is eclipsed by the electron density, which results in particle repulsion due to nanoparticles charging uniformly negative.[23]

3. Surface Growth

Once the electron density exceeds the particle density due to small particles coagulating with large particles, the nanoparticles become uniformly negative, and coagulation stops due to electrostatic repulsion. Therefore, further particle growth ensues via surface growth. As stated in *Section 1.3.1*, surface growth occurs by PVD or CVD. In PVD, precursors are evaporated to supersaturate the reactor volume and condense onto nanoparticles after colliding. CVD involves the dissociation of gaseous precursors into highly reactive molecules that react with nanoparticles upon collisions by heterogeneous chemical reactions.[7, 18]

1.4 Applications of Non-Thermal Plasma Processing

Non-thermal plasma processing is a versatile technique currently used in a broad range of applications. Low-temperature plasmas have strong potential in biomedical and environmental applications.[24, 25] For example, the low-temperature nature of the process can alleviate the problems associated with other methods in cancer treatment, such as laser treatment that causes excessive heating of biological tissue and can instigate healthy cell and tissue damage.[26] Comparatively, non-thermal plasmas can produce reactive oxygen species (ROS) that cancer cells are more susceptible to as opposed to normal tissue and cells, allowing enhanced selectivity of cancer treatment.[27, 28] Plasma-activated water (PAW) is another application in which reactive species are formed from a low-temperature plasma and is utilized to treat food and increase shelf-life.[29] The reactive oxidative species can damage bacterial cells while having no harmful effects on foods due to antioxidant enzymes in PAW.[30] One of the promising environmental applications non-thermal plasmas are used for is plasma catalysis. Conversion of carbon dioxide, one of the most prominent greenhouse gases, is carried out to create carbon-based chemicals and fuels.[31, 32] Plasma generation of ammonia (NH_4) is a promising application due to the conversion of green hydrogen into NH_4, particularly useful for the agriculture industry.[33-35]

The semiconductor field is another area in which non-thermal plasmas excel in. Carbon quantum dots (QD),[36, 37] Si QDs,[38-41] and germanium (Ge) QDs[42, 43] have all been synthesized by this technique to leverage their photoluminescent properties and tunable bandgaps for solid-state light emission and photovoltaic applications. In nanoelectronics, deposition of semiconductor materials using plasma-enhanced chemical vapor deposition (PE-CVD) and plasma-enhanced atomic layer deposition (PE-ALD) are utilized for

creating highly reactive species pertinent for fabricating surfaces.[44-46] Etching is another approach to manipulating nanodevice services, in which reactive ion etching (RIE) and plasma-enhanced atomic layer etching (PE-ALE) are employed.[44, 47, 48] Currently, PE-ALD and PE-ALE are attractive techniques for thin film fabrication due to their increased selectivity inherent to the processing methods. In both cases, two half-cycles take place in which the first cycle consists of adsorption of reactant species followed by a second cycle related to exposing other reactants and energy to desorb the initial reactant layer (ALE) or to chemically react and form a monolayer of material (ALD).[44]

Nano-energetics is an emerging application for non-thermal plasma processing of nanomaterials. Energetic materials are those that transform chemical energy into thermal energy, pressure energy, and light energy after external stimulation from heat, shock, or an electrical current.[49] Non-thermal plasma processing is a versatile technique for modifying energetic materials. It can be used to increase their reactivity by altering their chemical properties, or to preserve the ignitable fuel by passivating materials to prevent unprompted oxidation that renders fuels inert. Plasmas are a gas-phase method that produces materials without solvents and ligands, resulting in less impurities compared to liquid-phase modification techniques. Electrostatic stabilization of nanoparticles plays an important role in preventing particle agglomeration and aggregation, which leads to narrower size distributions compared to other gas-phase methods.[7] Overall, these qualities of non-thermal plasmas can be leveraged to process and functionalize materials, thereby enhancing their energetic performance. Being that this dissertation is highly related to the plasma

processing of materials to nanostructure and engineer the surface chemistry, more details about this particular field of research are outlined in **Section 2.4**.

Section 2: Introduction and Background (Energetics)

2.1: Energetic Materials

As stated in the previous section, energetic materials release energy in the form of heat, pressure, or light when exposed to an external energy source. Propulsion,[50] ignition,[51] and energy generation[49] are key fields in which energy dense materials are involved. There are two classes of energetic materials: monomolecular and composite energetic materials.[52] A single molecule that contains both fuel and oxidizer groups are classified as a monomolecular energetic material. Commonly known examples are 2,4,6-trinitrotoluene (TNT) and nitrocellulose (NC). Nanothermites and intermetallic compounds fall under the class of composite energetic materials since two components are necessary for combustion (fuel and oxidizer).[49] An example of a nanothermite is aluminum (Al) metal reacting with iron oxide (Fe_2O_3) metal oxidizer.[53]

The work presented in this dissertation focuses on tailoring the performance of energetic materials, mainly Mg. It is important to emphasize that the physical and chemical properties of a material are relevant when tuning its properties for engineered performance. Particle size is significant for diffusion of atoms, in which smaller particles have shorter diffusion lengths for mass transport of atoms, thus reaction kinetics can be hastened by reducing particle size.[54] As particle size decreases, the active content—the percentage of reactive fuel within a particle in comparison to its inert oxide layer—reduces.[55] This is because the native oxide layer on a particle remains constant, but the fuel within the particle core shrinks with decreasing particle size. Therefore, ignition of smaller particles is quicker, but little reactive fuel can lead to less energy release. When modifying materials

to enhance their reactivity and ignition properties, recognizing their chemical properties is important. For example, the melting point, boiling point, and surface properties each affect the combustion mechanisms of a metal fuel. Metals are incredibly energy dense, making them ideal for energetic applications as solid-state metal fuels.[54] **Figure 3** shows the large oxidation enthalpies of different metals. The combustion mechanism of each metal is different due to their unique chemical properties, necessitating careful consideration of approaches for tuning metal energetic performance.

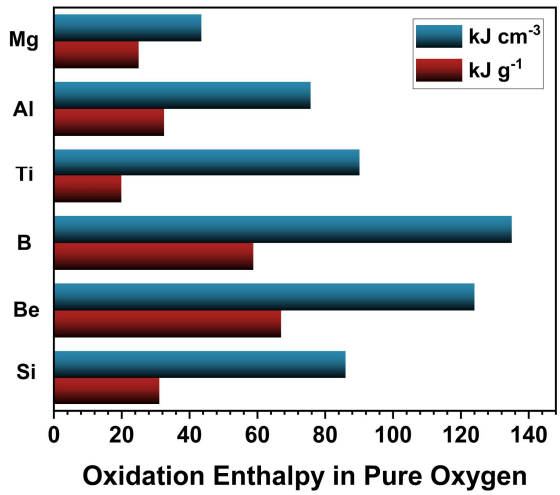


Figure 3: Bar graph showing the volumetric and gravimetric oxidation enthalpies of various metals.

- *Aluminum*

  Al is one of the most widely used metals for energetics because of its high volumetric and gravimetric energy density (~80 kJ cm^{-3} and ~30 kJ g^{-1} when reacting with oxygen), high abundancy, and cost effectiveness.[54] Ignition of Al occurs at 930 K at minimum, which is due to the melting of Al in the core (lower melting point than its

native oxide) and polymorphic phase transformations in the oxide layer causing stresses exerted by its Al core cracking its oxide layer. The transition from amorphous alumina (Al_2O_3) to γ phase occurs at ~820 K. Upon further heating, transition to α-Al_2O_3 occurs above 1170 K.[56] It is important to point out that the density increases after each phase transition, reducing its volume and creating open surfaces or cracks for diffusional pathways for oxygen. Subsequently, oxygen from an oxidizer diffuses to the Al core via the cracks in order for ignition to proceed.[55] Essentially, the energetic performance is heavily reliant on the cracking of its oxide shell to allow oxygen diffusion to the Al surface.

- Boron

Boron (B) is extremely desirable for energetics because its volumetric energy density is the highest among metals (~140 kJ cm^{-3}) and a larger gravimetric energy density (~60 kJ g^{-1}) than Al.[54] However, this metal boils (4200 K) after its oxide (2300 K), boron oxide (B_2O_3), posing a unique problem for its ignition.[57] The minimum ignition temperature for B (~1400 K) is lower than Al, which is due to the following reason.[54] Vaporization of the B_2O_3 layer is necessary to access the pure B fuel and ignite, which is difficult because adiabatic flame temperatures need to exceed the high boiling point of the oxide. First, the oxide layer melts as particles heat, allowing diffusion through the liquid oxide surface. The oxide layer is removed once enough heat is gained to vaporize B_2O_3.[58] Reaction of the exposed B occurs in the second stage of combustion. Once the B_2O_3 is vaporized and the B core is exposed, a phase transformation occurs from α to β phase, which takes place at the onset of ignition.[59]

In summary, the ignition and combustion mechanisms of B involves two stages: melting of the oxide layer to allow diffusion of species followed by vaporization to expose the B core, and a phase transformation of B from the α to β phase in order to oxidize and ignite.

- Beryllium

Beryllium (Be) is an attractive metal fuel for energetics owing to its high volumetric and gravimetric energy densities (~125 kJ cm^{-3} and ~70 kJ g^{-1}) being larger than Al.[54] Though work on Be for energetics is scarce, mainly due to its high toxicity deeming it hazardous and unsafe to experiment on.[60] The boiling point of Be (2740 K) is lower than the melting point of its native oxide (2820 K), beryllium oxide (BeO).[61] This suggests that the ignition mechanism may follow that of Al, involving the vaporization of the Be core followed by melting or cracking of the BeO surface to expose the Be for oxygen transport, or for Be vapor to transport outside of its cracked shell for oxidation. However, the minimum ignition temperature of Be (~1500 K) is much higher than Al, which could be regulated by the melting temperature (~1500 K) and force combustion through similar mechanisms to Al.[61] In Al, the melting temperature is extremely close to its ignition temperature, and stresses from Al melting onto its oxide layer are induced by this phase change. There is no reported phase change of BeO, so the cracking of the oxide layer is due to other reasons, such as compressive stress due to differences in Be and BeO thermal expansion.[62] Despite the higher enthalpy of combustion of Be and its ignition mechanism proposed to be similar to Al, more studies are necessary to investigate the ignition routes and understand the

differences in combustion performance. For example, Al combustion involves phase transitions, but information on whether similar transitions manifest for Be combustion.

- Titanium

  Titanium (Ti) has a larger volumetric energy density (~90 kJ cm^{-3}) than Al, qualifying it as a suitable candidate for energetic applications. Although its gravimetric energy density is lower (20 kJ g^{-1}) because its atomic weight is almost double that of Al.[54] The boiling point of Ti (~3600 K) and its oxide (3200K) are considerably high, driving combustion to take place by surface reactions.[57] Ti ignition is associated with an α to β phase transition occurring at ~900 ºC is necessary before oxidation. In addition, Ti melts at around 1900 K after it ignites, allowing combustion reactions to proceed by gas dissolution of oxygen into liquid Ti metal.[63] Overall, the gas-phase diffusion of oxygen into Ti during different stages of combustion is the limiting factor for ignition.

- Silicon

  Si is another metal that has volumetric (~30 kJ cm^{-3}) and gravimetric (~75 kJ g^{-1}) energy densities nearly identical to Al, making it ideal for combustion applications.[54] The melting (~1700 K) and boiling (~3100 K) temperature of Si is noticeably higher than Al. Moreover, the melting point (~2000 K) and boiling point (~2800 K) of silicon oxide (SiO_2) are incredibly high, highlighting the significance of surface reactions in ignition.[57, 64, 65] Regardless, the ignition threshold for Si is at the low-end of the ignition temperature spectrum for metals, igniting around ~1000 K at minimum.[54, 66] The process of pure Si ignition is as follows, diffusion of oxygen through the SiO_2 layer

accompanied by stress-induced fracturing of the crystalline Si.[67] The specific molar volume of SiO_2 is much larger than Si, causing compressive stress onto the Si.[68] Upon further heating, molten Si is formed, in which oxidation can proceed by gas-dissolution.[67, 69] Ultimately, ignition of Si is a diffusion-limited process involving oxygen reaching the Si core followed by cracking of the Si layer due to expansion of the growing SiO_2 layer.

Another mechanism is explored for Si ignition, involving terminated hydrides residing at the Si surface brought upon by relevant synthesis methods (usually related to silane as a precursor).[66] The release of hydrogen under heating causes silicon dangling bonds, immobilized free radicals with high reactivity, which provide accelerated pathways for oxidation.[66, 70] Thereafter, slower oxidation of the Si occurs in a similar fashion to pure Si, in which a diffusion-limited reaction takes place due to a growing SiO_2 layer. To summarize Si ignition, the Si surface is critical to instigate oxidation. Without the presence of silicon hydrides, a diffusion-led mechanism happens for oxidation of the Si core followed by cracking of this layer. With the presence of hydrides on the surface, desorption of hydrogen is vital to create Si dangling bonds and provide a fast pathway for oxidation.

- Magnesium

Among the metals discussed above, Mg has the lowest volumetric energy density (~50 kJ cm^{-3}); however, the gravimetric energy density (~28 kJ g^{-1}) makes it competitive for energetic applications.[54] The boiling point (~1300 K) is significantly lower than that of Al (~2600 K), differentiating mechanism of Mg ignition from Al.[57]

Vaporization of the Mg core is an essential process for its oxidation. The extremely high melting point (~3100 K) of its native oxide layer, magnesium oxide (MgO), governs the ignition of Mg via a diffusional mechanism.[71] Mg is one of few metals that vaporize within its core and permeates through its oxide layer in order to react with an oxidizer. Because Mg is highly volatile and the MgO layer is porous, Mg vapor is produced at low temperatures and transports easily through its oxide, resulting in one of the lowest ignition temperatures (~800 K) among rival metals.[71] For this reason, Mg remains one of the most attractive metals for energetics.

2.2: Applications of Energetic Materials

A few obvious applications of materials that release thermal energy are explosives for the military, civil engineering, and mining. Monomolecular compounds (i.e. TNT, HMX, RDX) are typically used for these applications due to their high energy density. TNT, HMX, and RDX are all typically used for munitions, rockets, and high explosives involved for warfare and defense. Demolition of buildings is important for clearing large buildings in civilian-populated areas, in which the soft and formable properties of RDX—a plastic explosive—is used for. TNT explosives have been widely used for mining operations to clear tunnels because of their insensitivity to shock and friction, which typically ignites other explosives prematurely.

Rocket propellants for military and space purposes is another application that energetic materials are used for. Monomolecular compounds can produce pressurized gas, which is useful for propellants. Gas-generating materials are particularly desirable for

propellants because producing gas will generate pressure, but releasing a flammable gas provides added fuel for combustion. Modern rocket propellant fuel contains Al powder fuel, ammonium perchlorate (AP) as the oxidizer, and hydroxyl-terminated polybutadiene (HTPB) organic binder that preserves structural stability in the composite solid fuel mixture. Solid-phase energetic particles are used as additives in liquid fuels for propellants because they improve the specific impulse, a measure of the thrust force per unit of the fuel. Thrusters in microsatellites and micro-propulsion systems use the specific impulse from solid particles.

Explosive welding to join metals and combustion synthesis of materials are other applications in which energetic materials are helpful. Different metals and alloys can be joined together through explosive reactions that propagate deformation processes in the participating metals. Diffusional mechanisms are bypassed due to the fast reaction kinetics taking place in μs, which promote solid-phase bonds between the metals or alloys. Intermetallic energetics and nanothermites excel for this purpose because they can be used for localized heating, in which external heating sources are ineffective, and because they achieve high adiabatic flame temperatures as well as accelerated burn rates. Moreover, little gaseous reaction products are produced, enabling materials to weld together. Combustion synthesis is a versatile method of nanomaterial preparation of inorganic materials. Refractory materials, such as ceramics and alloys, can be produced by self-propagating high-temperature synthesis due to the large exothermic reactions. The possibility of synthesizing a broad range of materials enables its use for producing material in a wide

range of applications (i.e. optical engineering, biomedical, energy, construction, defense, etc.).

Hydrogen production[72] and chemical oxygen generation[73] are a couple of areas in which metal energetic materials can be implemented to generate energy. H_2 can release from combustion reactions involving metal fuels without a catalyst compared methods involving aqueous alkaline solutions. The released H_2 can then be utilized for fuel cells to generate electricity.[72] Oxygen generators are important for anaerobic environments in which oxygen is needed to sustain human activities, such as spacecraft, submarines, and deep mines. Metal fuels can react with oxygen releasing compounds at low ignition temperatures.[73] Coupling the two chemical processes can create electrical power while providing respirable air for space and subsurface applications.[72]

Energetic materials are also used for biocidal agent defeat to combat biochemical warfare.[74, 75] Iodine-based substances have shown to have bactericidal, fungicidal, and virucidal effects, therefore are used for disinfection.[76-78] Metal energetics can be employed for combusting with iodine-based oxidizers to release atomic iodine.[79] Additionally, silver (Ag) has biocidal effects, which Ag-based oxidizers can be utilized to release gaseous Ag.[80-82] Dispersal of the biocidal is important in neutralizing an airborne biochemical weapon, thus gas-generating energetic materials are desirable for agent defeat applications.[83, 84] Diisopropyl methylphosphonate (DIMP) is an alternate organophosphorus compound used to emulate other chemical warfare agents (CWA).[85, 86] Recent work is carried out to decompose DIMP at low temperatures and at faster rates. Metal oxides have been shown to catalyze the decomposition of DIMP below its boiling

point.[87] Based on these studies, combustion of energetic materials that produce metal oxides is pertinent for CWA defeat.

2.3: Core-Shell Nanoparticles

Core-shell nanoparticles are a burgeoning class of materials that are broadly used in diverse applications. Their nanostructured effects are recognized for improving material properties due to the unique combinatorial behavior that is distinct from the individual components.[88] In relation to nanoenergetic materials, surface interactions are significant for ignition, therefore the direct contact between reactive species within a core-shell structure is crucial for improving ignition and combustion behavior.[54] As mentioned in **Section 2.1**, the native oxide layer that inherently forms on metal particles regulates the diffusional processes involved in ignition.[55, 58, 71] Hence, much work focuses on manipulating the surface of nanoenergetic materials in order to alter their ignition pathways. Alternatively, sensitive explosives prone to accidental detonation—typically materials in which shock or impact initiate ignition—are subjected to surface passivation to resolve spontaneous ignition instigated by unintentional sources of shock and impact.[89, 90]

Passivating a nanoparticle surface by surface modification is a common approach to preserve solid nanofuels and reduce their surface reactivity in atmospheric conditions.[91] One method for passivation is to use reactive mediums to interact with particle surfaces in a controlled manner. For example, using an inert gas that contains low amounts of oxygen can result in thinner oxide layers around Al, which can increase the active content of the

material by preventing thick oxide layers from forming. The particles can be stored for 3 days to ensure slow oxidation and stirred to allow shells to form uniformly.[92] Liquid mediums can also be used for surface passivation of nanoparticles. Hydroxyl-terminated polybutadiene (HTPB) coatings on Al nanoparticles can be produced by a laser-induction complex heating technique.[93] Molten Al is produced by high-frequency induction, and a high-power laser evaporates the molten Al. Particles are formed via gas-condensation using Ar inert gas. Subsequently, the Al particles penetrate into a cover containing smeared HTPB, which results in HTPB-coated Al particles. A HTPB coating around Al (without the presence of an oxide layer) passivates the Al core fuel for 2 years minimum while maintaining heightened reactivity in comparison to uncoated Al (contains an oxide shell).

The use of polymer coatings onto energetic materials is useful in reducing sensitivity. HMX is typically sensitive to impact and electrostatic spark. Researchers have investigated conductive oxide coatings to combat electrostatic spark sensitivity, but their rigidity often exacerbates impact sensitivity.[94] Therefore, conductive polymer coatings can solve sensitivity issues due to their flexibility and ability to dissipate charge. In situ polymerization is a wet chemistry approach to attaching polymers to the surface of monomolecular energetic compounds.[95, 96] HMX can be mixed in deionized water with a polymer to induce coating with the surface. Metal nanoparticles are also functionalized with polymers because of their vulnerability to reacting with atmospheric components.[97] Wet chemistry methods are typically used to encapsulate and passivate metal nanoparticles. In situ polymerization,[98, 99] solvent/non-solvent method,[100-102] and emulsion

polymerization[103, 104] are some examples of methods typically used to passivate and reduce the sensitivity of metal nanoparticles.

Coating metal nanoparticles with another metal creates a bimetallic particle in which the core is passivated while the metal-metal interface can react through intermetallic exothermic reactions.[105-108] Not all metals are miscible with one another because a thermodynamic driving force is lacking, therefore not every metal combination can form an alloy.[109] Two immiscible metals can indeed be forced to form an alloy by overcoming an activation energy barrier (usually thermal energy) followed by quenching the metastable mixtures.[110] In terms of energetic materials, a core-shell nanostructure of immiscible metals is counterproductive because energy is absorbed (endothermic reaction) to form an alloy, reducing the energy release from combustion. Therefore, it is crucial to exploit the alloying reactions that take place from miscible metals.

Previous work focused primarily on metallic coatings onto Al nanofuels. Passivation using palladium (Pd), silver (Ag), gold (Au), and nickel (Ni) coatings onto Al have been achieved through a solution method.[111] It was found that Ni was the only metal coating that resulted in sluggish oxidation of the Al core after exposure to ambient and humid conditions. Other studies were conducted involving Pd coatings onto Al; however, the aim was to investigate the effects of an exothermic alloying reaction between the core and shell on ignition.[112-114] Shorter ignition delay times and a lower ignition temperature than uncoated Al. Thus, Pd may not serve as a passivating layer, but as a reactive shell able to accelerate Al ignition through exothermic alloying reactions. Exploding wire synthesis of Si-coated Al nanoparticles was studied, although it was mentioned that slow exposure

to air allowed the oxidation of Al to form an Al_2O_3 shell as well as some agglomeration of Si onto the surface.[115] The study found that the ignition temperature of Al nanoparticles decreased with addition of Si to the shell, which may be attributed to faster oxidation of the core fuel since the Si portions of the shell is less dense than Al_2O_3, creating pathways for oxygen diffusion. Additionally, the Al functionalized with Si increased the energy release from nano-Al. Another work explored the addition of a double shell of Ni and phosphorous (P) applied to Al by electroless plating method.[116] The authors found that the pressurization rate increased by 11-fold and the ignition delay time shortened in comparison to raw-Al, which is attributed to an intermetallic exothermic reaction taking place to enhance mass and heat transfer to the Al core.

Despite most of the work on metal coatings concentrating on Al, coatings onto B metal nanoparticles resulting in bimetallic nanostructures have been developed as well. Aspirations of harnessing the large energy density of B has sparked interest in utilizing metal coatings onto its surface since the melting of the surface oxide is detrimental for ignition. One instance is iron (Fe) coatings onto B particles using a thermal decomposition of Fe precursors followed by solution mixing with B.[117] The Fe coating accelerated the burn rate of B because it served as a transporter of oxygen. Particularly, the outer Fe layer is oxidized by ambient oxygen to form an oxide, which subsequently transports the oxygen by undergoing a redox reaction with the B core. The oxide layer on B can be replaced with Ni,[118] Ti,[119] and Mg[120-122] to have similar effects on ignition of B fuels. Overall, replacing the oxide layer around B particles is critical to enhance the ignition characteristics because it circumvents the second-stage ignition process that regulates B combustion. Besides Al

and B, there is little work on other metal fuels associated with bimetallic nanostructures in which intermetallic reactions are exploited to accelerate ignition, highlighting an opportunity for future work in this research area.

Engineering the surface of metal nanoparticles with an oxidizer is another method of enhancing ignition. A tremendous amount of work focuses on this approach due to the large energy release generated by the nanothermite reactions.[123] Composites in this fashion may exhibit ignition behavior similar to monomolecular compounds due to the chemical bonding of the oxidizer to the interface of the fuel. Among the many types of oxidizers available to react with metal fuels, chlorates,[124-129] fluorocarbons,[130-133] and metal oxides[134-138] are typically chosen as a coating material. Chlorates as oxidizers exhibit large amounts of energy release when reacting with a metal, which can exceed the energy release from metal oxide oxidizers. A few studies involving potassium perchlorate ($KClO_4$) coatings have been pursued in the past, in which the intimate contact between the fuel and oxidizer allows faster oxygen transport that results in faster burning rates.[124, 125] A larger number of studies focuses on ammonium perchlorate (AP) coatings due to it being a common oxidizer component for propellants.[139] Its high heat release, stability, and gas-generating ability makes it a great candidate for propellant applications.[140] Coating metal surfaces with AP facilitates the high temperature decomposition of AP because of the thermal and chemical interactions that occur between the metals and metal oxides and the intermediate decomposition products of AP. Most of the research focuses on utilizing the catalyzing behavior of various combinations of metal and metal oxides in order to hasten

the decomposition of AP and enhance the combustion properties as well as the burn rates.[127, 128, 141-147]

Utilizing the high electronegativity of fluorine is useful for energetics because it creates a strong oxidation environment in comparison to oxygen.[148] Thus, synthesizing core-shell composites in which the shell is composed of fluorinated materials is highly desirable. A large number of research involves fluorocarbon coatings onto various metal fuels. For Al-based composites, fluorination generates a large gravimetric energy release (higher than oxidation) and produces gaseous aluminum fluoride (AlF_3), which is beneficial for rocket propellants.[149] Coating the surface of Al that originally contains an Al_2O_3 shell is not necessarily detrimental to ignition because the fluorocarbon can react with Al_2O_3 and avoid the normal ignition mechanism associated with cracking the Al_2O_3 layer to allow Al oxidation. Many studies using various fluorocarbon compounds showed that corrosion of the Al_2O_3 layer on Al is the reoccurring mechanism involved in reducing the Al ignition threshold while increasing the energy release and burn rate.[132, 150-154] Effects of B combustion with a fluorocarbon or a fluorine-based coating is similar to that of Al with fluorocarbon in which the fluorine reacts with the oxide layer to expose the B core for oxidation.[155-157] Gaseous products, such as boron fluoride (BF_3) or boron oxyfluoride (BOF) are produced. Fluorocarbon coatings onto Si particles have been studied as well.[158, 159] The prospects of generating silicon fluoride (SiF_4) gas by fluorination of Si fuel is promising for propellants. Additionally, fluorine can react with the oxide layer of Si and produce more energy.[158] Fluorination of Mg is unique compared to other metals because MgF_2 products are in the solid phase.[160, 161] The MgF_2 layer that forms eventually becomes

a diffusional barrier for oxidation or further fluorination.[162] The size of Mg particles directly impacts its ignition, in which μMg ignition proceeds by Mg evaporation followed by decomposition of the fluorocarbon while nMg ignition proceeds by condensed phase fluorination with subsequent evaporation of Mg and oxidation. Oxidation reactions are more dominant than fluorination for nano-sized Mg.[160]

Surface modifying metal fuels with metal oxides is another way of improving the ignition properties and reaction kinetics. Ensuring close contact between the fuel and oxidizer allows for faster atomic diffusion by decreasing the mass transfer lengths, which results in faster kinetics.[163] A plethora of metal oxide coatings onto Al have been explored in the past including, but not limited to, iron oxide (Fe_2O_3),[164-166] tin oxide (SnO_2),[167] nickel oxide (NiO),[168, 169] manganese oxide (Mn_3O_4),[170] zinc oxide (ZnO),[171] silicon oxide (SiO_2),[172] and copper oxide (CuO).[136, 173] In each of these reactive interfacial systems, the diffusivity of oxygen is heightened due to the shortened diffusion lengths for the thermite reactions, which results in increased energy output while quickening reaction timescales. Boron,[174-177] magnesium,[1, 178] silicon,[179] and zirconium[180] have all been coated with metal oxides in order to increase their reactivity and energy release during ignition. A similar effect occurs by modifying the surface with a metal oxide, the intimate contact between fuel and oxidizer allows for faster ignition sparked by solid-state reaction as opposed to a heterogeneous phase reaction. Overall, attaching metal oxides to the surface of metal fuels accelerates ignition, reduces the ignition threshold, and increases energy release for combustion of metallic fuels.

2.4: Plasma-Induced Functionalization of Nanoparticles for Energetics

Plasma functionalization of materials is a promising processing method to surface engineer nanomaterials for specific chemical properties. Plasma processing encompasses an extensive range of applications, in which plasma processing is an innovative method to engineer novel energetic materials. In particular, non-thermal plasmas are useful for material processing of energetic materials due to the inherent low-temperature quality of the synthesization or functionalization process. For instance, thermally-sensitive polymers that are prone to degrading at low temperatures or possess a low melting point can be processed by this method.[181] Non-thermal plasmas have the ability to create highly reactive radicals from the precursor gas that can react and modify material surfaces, making it a proficient processing method to design the surface chemistry through functionalization or surface coatings.[182-184]

2.4.1: Plasma-Induced Coatings of Energetic Materials

nanoparticles sensitive to reacting in ambient conditions or the surrounding environment can be passivated to prohibit undesired surface reactions and preserve the particle core. For the case of energetic applications, the native oxide layer that inherently forms on the surface after exposure to ambient conditions limits ignition of the metal core by regulating the diffusion of atoms necessary for combustion. Low-temperatures plasmas enable the passivation of nanomaterials through surface coatings that protect the particle core from oxidizing. Abundant studies have shown the passivation ability of non-thermal plasmas.[1, 42, 185-189] Therefore, this processing method may be beneficial for preserving metal nanoparticle cores from solid-fuels. Moreover, attaching materials with the potential

to react with the metal fuel can enhance ignition due to the direct contact and better surface coverage to particle surfaces as discussed in **Section 2.3**.

A few studies have been carried out investigating the potential use of non-thermal plasmas as a coating technique for energetic materials. One study coated Al nanoparticles via non-thermal plasma with toluene, isopropyl alcohol, and perfluorodecalin in order to passivate the surface and prevent Al_2O_3 formation.[190] Attaching the different molecules to the surface of Al changed the hydrophobicity, of which the isopropyl alcohol was most hydrophilic and the perfluorodecalin was the most hydrophobic. It was found that the energy release was higher from the coated Al nanoparticles compared to uncoated Al, which the most hydrophobic coatings prevent moisture from the humid environment from interacting with the Al core. Another study utilized plasma-enhanced CVD to coat B nanoparticles with perfluorodecalin to preserve the B metal and prevent oxidation.[191] The authors note that the energy release was maintained for 60 days, confirming successful coating and passivation of the B metal. The energy release was originally increased by ~20 % because the plasma reduced the native oxide layer, which increased the active content of the B particles.

Surface coatings onto nanoparticles that enhance the reactivity at the surface of metal fuels can also be accomplished by non-thermal plasmas. Fluorocarbon coatings onto Al can improve its ignition because fluorination of Al is highly exothermic. One study applies a perfluorodecalin coating onto Al particles via a plasma-enhanced CVD method.[192] Al particles with an Al_2O_3 shell was functionalized, in which the fluorine from the fluorocarbon reacts with and eliminates the oxide shell to produce AlF_3. The

nanoexplosions provide a pathway for oxidation of the Al core, enhancing ignition. Additionally, the heat release was tested after aging of the coated and uncoated nanoparticles, of which the fluorocarbon-coated Al maintained its heat release whereas the heat release from uncoated Al is drastically reduced. In another study, a fluorocarbon coating onto aluminum boride (AlB_2) nanoparticles were produced by plasma-enhanced CVD.[193] It was found that the heat release from coated AlB_2 was almost double that of a mixture of Al and B. The proposed mechanism is as follows, Al reacts with the B_2O_3 to produce more B metal fuel while the exothermic fluorination of B at the interface helps create contact between the oxidizer and B fuel. An in-flight plasma-induced coating process was developed in order to synthesize Si-coated Mg nanoparticles to create a core-shell nanostructure.[1] A flow-through reactor was engineered to produce Mg nanoparticles by gas-condensation followed by plasma coating with Si in one-step fashion. The resulting particles were subsequently exposed slowly to air to partially oxidize the Si shell, forming a thermite interface. The interaction between the Si and Mg at the interface caused an intermetallic alloying reaction that accelerated the ignition kinetics of Mg, which was followed by magnesiothermic reduction of the silica outer layer for further supplemental heating of the Mg nanoparticle. Thus, the ignition threshold was reduced, and the reaction kinetics were accelerated from the increased surface reactivity of the Mg nanoparticles. More details about the Si-coated Mg nanoparticles for ignition will be discussed in **Section 3** because this contribution is a part of the dissertation.

2.4.2: Plasma Treatment of Energetic Materials

Low-temperature plasmas are proficient in treating nanomaterial surfaces. Some examples of utilizing this method to enhance material properties include doping material surfaces with atoms,[194-196] introducing vacancies or defects within the material,[197-199] and treating surfaces with hydrogen or oxygen.[200-203] The wide range of applications involving surface treatment by non-thermal plasma processing outline the versatility of this technique in engineering nanomaterials for enhanced performance. Plasma surface treatment of energetic materials is a promising approach to tailor the reactivity of nanomaterials and enhance ignition. Introducing oxygen vacancies within the metal nanoparticle fuel can establish an accelerated oxidation pathway, reducing ignition thresholds.[204] Hydrogenated compounds are useful in energetics due to the gas-generation and reactivity of H_2 as a secondary fuel.[205] Therefore, there is untapped potential for the use of plasma treatments of energetic materials to develop application-specific material surfaces and improve solid-fuel ignition.

A few reports exist regarding the plasma surface treatment of Al nanoparticles to enhance ignition. A few studies utilized a helium (He), argon (Ar), and He/carbon monoxide plasma separately to etch the native oxide layer that serves as a diffusional barrier for ignition.[206-208] A 40 % reduction of the oxide layer was found for both the Ar and He plasma treated Al, and the authors saw a faster oxidation rate in comparison to untreated Al. Thinning of the oxide shell provides shorter diffusion lengths for atoms to transport and exothermically react. In another study, plasma-induced hydration of Al nanoparticle surfaces was achieved.[209] A He/water vapor dielectric barrier discharge

plasma was used to thin the oxide shell on Al and simultaneously treated with hydroxyl species upon plasma-hydration. The engineered surface increased the pressurization rate by an incredible 50 %, which was attributed to the decreased diffusional barrier from a thinner oxide shell as well as close contact of the oxidizing species at the interface. Moreover, hydrogen gas was produced during combustion to increase the pressurization rate of Al.

Energetic materials containing hydrogen are highly beneficial for ignition purposes because the desorbed hydrogen upon heating can exothermically react with oxygen.[210] In addition, hydrogen gas generation benefits ignition because it increases the pressure generation.[211] A couple studies have focused on the hydrogenation of metal nanoparticles by hydrogen plasma treatment. The surface of Al was treated with hydrogen, in which aluminum hydride (AlH_3) was incorporated within the oxide shell.[212] The authors stated that the desorption of hydrogen from the surface exposes the Al surface to the oxidizer to improve contact. Hydrogen plasma treatment also reduces the oxide shell that serves as a diffusional barrier to ignitioin. It was found that the heat release was improved by 33% compared to untreated Al. Combustion products of untreated Al showed an oxide shell, signifying incomplete combustion and evidence of the Al_2O_3 shell acting as a barrier to oxidation. In contrast, the combustion products from plasma-treated Al showed complete oxidation. Plasma-induced hydrogenation of Mg nanoparticles can also be achieved for energetic purposes.[2] An Ar-H_2 plasma was employed to produce magnesium hydride (MgH_2) by diffusion of plasma-produced atomic hydrogen into Mg cores in-flight with subsequent nucleation of MgH_2 crystalline domains. Processing parameters were

controlled in order to maximize MgH_2 production, in which hydrogenation was mostly affected by Mg particle size. It was found that the incorporation of hydrogen to the surface of Mg benefited ignition by accelerating ignition kinetics depending on the chose oxidizer. By choosing an oxidizer that release oxygen at a similar temperature to the hydrogen desorption temperature of MgH_2, the ignition temperature can be reduced dramatically by over 200 K compared to untreated Mg. Therefore, surface reactions evolves when hydrogen is present on the Mg particle surface. Ignition of hydrogen treated Mg occurs upon desorption of H_2 from the particles, whereas ignition of untreated Mg occurs when oxygen releases from the oxidizer. Moreover, Mg releases from the plasma-treated Mg earlier, which accelerates its oxidation with the oxidizer. In summary, the few studies concerning plasma-induced surface treatment of metal nanofuels highlight the great potential of non-thermal plasma as a processing method to enhance ignition and overall energy release.

Section 3: Magnesium/Silicon-Based Core-Shell Nanoparticles

3.1: Introduction

Even though ignition of metal particles can be improved by reducing particle size to shorten diffusion lengths of atoms, there are inherent disadvantages. It results in a significant decrease in active content as size is pushed into the sub-micron regime.[213] In addition, sintering and agglomeration of particles during ignition often leads to inefficient combustion, in which the oxide layer that thickens during oxidation eventually hinders the metal core from completely combusting.[54, 214] The native oxide layer that forms on the surface of all metals serves as a diffusional barrier for oxidation, hampering the reaction kinetics.[54, 215] Among metals, Mg has attracted interest for energetic applications because of its abundance, volatility, and high volumetric energy density.[216-218] Combustion of Mg is regulated by a diffusion-limited mechanism, in which Mg vapor diffuses outside of its oxide shell to react with oxygen since the boiling point of Mg is much lower than its oxide (1090 ^{o}C << 3600 ^{o}C).[71, 219] Despite the porous nature of the oxide layer facilitates the Mg vapor transport, this process remains the rate-limiting step for the ignition of nanoscale Mg particles.[220]

Surface modification has been actively investigated as a means toward passivating metal surfaces and enhancing interfacial interactions for combustion-related purposes.[206, 221-223] The combustion of aluminum (Al) particles can be improved with the addition of an inorganic coating applied by a heterogeneous nucleation method. Faster decomposition of the oxidizer was caused by better surface coverage of the Al with AP due to the surface coating.[224] Silylation chemistry can be utilized to apply fluorocarbons to Al nanoparticles

(nanoparticles) to improve their reactivity and combustion performance.[225] Wet-chemistry methods can be used to simultaneously nucleate Al nanoparticles coated with a fluorocarbon coating, to make an oxide free system.[222] The disadvantage of the coating methods in the aforementioned work is the use of toxic solvents and the required washing and drying steps. Al nanoparticles can be coated with various transition metals to prevent them from oxidizing in air. The active content of Al is higher with a nickel coating compared to the uncoated sample.[111] Core-shell particles composed of an Al core and iron shell by electroless deposition, which exhibited a higher energy release rate than uncoated Al.[226] The approach involved pre-treatment of the powder to remove the alumina layer before applying the metal coating, which introduces a critical step in the synthesis scheme. There is considerably less work on the coating of Mg powders for combustion applications. One report shows that Mg fuel can be preserved by a paraffin coating using a supercritical solution method.[227] The purpose of the coating is to passivate the Mg surface and stabilize it in air. In another report, a successful coating with siloxane by reactions with cyclic hydridomethylsiloxanes with Mg powder was achieved.[228] The coating improves stability compared to uncoated Mg while minimally decreasing the ignition temperature of Mg.

Motivated by these reports as well as by the scarcity of work involving coatings of energetic Mg nanofuels, we explore the plasma surface modification of Mg nanoparticles with the goal of improving their combustion kinetics. The goal of this work is to utilize a non-thermal plasma to create highly conformal coatings onto Mg and increase its surface reactivity. Coatings are achieved onto airborne Mg nanoparticles formed from gas-condensation method under anaerobic conditions to prevent a native oxide layer from

forming. Non-thermal plasma processing is a versatile gas-phase synthesis method for nanoparticle production,[229-231] thin-film deposition,[232, 233] surface modification,[234, 235] and coatings.[236, 237] Non-thermal plasmas offer several advantages over other gas-phase processing methods. The aerosol in a low-temperature plasma becomes negatively charged, preventing agglomeration, and leading to narrower size distributions.[238-240] Free electrons, or seed electrons, are accelerated by an applied electric field, having temperatures in the range of a few eVs generates highly reactive free-radicals and drive reactions at low gas temperatures. As a result, materials with controllable degree of crystallinity (crystalline or amorphous) can be produced.[7, 66] Solvents and ligands are unnecessary, which helps produce highly pure products. Previous reports involving coatings onto airborne nanomaterials are achievable through non-thermal plasma processing. For instance, recent work has shown that silicon nanoparticles can be either surface modified with polymer,[241] or coated with carbon.[242] Core–shell semiconducting quantum dots[42] and plasmonic materials[243, 244] have also been generated through inflight plasma coating.

In this work, we use a non-thermal plasma to coat Mg nanoparticles in-flight with a silicon shell before an oxide layer forms, and we investigate its effects on ignition. Thermal evaporation with subsequent gas-condensation is used to produce an aerosol of Mg nanoparticles starting from a solid Mg precursor. Resistive heating of the Mg precursor generates a Mg vapor cloud while argon gas is used to quench the vapor to drive the homogeneous nucleation of nanoparticles as well as a carrier gas to feed the Mg-laden aerosol into the plasma reactor.[245] The Mg-laden aerosol is subsequently passed to a non-thermal plasma chamber where the silicon coating is applied in-flight in a simultaneous

manner. The addition of a silicon coating serves a dual purpose: it limits the growth of the MgO shell while also achieving direct contact between the fuel (Mg) and a supplementary oxidizer, since the silicon shell is inevitably partially oxidized. Effectively, this approach leads to a nanothermite interface, a reactive surface connecting the metal reducing agent and oxidizer. The application of the silicon-based shell directly onto the surface of the Mg nanoparticles leads to short diffusion distances, resulting in a significant reduction in ignition temperature and rapid combustion kinetics for boosted performance when the coated material is ignited with a primary oxidizer such as bismuth oxide (Bi_2O_3).

3.2: Experimental Methods

The experimental setup is shown in **Figure 4** with more details of the setup outlined in **Figure 5**, depicting specific configuration parameters of the system. Mg nanoparticles were prepared by thermal evaporation, where bulk Mg precursor (~250 mg) was heated while flowing argon gas at a flow rate of 350 sccm, and the chamber pressure was 40 torr. The Mg-laden aerosol generated from the evaporator stage was injected through an orifice into the non-thermal plasma reactor along with 60 sccm of an argon–silane mixture (1.36% SiH_4 in Ar) for in-flight coating. H_2 (30 sccm) was also added to the plasma to minimize the nucleation of Si particles and ensure that the silane precursor was used to coat the Mg nanoparticles. The plasma reactor consists of a 2″ quartz tube and copper parallel plate electrodes, to which a radiofrequency (RF) signal was applied to sustain the discharge. The plasma reactor was maintained at a pressure of 1 Torr, and the RF power was 60 W at 13.56 MHz. The estimated residence time in the plasma reactor, based on flow velocity,

was ~185 ms. The coated particles were collected onto a stainless-steel mesh filter downstream of the plasma reactor. The nanoparticles were extracted from the vacuum system after slowly leaking air to prevent ignition.

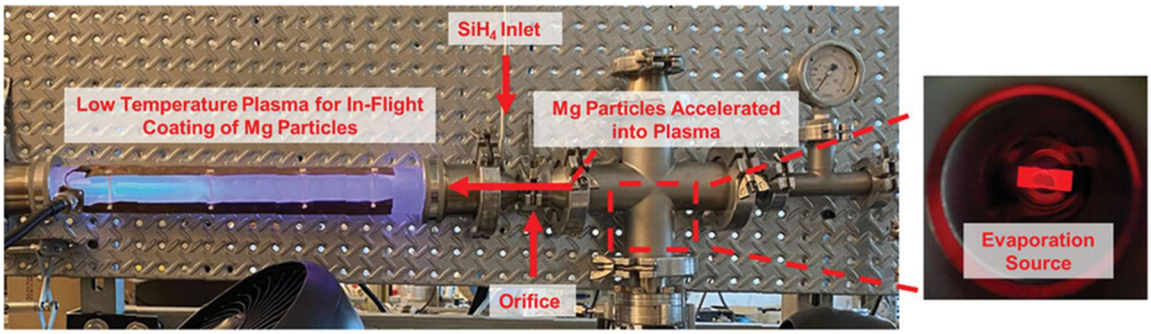


Figure 4: A photograph of the system that produces Mg nanoparticles with simultaneous Si coatings. Resistive heating utilizing a tungsten boat is used to sublimate Mg precursors as shown in the evaporation source on the right. An orifice allows acceleration of the Mg particles into the plasma reactor where the in-flight functionalization occurs. Reprinted with permission from [1]. Copyright (2023) Wiley-VCH.

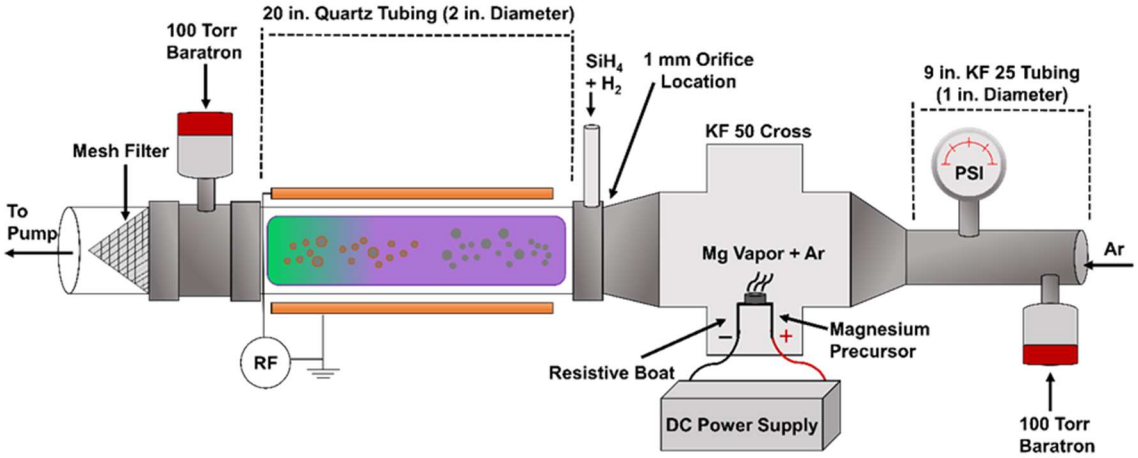


Figure 5: Schematic of the experimental setup specifying the dimensions and properties of each component. Reprinted with permission from [1]. Copyright (2023) Wiley-VCH.

In preparation for the nanothermite composite mixtures for ignition tests, Mg, Si, and coated Mg (Mg/Si–SiO_x) powders were added to the Bi_2O_3 oxidizer in hexanes

followed by ultrasonication to achieve three homogeneous mixtures. The samples were dried for 24 h under ambient conditions to obtain the thermite powders. Different fuel samples (Mg, Si, and Mg/Si–SiO_x) with stoichiometric equivalents of Bi_2O_3 oxidizer (fuel:oxidizer equivalence ratio, $\varphi = 1$) were mixed into nanothermite composites.

Ignition characteristics were investigated by temperature-jump time-of-flight mass spectrometry (T-Jump/ TOFMS) to probe the reaction mechanisms in the different energetic composites at high heating rates.[83, 246] The dispersed composites were coated on a Pt wire and resistively ignited using a rapid thermal pulse (~3 ms). The pulse heated the wire rapidly to ~1000–1200 °C, yielding a high heating rate of ~105 °C s^{-1}. The gas-phase product species evolved from the thermally activated reactions in the samples were ionized using a 70 eV electron gun and accelerated toward a multichannel plate detector maintained at ~1500 V. As a result, the mass spectra were obtained with a high temporal resolution (0.1 ms) and within timescales relevant to the rapid combustion reactions (~1 ms). For ignition characterization, the thermite composites were coated on a Pt wire in an argon atmosphere followed by resistive pulse heating ignition, as described above. Simultaneously, a high-speed camera (Vision Research Phantom V12.1) was used to record the ignition event. The current across the Pt wire was measured using a Teledyne LeCroy CP030A current probe to obtain the wire temperature, which was determined from the current–voltage relationship using Callendar−Van Dusen equation.[247, 248]

3.3: Materials Characterization

The morphology of the synthesized nanoparticles was characterized by scanning electron microscopy (SEM) with a ThermoFisher Scientific NNS450 microscope using a

20 kV accelerating voltage. Energy dispersive X-ray spectroscopy with an Oxford Instruments AztecSynergy Software and a 50 mm^2 X-Max50 SDD detector was utilized to obtain elemental analysis. A FEI Titan Themis 300 microscope was used to obtain high-angle annular dark-field (HAADF) images along with the elemental mapping of Mg, Si, and oxygen (O) content of the samples using the EDS detector. Transmission electron microscope (TEM) grids were prepared by ultrasonicating sample powder in isopropanol and drop-casting the particle solution onto lacey carbon grids. X-ray diffraction (XRD) via a PANalytical Empyrean Series 2 was performed to investigate the crystallinity and composition of the samples. X-ray photoelectron spectroscopy (XPS) by a Kratos AXIS Ultra DLD was carried out to examine the surface composition and oxidation states of the atoms at the nanoparticle surface. Differential scanning calorimetry (DSC) was performed using a Netsch STA449 F3 Jupiter analyzer to monitor the oxidation of samples with a slow heating rate of 10 °C min^{-1}. In situ TEM using a JEOL JEM-ARM300F Grand ARM TEM instrument was utilized to analyze structural and morphological evolution while heating (10 °C min^{-1}) under vacuum.

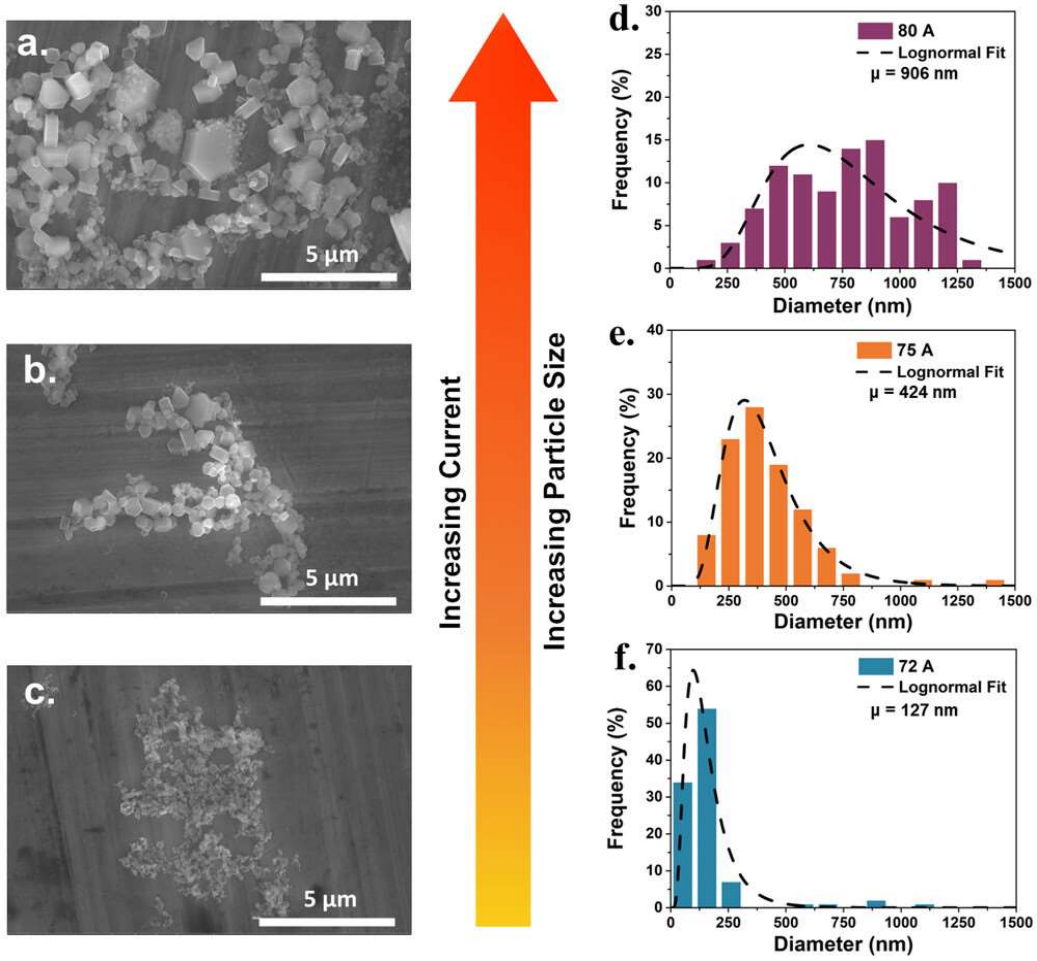


Figure 6: SEM images of Mg particles produced by thermal evaporation followed by gas-condensation using a) 80 A, b) 75 A, and c) 72 A of DC current with their correlated size distributions d–f). Reprinted with permission from [1]. Copyright (2023) Wiley-VCH.

First, SEM was used to analyze the morphology and size of the Mg nanoparticles synthesized via gas-condensation. **Figure 6a–c** shows the SEM images of Mg particles synthesized using various DC currents with their respective size distributions shown in **Figure 6d–f**. The crystals show hexagonal plate shapes, which is the thermodynamically favorable since the (0001) plane is close-packed and has the lowest free energy.[249] In order to completely show the hexagonal crystal structure of the Mg crystallites, we have performed XRD on these samples as shown in **Figure 7**. XRD confirms that the Mg nanoparticles possess a hexagonal crystal lattice structure with no impurities due to the absence of additional peaks. It is important to point out that the size of the particles increases as current supplied to the tungsten boat increases. The average nanoparticle size is ~120 nm, ~420 nm, and ~900 nm, at currents of 72, 75, and 80 A, respectively. The size distributions are reasonably well fitted with lognormal size distributions, a size distribution tendency that nanoparticles have when forming in aerosols. Expectedly, we observed a broadening of the size distribution with increasing current, with the geometric standard deviations (σ_g) being 1.5–1.6 for the three evaporation conditions. This is attributed to the increasing rate of Mg evaporation at higher currents (higher temperature), causing more saturation of Mg vapor within the evaporation chamber. The critical cluster size and free energy barrier for homogeneous nucleation is lower at larger saturation ratios, ultimately leading to an increase in particle number density and to an increased rate of particle coagulation.[250] The size distributions were calculated by measuring the diameters of 1000 hexagonal crystals synthesized at each current conditions, analyzing various TEM images in ImageJ software (version 1.53k). The estimated particle aspect ratio is roughly 0.35, and

we did not observe any quantifiable dependence of aspect ratio over current density. Uncoated Mg and Mg/Si–SiO_x nanoparticles were synthesized using 74 A of DC current, and the morphology of these nanoparticles was analyzed by TEM (**Figure 8a and 8b**). The average particle size for uncoated Mg and Mg/Si– SiO_x nanoparticles are 361 and 317 nm, respectively (**Figure 8c and 8d**)

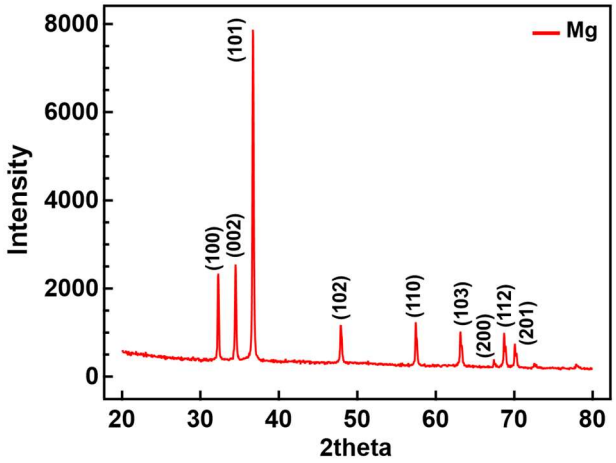


Figure 7: X-ray diffraction pattern of magnesium nanoparticles synthesized by thermal evaporation-gas condensation method showing hexagonal crystal structure. Reprinted with permission from [1]. Copyright (2023) Wiley-VCH.

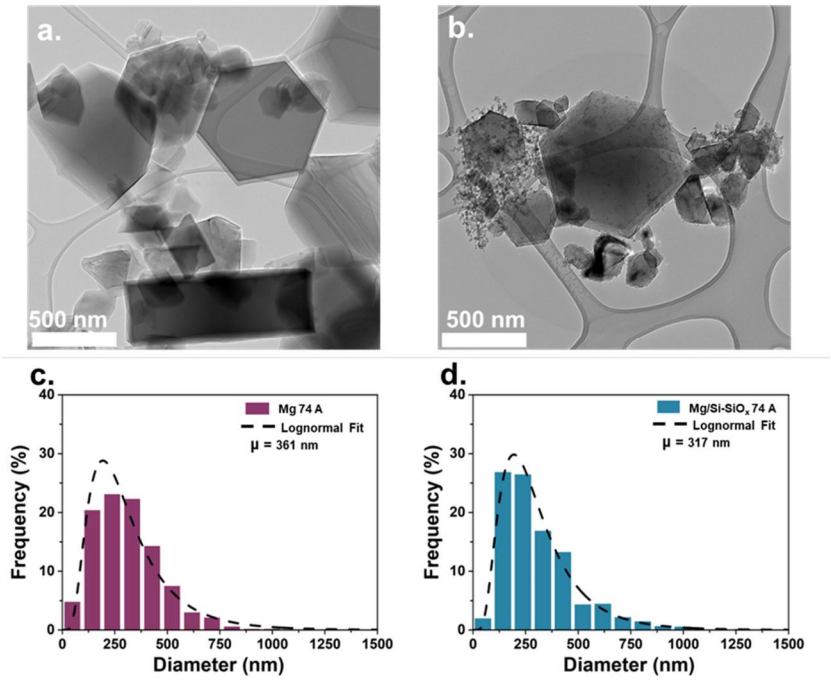


Figure 8: Transmission electron microscopy images of (a) uncoated Mg nanoparticles and (b) Si-coated Mg nanoparticles. Lognormal size distributions of (c) uncoated Mg nanoparticles and (b) Si-coated Mg nanoparticles. Reprinted with permission from [1]. Copyright (2023) Wiley-VCH.

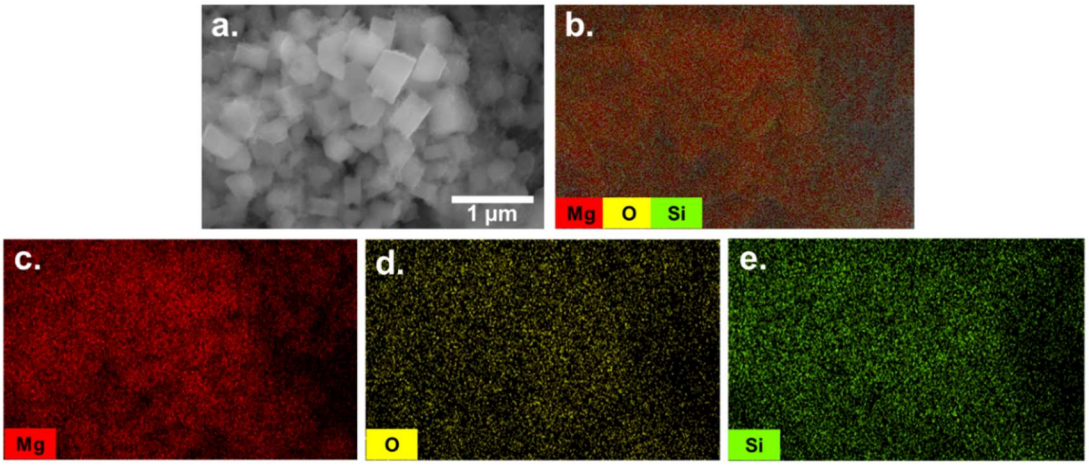


Figure 9: (a) Scanning electron microscopy image of Si-coated Mg nanoparticles. (b) Layered energy dispersive x-ray spectroscopy image of the Mg, O, and Si signals. (c) Mg, (d) O, and (e) Si images of the aforementioned signal. Reprinted with permission from [1]. Copyright (2023) Wiley-VCH.

SEM and EDS were used to confirm the morphology and composition of Mg/Si–SiO_x particles (**Figure 9**). The particles in the electron micrograph (**Figure 9a**) show hexagonal morphology with apparent surface roughness, which may be attributed to smaller Si particles residing at the Mg particle surface. This was confirmed by the EDS elemental maps shown in **Figure 9b–e** that show Mg particles coated with Si, and with small Si particles on the Mg surface. Compositional analyses suggest that the Mg-to-Si atomic ratio is 3:1. Characterization and analysis of the plasma coating were performed by STEM with EDS elemental maps in **Figure 10**. A uniform oxide shell is confirmed on uncoated Mg particles (**Figure 10a**). Pores are observed around the edges of Mg crystals, which is indicative of the porous nature of the MgO layer when the bare Mg nanoparticles are exposed to air. By comparison, STEM-EDS images of the Mg/Si–SiO_x particles (**Figure 10b**) suggest that the non-thermal plasma coating process is successful in applying a conformal Si shell around Mg particles. Based on STEM-EDS, the thickness of the Si layer on the Mg particles is ~15 nm.

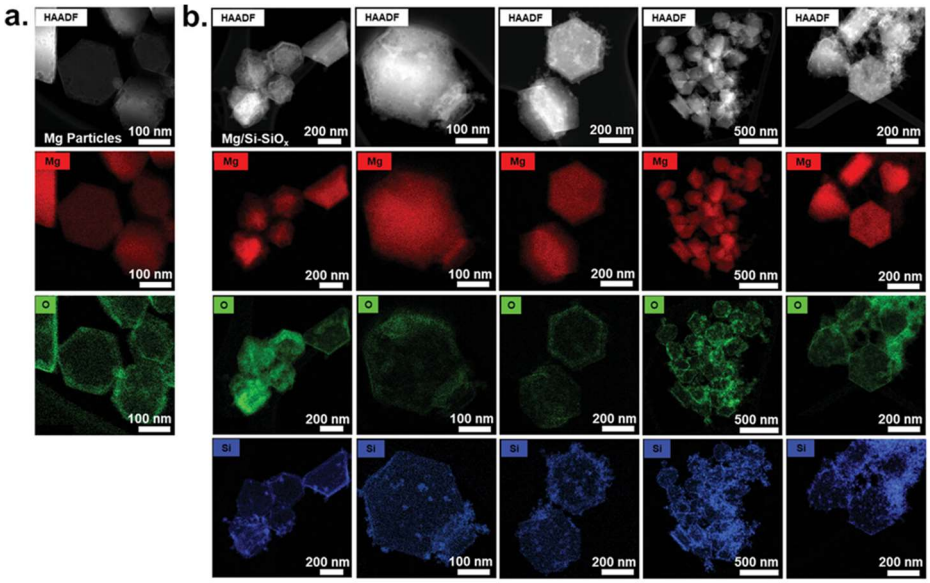


Figure 10: HAADF and STEM/EDS images of (a) uncoated Mg nanoparticles displaying a MgO shell and (b) Si-coated Mg nanoparticles displaying a partially oxidized Si coating. Reprinted with permission from [1]. Copyright (2023) Wiley-VCH.

XPS characterization was performed to analyze the surface chemical composition of Mg nanoparticles with and without the Si shell. The O 1s peak ~531 eV is shown in **Figure 11a**. To better understand the XPS results, we have also performed XPS analysis on uncoated Mg nanoparticles and on Si nanoparticles produced using the same reactor without the presence of Mg nanoparticles in order to nucleate Si nanoparticles. For the Si-coated Mg, we find contributions from both Si-O at ~532 eV[251] and Mg-O at 531 eV,[252] although the dominant contribution is from Si-O suggesting that most of the oxygen is bound to silicon for the coated Mg nanoparticles. The Si 2p peak ~100 eV is shown in **Figure 11b** for both the coated Mg nanoparticles and for the Si control. For the control, we can identify two peaks assigned to ground state Si at 99.5 eV and to SiO at 101.6 eV.[253] The Si 2p spectrum for the Mg/Si–SiO_x particles is more complex. We observe additional peaks, which we attribute to Mg_2Si at 98.4 eV and to SiO_2 at 103.1 eV.[253, 254] This suggests

that the silicon-based coating is oxidized, with contributions from both SiO and SiO_2 bonding. It also suggests that some of the silicon is bound directly to Mg, which is to be expected given the fact that the coating is applied before the particles are ever exposed to air. For completeness, we also show the Mg 2p peak ~50 eV for the Mg control case and for the coated particles in **Figure 11c**. For the control case, we find two peaks corresponding to ground state Mg at 49.5 eV and MgO at 50.8 eV.[255] There is a slight blueshift for the Mg/Si–SiO_x particles, which in a counterintuitive manner suggests that the magnesium is more oxidized for the in-flight coated particles. Given the high degree of silicon oxidation, oxygen can diffuse through the shell and still reach the magnesium core. We should point out that the Mg 2p signal is quite low for the case of the coated particles because the Mg is buried underneath the SiO_x layer. Because of this, the XPS analysis is more sensitive to the outermost portion of the Mg core, i.e., the one that is reached by oxygen. This explains the higher contribution from MgO bonding for the coated particles compared to the control sample (Mg nanoparticles containing a native oxide shell). Overall, the combination of STEM-EDS and XPS confirms the successful coating of the Mg particles with a silicon-based shell. The shell is oxidized upon exposure to air. Direct bonding between Mg and Si is present at the interface between the Mg core of the silicon-based shell.

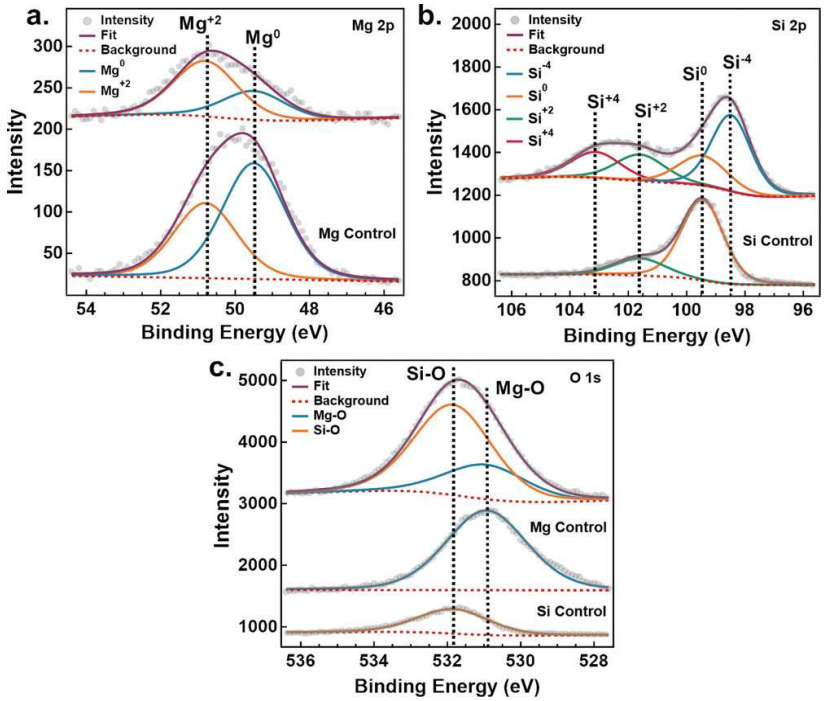


Figure 11: XPS of the Mg/Si–SiO_x particles, Mg control, and Si control showing the a) O 1*s* peaks, b) Si 2*p* peaks, and c) Mg 2*p* peaks. Reprinted with permission from [1]. Copyright (2023) Wiley-VCH.

3.4: Energetic Performance

Tjump-TOFMS and high-speed camera snapshots during combustion with an oxidizer in vacuum.[246, 256] In a recent study regarding the ignition of Mg nanoparticles with different oxidizers, the results showed that the availability and release of Mg vapor directly impacted ignition and energetic performance.[71] Oxidizers, such as Bi_2O_3 and copper oxide (CuO) decompose after the release of Mg vapor. As a result, using Bi_2O_3 as the oxidizer allows us to probe how surface modification affects the reaction rate-limiting step, i.e., the release of Mg vapor.[257] Different fuel samples (uncoated Mg and Mg/ SiO_x) prepared with the plasma reactor are incorporated with stoichiometric equivalents of Bi_2O_3 oxidizer (fuel:oxidizer equivalence ratio, $\varphi = 1$) into nanothermite composites. The coated samples

were also characterized against Mg and Si controls to investigate the effects of surface modification on ignition and reaction mechanism. The Si control was synthesized under the same plasma reactor conditions used for the Mg/Si–SiO_x nanoparticles, but without supplying current to the thermal evaporator, hence eliminating Mg particles in the process. A constant equivalence ratio ($\varphi = 1$) is maintained for all the samples.

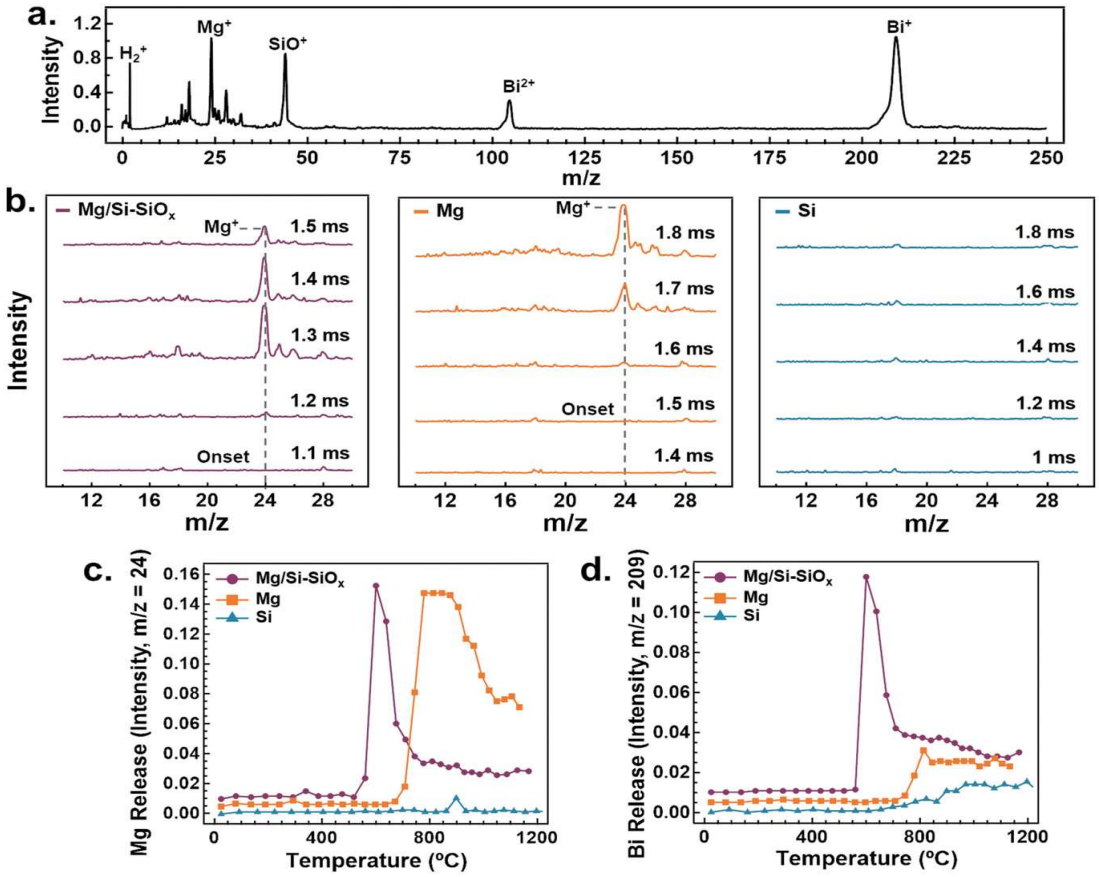


Figure 12: a) Tjump-TOFMS full spectrum data for the Mg/Si–SiO_x nanoparticles. b) Timed spectra for Mg/Si–SiO_x nanoparticles, Mg control, and Si control samples showing the evolution of Mg (m/z = 24) release. The c) Mg release profiles, and the d) Bi release profiles for Mg/Si–SiO_x nanoparticles, Si control, and Mg control. Reprinted with permission from [1]. Copyright (2023) Wiley-VCH.

Figure 12a is a representative full spectrum of the TJump/ TOFMS, showing the combustion product species evolved during ignition of the coated Mg sample. The Mg release over time for Mg/Si–SiO_x nanoparticles, uncoated, and Si nanoparticles are shown in **Figure 12b**. There is no Mg release from the Si control since there is no Mg present. The Mg release onset for the coated Mg occurs ~0.4 ms earlier than the uncoated Mg. **Figure 12c and 12d** provides the temporal release of Mg and bismuth (Bi) when samples are rapidly heated until combustion, respectively. Both Mg and Bi were released earlier and at lower temperatures for the coated samples compared to uncoated Mg and Si. The snapshot images of ignited Si, uncoated Mg, and coated Mg nanoparticles are shown in **Figure 13a–c**, respectively. The ignition temperature, as obtained from high-speed imaging, showed that optical emission occurs at a significantly lower temperature for Mg/Si–SiO_x nanoparticles (~520 °C) compared to non-coated Mg (~740 °C). The ignition of the coated Mg nanoparticles completes in ~0.1 ms as opposed to ~0.3 ms for the uncoated Mg, suggesting reduced ignition thresholds for coated particles. The Si nanoparticles do not show any significant combustion, ruling out the contribution from Si itself to the overall energetic reaction. Additionally, the decomposition of Bi_2O_3 results in the release of gaseous Bi at temperatures above 870 °C.[257] The early onset of both Bi and Mg release for the Mg/Si–SiO_x nanoparticles is consistent with a localized exothermic reaction, which accelerates combustion. Overall, the Tjump-TOFMS data along with the snapshots from the high-speed camera conclusively shows that the non-thermal plasma surface modification has a direct and beneficial effect on the energetic performance of the fuel particles. Size effects can be ruled out for the observed reduced ignition onset because

the difference in average size between the uncoated Mg and the Mg/Si–SiO_x nanoparticles is minimal, as shown in **Figure 8**. As found in previous work, the difference in ignition temperature for 500 and 40 nm Mg particles is ~140 °C,[71] a significantly smaller temperature difference compared to the ignition temperature reduction seen from our coated nanoparticles.

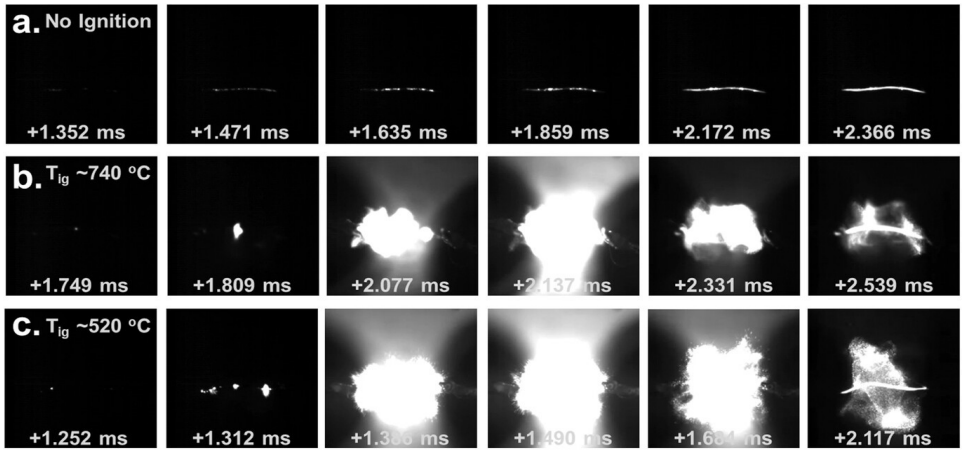


Figure 13: Ignition snapshots from the Tjump visualized from a high-speed camera for (a) Si nanoparticles, (b) uncoated Mg nanoparticles, and (c) Si-coated Mg nanoparticles. All samples were mixed separately with Bi_2O_3 to create nanothermite composite mixtures. Reprinted with permission from [1]. Copyright (2023) Wiley-VCH.

The ignition mechanisms were further investigated by DSC in an ultra-high purity argon environment, as shown in **Figure 14a**. The products were analyzed via XRD, see **Figure 14b**. The as produced particles show the expected Mg peaks according to the hexagonal close-packed crystal structure with the major peak at 36.8° corresponding to the (10–11) plane, and a small Mg_2Si peak at ~40° according to the (220) plane. We did not observe any peak from silicon, suggesting that the shell is amorphous. DSC shows a first exotherm upon heating to ~400 °C. The corresponding XRD spectrum indicates that the Mg peaks are reduced while the Mg_2Si peaks increase in intensity. This correlates with a

condensed-phase alloying reaction occurring at the interface between the Mg core and the Si–SiO_x shell. Further heating to 750 °C leads to a second exotherm, with the corresponding XRD showing peaks from Si with the major peak at 28.2° according to the (111) plane, and from MgO with the prominent peak at 42.4° according to the (200) plane. Therefore, we interpret this second exothermic reaction as the magnesiothermic reduction of the oxidized silicon shell by the Mg core.

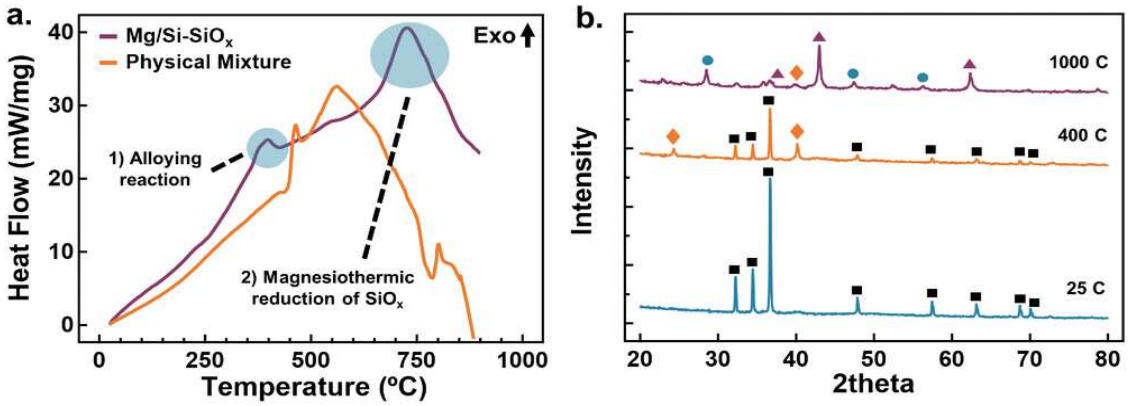


Figure 14: a) DSC profile for Mg/Si–SiO_x particles performed in ultra-high purity Ar. b) XRD of the Mg/Si–SiO_x samples heated to 400 and 1000 °C and analyzed against an unheated sample. The blue circles, black squares, purple triangles, and orange diamonds indicate Si, Mg, MgO, and Mg_2Si, respectively. Reprinted with permission from [1]. Copyright (2023) Wiley-VCH.

The combination of DSC and XRD data suggests that there is a two-step ignition process for Mg/Si–SiO_x samples, as indicated by **Equation 6 and 7**.[258, 259] The calculated adiabatic temperatures for the reduction of SiO_2 by Mg can reach ~2300 °C,[260, 261] and Mg_2Si formation can reach ~1000 °C,[262, 263] supporting the conclusion that the heat generated by the reaction between Mg core and the Si–SiO_x shell is more than sufficient to trigger Mg release and initiate combustion when mixed with Bi_2O_3. The onset temperature

of magnesiothermic reduction has been reported over a wide range of values, where onset temperatures are expected from ~460 °C to above ~650 °C, and the reaction heightens when the Mg vapor pressure is sufficiently high to diffuse into SiO_2.[260, 264, 265] Below 650 °C, a solid-state reaction occurs that includes the formation of Mg_2Si.[264] We observe the formation of Mg_2Si for the coated Mg nanoparticles at a lower temperature of ~400 °C, which suggests the close proximity of Si at the interface allows a lower reaction onset temperature.

$$2Mg\ (s) + Si\ (s) \rightarrow Mg_2Si\ (s) \qquad \Delta H_r = -78\ kJ\ mol^{-1}$$

Equation 6: The heat release from Mg_2Si alloy formation.

$$2Mg\ (s) + SiO_2\ (s) \rightarrow 2MgO\ (s) + Si\ (s) \qquad \Delta H_r = -292\ kJ\ mol^{-1}$$

Equation 7: The heat release according to the magnesiothermic reduction of silica.

Additionally, we have performed DSC on a physical mixture of Si nanoparticles containing a native oxide layer and uncoated Mg nanoparticles to investigate whether the intimate contact between the Mg particle fuel and the partially oxidized Si shell has an effect on lowering the ignition temperature. Two exotherms are apparent in the DSC curve; however, they occur at higher temperatures compared to the in-flight coated samples. Therefore, we conclude that the reduced reaction onset temperature for Mg/Si–SiO_x nanoparticles (~400 °C) observed in DSC can be attributed to the direct contact between the Mg core and the partially oxidized Si layer, allowing shorter diffusion lengths, faster kinetics, and lower onset of the exothermic reaction. The quicker Mg and Bi release from

the coated Mg nanoparticle interacting with the Bi_2O_3 primary oxidizer ignition observed in the T-jump/TOFMS (see **Figure 12**), can therefore be attributed to interfacial reactions enabling the release of Mg vapor at a lower temperature, resulting in earlier reaction onset between Bi_2O_3 and Mg.

Finally, we have performed in situ TEM analysis to monitor changes in particle morphology during heating in vacuum under slow heating (10 °C min^{-1}), similar to the heating rate used in the DSC experiment. The in-situ TEM videos of non-coated Mg nanoparticles and Mg/Si–SiO_x nanoparticles are provided in **Videos 1 and 2**, respectively. **Figure 15a and 15b** depict snapshots at different temperatures of Mg/Si–SiO_x nanoparticles and Mg nanoparticles, respectively. For both cases, we observe outward-diffusion of Mg resulting in hollowing of the particles, consistent with recent findings from Ghildiyal et al.[71] The onset of core vaporization of Mg for the coated particles occurs at ~240 °C compared to ~340 °C for uncoated Mg particles. This is consistent with the data shown in **Figure 14**. Early access to the Mg fuel explains the decreased ignition and release temperatures for the reaction of Mg/Si–SiO_x nanoparticles with Bi_2O_3 (**Figure 12**). It is important to point out that while the hollowing of the Mg/Si–SiO_x nanoparticles starts considerably earlier compared to the Mg nanoparticles, it also finishes at ~350 °C, corresponding to a ΔT of 110 °C. Hollowing of the Mg nanoparticles finishes at ~355 °C, which is15 ° of 15 °C. The localized release of energy at the Mg core/Si–SiO_x shell interface leads to Mg vaporization at a lower temperature, although outward-diffusion of Mg seems slower for the case of the coated sample. This is likely due to the presence of a thicker shell for the case of the in-flight coated material. It is important to note that the

evaporation of the Mg core occurs at a much lower temperature (~240 °C) than the oxidation onset observed by DSC (~400 °C). The sample size for in situ TEM studies is considerably smaller (a handful of particles) compared to DSC (several mg of powder characterized at once). A study by Mahadevan et al. shows that decreasing sample size influences the measured reaction kinetics due to heat and mass transport effects.[266] In situ TEM measurements can increase the particle temperature up to 200 K, which could be another reason for the earlier Mg evaporation temperature than the Mg release and oxidation onset temperatures from T-jump/TOFMS and DSC, respectively.[267] A schematic summarizing the ignition mechanism of non-coated Mg nanoparticles versus Mg/Si–SiO_x nanoparticles is outlined in **Figure 15c**. For the case of Mg with a native oxide shell, the metal vaporizes within the core and diffuses outward through a porous oxide shell to react with an oxidizer. For the coated sample, the Mg core is surrounded by a partially oxidized Si layer. Upon heating, an intermetallic reaction takes place first followed by the magnesiothermic reduction of the oxidized shell. These reactions are exothermic with high predicted adiabatic temperatures, triggering the early release of Mg vapor and further reaction with the surrounding oxidizer.

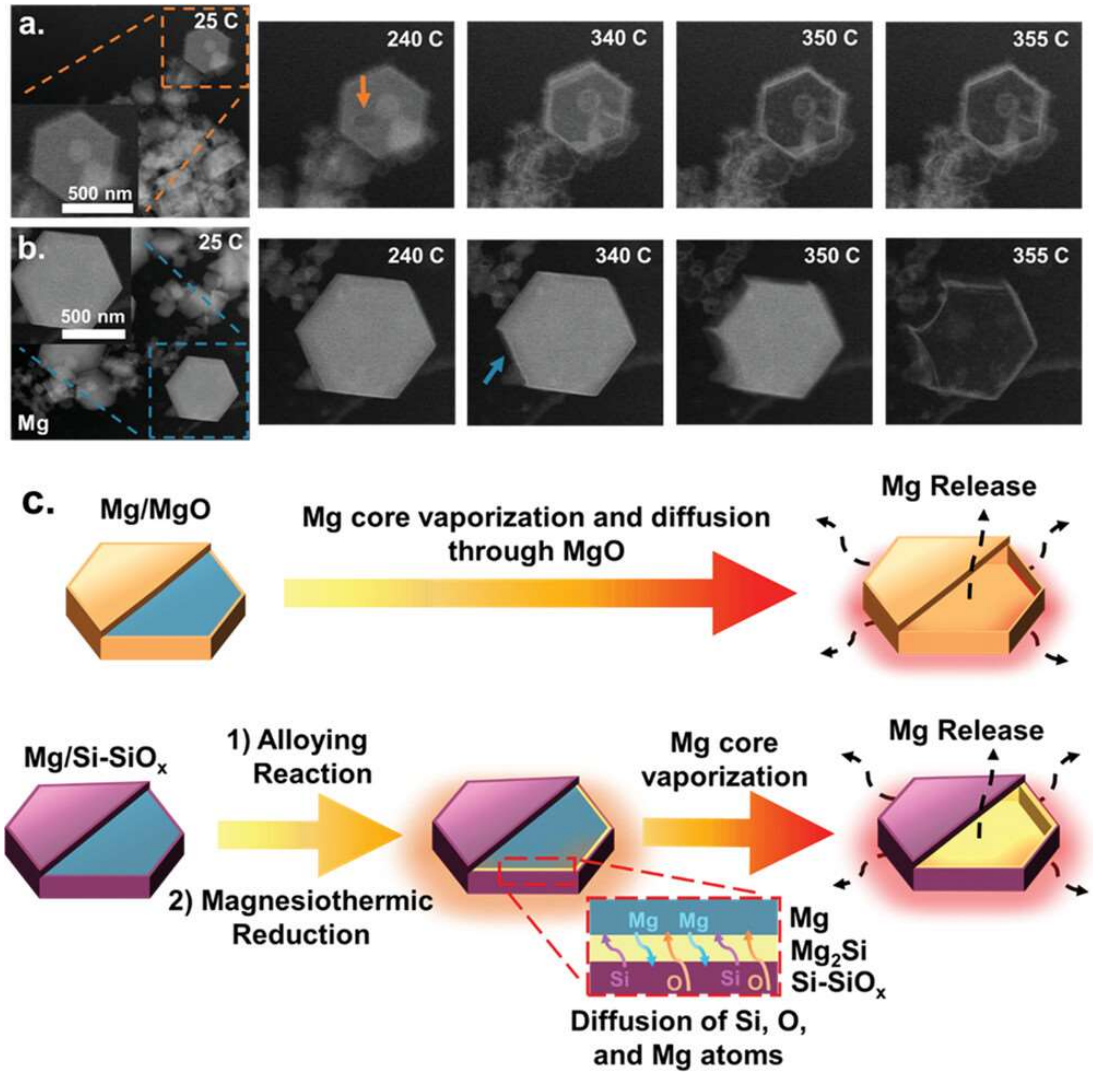


Figure 15: In situ TEM micrographs of a) Mg/Si–SiO_x nanoparticles and b) Mg nanoparticles under a heating rate of 10 °C min^{-1}. c) Schematic showing the ignition pathways for Mg and Mg/Si–SiO_x particles. Reprinted with permission from [1]. Copyright (2023) Wiley-VCH.

3.5: Summary

In conclusion, we have investigated the surface modification of magnesium nanoparticles and its effect on the material combustion properties. We have leveraged the capabilities of low-temperature plasmas to apply a conformal silicon-based coating onto the surface of magnesium nanoparticles. This is done in-flight, immediately after the nucleation and growth of the magnesium particles and before exposure to air. We demonstrate that the ignition temperature and the reaction rate of Mg particles with Bi_2O_3 can be considerably altered by the presence of a silicon-based shell. Differential scanning calorimetry, detailed structural analysis by XRD and in situ TEM during heating in an inert environment confirm both the formation of magnesium silicide and the occurrence of a magnesiothermic reaction between the magnesium core and the silicon oxide shell. T-jump measurements confirm that the coated particles show a significant reduction in ignition temperature (>200 °C) during combustion with Bi_2O_3, consistent with an earlier onset of release of Mg vapor from the fuel particles when these are coated with the silicon-based shell. This work demonstrates that improvements in the combustion of Mg particles, which have received less attention than the more widely investigated Al, are easily within reach with the appropriate surface modification approach. We stress that further improvements are likely within reach by further optimization of coating thickness and magnesium core size.

Section 4: Plasma-Induced Hydrogenation of Magnesium

4.1: Introduction

Magnesium hydride (MgH_2) is a potential solid-state hydrogen storage material because of its high capacity (7.6 wt %), which exceeds the standards set by the U.S. Department of Energy for hydrogen storage materials.[268-271] MgH_2 is also a promising candidate for combustion-related applications due to its high combustion enthalpy and hydrogen content. For instance, metal hydrides are attractive additives in solid rocket propellants since they have been shown to improve combustion performance.[205, 272] Oxidation of hydrogen gas (H_2) is highly exothermic, contributing to the overall energy release during the ignition of solid metal fuels.[273] One study found that combining metal hydrides with boron particles enhances the ignition by releasing heat, thus increasing the temperature of boron and facilitating its burning.[274] The effects of titanium hydride (TiH_2), zirconium hydride (ZrH_2), and MgH_2 on combustion were studied previously, in which the addition of the metal hydrides resulted in more intense flames and higher combustion rates.[275] Particularly, the sample with MgH_2 as an additive had the highest combustion rate compared to those of TiH_2 and ZrH_2. The ignition behavior of aluminum hydride (AlH_3) microparticles was investigated, finding that their ignition threshold was considerably lower than aluminum (Al) microparticles.[276] Micrometer-sized AlH_3 exhibited ignition behavior similar to nanoscale Al particles. Among the existing metal hydrides, MgH_2 is particularly attractive for fuel additives because of its high hydrogen storage capacity, along with it releasing H_2 gas and magnesium (Mg) vapor during ignition, generating large amounts of pressure.[277, 278]

Particle agglomeration and sintering are common issues when using nanosized particles for ignition purposes.[213] Previous studies have suggested that gas generation during the ignition of nanoparticles can alleviate these problems by propelling particles apart, preventing agglomeration, and allowing the complete combustion of the nanoparticle fuel.[83, 225, 279] Aluminum-based mesoparticles loaded with a gas-generating binder, nitrocellulose, was explored and found that sintering was minimized during ignition to allow full combustion of the particles.[280] For biocidal purposes, gas generators are important for dispersing a biocidal to the deactivation area of biological weapons.[281] To summarize, the hydrogenation of nanofuels is beneficial for both combustion kinetics and gas generation, thus providing an additional handle for the optimization of energetic formulations.

Several methods have been implemented to prepare MgH_2. Mechanochemical ball milling is a typical approach to prepare MgH_2 from a Mg precursor; however, this method generally requires high pressures (several MPa) and relatively high temperatures exceeding 300 °C while using catalysts.[282-284] Additionally, lengthy production times are necessary for complete hydrogenation by this process. Plasma-assisted ball milling is an enhanced technique that allows the production of Mg-based alloys containing MgH_2 for hydrogen storage applications. The use of plasma enables electron and ion bombardment of the metal precursors that facilitates the formation of hydrogen storage alloys in shorter processing times.[285-287] The thermodynamics and kinetics of H_2 desorption can be tuned by alloying other metals with Mg.[288] A Magnesium fluoride (MgF_2) doped Mg–In alloy was synthesized to maintain a high hydrogen storage capacity while lowering the activation

energy for H_2 desorption.[289] MgH_2–Ni composites were produced through a similar method and found that dehydrogenation can occur at temperatures as low as 225 °C, almost 200 degrees lower than the original desorption temperature of H_2 from MgH_2.[290] MgH_2 films have been produced by plasma-assisted physical vapor deposition, in which synthesis occurs in a low-pressure environment.[291, 292] The process involves lower temperatures and shorter hydrogenating times compared with other methods.

Nonthermal plasmas can process various materials at near room temperature and low pressures (1–10 Torr).[38, 231, 293-296] Free electrons with temperatures in the 1–5 eV range can activate a broad range of chemistries, even while the gas remains close to room temperature, including in the case of the nucleation of nanoparticles. An additional advantage of low-temperature plasmas is the electrostatic stabilization of nanoparticles dispersed within them.[238, 240] This effect prevents agglomeration, allowing the functionalization of individual particles on-the-fly, as opposed to agglomerates. For example, low-temperature plasmas have been used to apply surface coatings on nanoparticles in-flight to produce a conformal Si-based shell around Mg core particles for accelerated ignition.[1] Silicon nanoparticles synthesized by low-temperature plasmas are widely studied materials. A recent work produced crystalline and amorphous Si nanoparticles by varying the plasma power and studied their effects on ignition.[66] Because amorphous Si contains more hydrogen-terminated Si on the surface, more pressure generation was observed due to increased amounts of H_2 gas released from the particles. Other work shows that Al nanoparticles can be treated with hydrogen to dope the oxide layer with aluminum hydride (AlH_3).[212] The surface oxide shell was doped with H_2, which

desorbed H_2 gas upon heating or burning. The results showed that H_2 gas generation increased the heat release during combustion by exposing more aluminum, providing a pathway for oxygen to diffuse to and react with the oxidizer upon heating. The reduction of the oxide shell around Al by hydrogen plasma treatment negates the diffusion barrier abilities of Al_2O_3.

In this second work of the dissertation, Mg nanoparticles produced by the gas-condensation method are subjected to in-flight hydrogen plasma treatment to synthesize MgH_2-containing (h-Mg) composite nanoparticles. To the best of our knowledge, there are no reports of MgH_2 produced by low-temperature plasma treatment for combustion-related applications. The effects of plasma processing on the hydrogen content and ignition kinetics are investigated. Process characterization suggests that in-flight hydrogenation is due to the high density of atomic hydrogen achieved by low-temperature plasma. Diffusion of atomic hydrogen into the magnesium lattice results in the formation of particles with MgH_2 in their outer layer, as confirmed by careful transmission electron microscopy analysis. Combustion was tested against untreated Mg nanoparticles produced without plasma treatment with a potassium perchlorate ($KClO_4$) oxidizer to examine the effects of H_2 gas release on the ignition mechanism. The results discussed in this contribution show that H_2 gas release reduces the ignition threshold of the nanothermite mixtures, consequently enabling the faster release of the Mg fuel for combustion.

4.2: Experimental Methods

The experimental setup is similar to the work outlined in **Section 3**. Magnesium nanoparticles were prepared by the gas condensation of Mg vapor and exposed to a low-temperature hydrogen plasma for hydrogenation, as shown in **Figure 16**. Bulk Mg precursor (~250 mg, disc shape, 1.2 cm diameter, and 1 mm thickness) was resistively heated while high-purity argon (Ar) was flown (350 sccm) as a carrier gas. The pressure in the evaporation chamber was ~40 Torr. The Mg-laden aerosol was injected into the plasma reactor by flowing through an orifice while high-purity H_2 gas was introduced at 30 sccm for hydrogen treatment. The plasma reactor consisted of 2" × 20" quartz tubing and copper parallel plate electrodes connected to a radio frequency (RF) power supply and matching network. The RF power at 13.56 MHz was varied, while the pressure was maintained at 3 Torr in the plasma reactor. Based on flow velocity, the estimated residence time of the Mg-laden aerosol in the plasma reactor was ~185 ms. The samples were collected downstream of the plasma reactor onto a stainless-steel mesh filter in vacuum. The nanoparticles were removed from the vacuum system by slowly leaking air to prevent ignition.

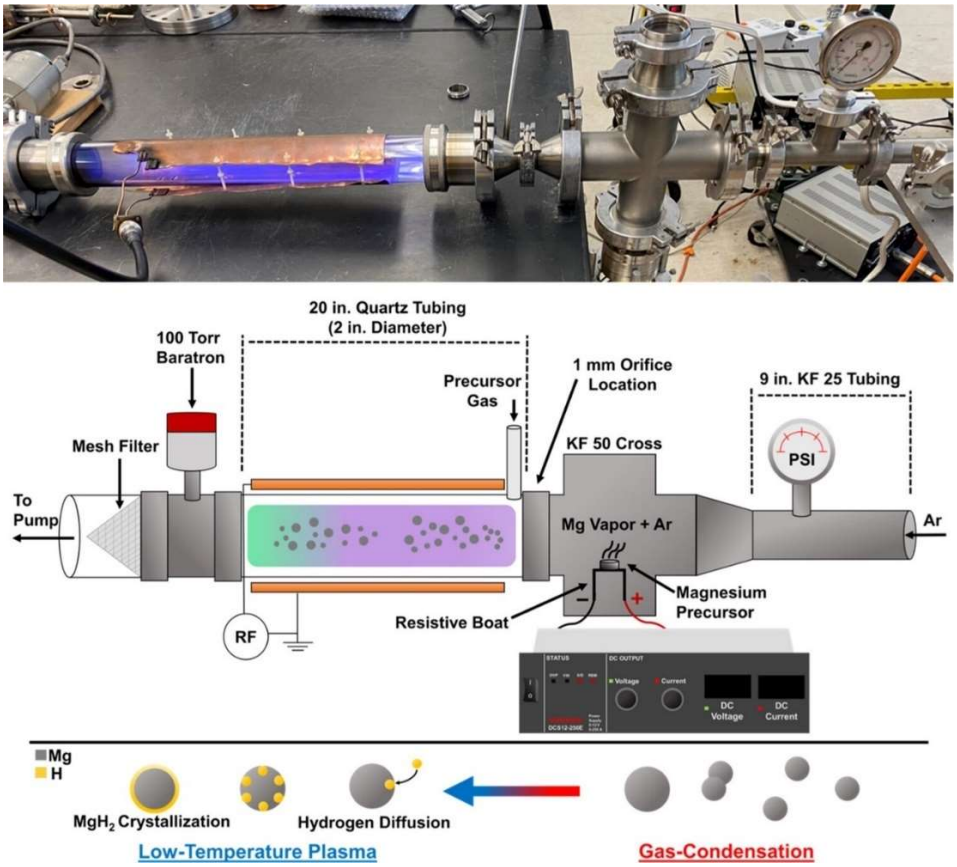


Figure 16: Photograph and schematic of the thermal evaporation and nonthermal hydrogen plasma system. Gas-condensation of thermally evaporated Mg nucleates Mg nanoparticles. A hydrogen plasma is utilized to create atomic hydrogen that continues on to diffuse into the Mg lattice and form crystalline domains of MgH_2. Reprinted with permission from [2]. Copyright (2023) American Chemical Society.

Preparation of the nanothermite composite mixtures were made in the following way. Mg and h-Mg powders were mixed with the $KClO_4$ oxidizer in hexanes and ultrasonicated to obtain homogeneous thermite mixtures. The mixtures were dried under ambient conditions for 24 h until the hexanes solvent was evaporated and collected for ignition testing. Each fuel sample was prepared with stoichiometric equivalents of the $KClO_4$ oxidizer (fuel:oxidizer equivalence ratio, $\phi = 1$) and mixed into nanothermite composites.

Temperature-jump time-of-flight mass spectrometry (T-jump/TOFMS) was used to investigate the gaseous products produced during ignition, as well as their time-resolved release and ignition temperature. The sample mixtures were coated onto a platinum (Pt) wire and resistively heated with a rapid pulse (~3 ms) to ~1200 °C, which resulted in a high heating rate of $\sim 10^5$ °C s^{-1}. The current applied to the Pt wire was measured using a Teledyne LeCroy CP030A current probe to obtain the wire temperature, which is attained from the current–voltage relationship from the Callendar–Van Dusen equation. Gaseous products created from ignition reactions were ionized using a 70 eV electron gun and were accelerated toward a multichannel plate detector maintained at ~1500 V. Mass spectra were recorded with a high temporal resolution (0.1 ms) to probe the relevant time scales of fast combustion reactions (~1 ms). The T-jump/TOFMS instrument was equipped with a high-speed camera (Vision Research Phantom V12.1) to record the ignition events.

Optical emission spectroscopy (OES) was used to characterize the excited species in the plasma based on the light emitted during processing. A fiber-optic cable was positioned perpendicular to the plasma reactor tube to collect light and pass it to a

monochromator (Princeton Instruments, Acton SpectraPro SP-2750). Emission spectra are acquired and processed by LightField software. Plasma emission from 500 to 800 nm is measured to obtain the emission line intensities with respect to Mg, H_2, and Ar.

4.3: Materials Characterization

X-ray diffraction (XRD) was performed (PANalytical Empyrean Series 2) to analyze the crystallinity and composition of the samples. Curve fitting by the Rietveld refinement method was used using Profex (version 5.2.0) software in order to obtain semiquantitative material composition of MgH_2 and Mg composition within the h-Mg samples. Particle morphology was analyzed using a ThermoFisher Scientific NNS450 scanning electron microscope (SEM) using a 15 kV accelerating voltage. An FEI Titan Themis 300 transmission electron microscope (TEM) was used to obtain high-resolution transmission electron microscopy (HR-TEM) images. The TEM grids were prepared by ultrasonicating the powder samples in isopropanol for 2 min and drop-casting the dispersed solution onto lacey-carbon grids. The average size and size distributions were obtained by measuring 1000 particles from each sample from TEM images in ImageJ software (version 1.53k). Temperature-programmed desorption (TPD) was performed to verify hydrogen content in the nanopowders. About 50 mg of h-Mg powder was loaded onto an alumina boat and placed into the center of a 1-inch quartz tube and heated using a furnace f to 550 °C with a 10 °C min^{-1} heating rate. A residual gas analyzer (RGA) was used to determine the composition of the gas downstream of the heated region. The hydrogen signal at amu = 2 was carefully corrected by removing the contribution from moisture. This was done by

acquiring a background mass spectrum with argon flowing through the system to determine the ratio between the water signal at amu = 18 and the hydrogen signal at amu = 2 from the water dissociation. Thermogravimetric analysis (TGA) and differential scanning calorimetry (DSC) were performed by using a Netsch STA449 F3 Jupiter analyzer to monitor the slow oxidation of nanoparticles with a heating rate of 10 °C min^{-1}.

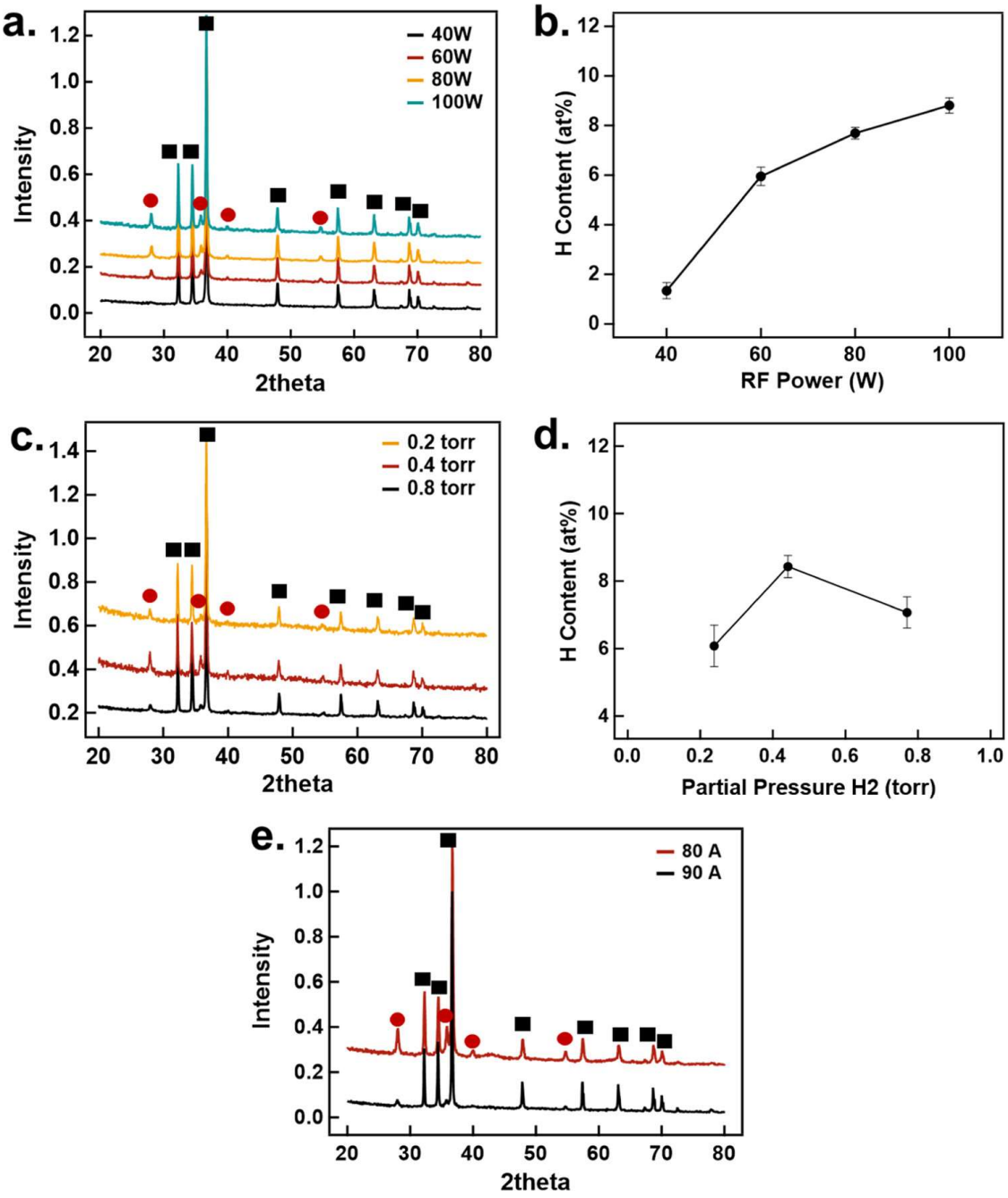


Figure 17: XRD patterns of h-Mg nanoparticles produced using (a) an RF power of 40–100 W and (c) partial pressure of H_2 and their respective H content (b, d). XRD patterns of nanoparticles made with low (80 A) and high (90 A) currents are shown in panel (e). Red circles denote MgH_2 planes, and black squares denote Mg planes in the XRD patterns. Reprinted with permission from [2]. Copyright (2023) American Chemical Society.

XRD was used to analyze the composition and crystallinity of the h-Mg nanoparticles synthesized by various RF powers (**Figure 17a**) and partial pressure of H_2 (**Figure 17c**). Rietveld Refinement was used to determine the Mg and MgH_2 composition according to the RF power and partial pressure of H_2 in weight percent, from which the atomic percentages of H were calculated (**Figure 17b and 17d**). Increasing RF power from 40 to 100 W raises the overall H content within the h-Mg nanoparticles from 2 to 8 atom %, with the increase leveling off at a high RF power. This confirms the ability of the low-temperature plasma to achieve substantial hydrogenation of the Mg particles. The plateauing of hydrogen content at a higher RF power and plasma intensity will be discussed in detail later in the dissertation. It is likely the consequence of nanoparticle heating exceeding the hydrogen desorption temperature of MgH_2 within the plasma, limiting the hydrogen content in the material. With respect to gas composition, an optimal H_2 partial pressure of 0.4 Torr produces the largest degree of hydrogenation at a constant power of 100 W. Increasing the flow of molecular hydrogen beyond this level is actually detrimental to producing more MgH_2. This result is unsurprising, as an excessive fraction of H_2 gas in the plasma is expected to quench it due to energy transfer to vibrational and rotational excitation of H_2. TPD was used to assess the accuracy of the MgH_2 content obtained through the Rietveld Refinement fitting method. A sample consisting of 16.7 atom % MgH_2 was produced using 82 A of current and an RF power of 80 W, containing 0.372 mmol of H_2 for 55 mg of powder. TPD showed that the volume of H_2 desorbed from the particles was 7.9 cm^3 (**Figure 18**). **Equation 8-10** show the calculations that were used in order to estimate the mmol of H_2 within the h-Mg nanoparticles containing 16.7 at. %

MgH_2. **Equation 11** shows the calculation according to the experimental recording of volume of H_2 analyzed by TPD. The volume was calculated by integrating the area underneath the flow rate vs. time plot, which equated to 0.355 mmol of H_2 and is in reasonable agreement with the amount obtained by Rietveld refinement. The results show that the Rietveld refinement is a reliable technique to estimate the fraction of MgH_2 within the h-Mg nanoparticles, from which the H content can be calculated. We have also found that the overall production rates of the h-Mg nanoparticles are strongly dependent on the RF power (**Figure 19a**). When the power is 40, 60, 80, and 100 W, the production rates are 16, 8, 7, and 6 mg h^{-1}, respectively. The production rate drops considerably at higher plasma power. **Figure 19b** shows the plasma reactor tube before synthesis. After synthesis, there is noticeable film growth onto the plasma reactor tube at 80 and 100 W of RF power (**Figure 19c and 19d**). The high amount of film growth at a high RF power is indicative of Mg losses to the walls of the reactor, consistent with the production rate of h-Mg nanoparticles being strongly dependent on plasma power. Finally, we have found that the MgH_2 content in the nanoparticles is strongly dependent on the particle size. Reducing the current in the evaporation step from 90 to 80 A results in nanoparticle sizes decreasing from 400 to 130 nm on average, respectively (**Figure 20a and 20b**). 500 particles were measured for both samples in ImageJ software from SEM images to obtain the average sizes. The corresponding XRD patterns are shown in **Figure 17e**. Rietveld Refinement indicates that the atomic fraction of MgH_2 increases from 7.4 to 23.5 atom % when decreasing particle size.

$$\frac{17.8\ wt.\%\ of\ MgH_2 \div 26\frac{g}{mol}}{\left(17.8\ wt.\%\ of\ MgH_2 \div 26\frac{g}{mol}\right) + (82.2\ wt.\%\ of\ Mg \div 24\frac{g}{mol})} = 16.7\ at.\%$$

Equation 8: Calculation for converting the wt. % of MgH_2 within the sample to at. %.

$$55\ mg * 17.8\ wt.\%\ MgH_2 = 9.79\ mg\ of\ MgH_2$$

Equation 9: Calculation for converting the weight of h-Mg nanoparticles loaded into the furnace for the TPD measurement to weight of MgH_2.

$$\frac{9.79\ mg * 7.6\ wt.\%\ H_2\ in\ MgH_2}{2\frac{g}{mol}} = 0.372\ mmol\ of\ H_2$$

Equation 10: Calculation for converting the weight of MgH_2 to mmol of H_2 within h-Mg.

$$\frac{7.9\ cm^3\ of\ H_2 * 0.08988\frac{g}{L}\ H_2\ density}{2\frac{g}{mol}} = 0.355\ mmol\ of\ H_2$$

Equation 11: Calculation of the experimental data for volume of H_2 analyzed by the RGA to mmol of H_2.

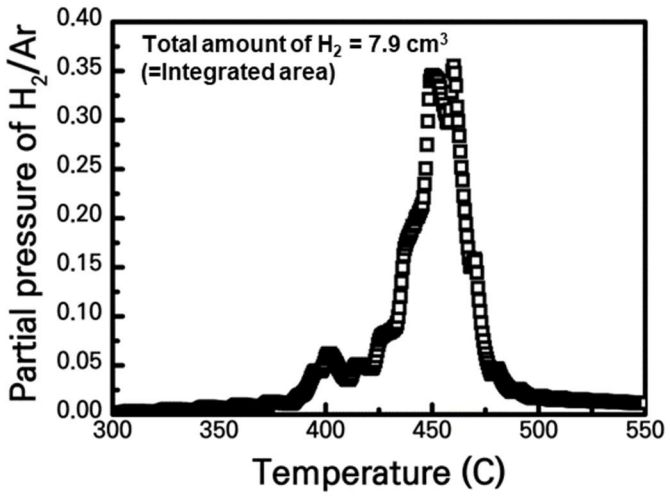


Figure 18: TPD of 55 mg h-Mg nanoparticles with a heating rate of 10 ^{o}C min^{-1}. The integrated area underneath the curve yielded the volume of H_2 gas. Reprinted with permission from [2]. Copyright (2023) American Chemical Society.

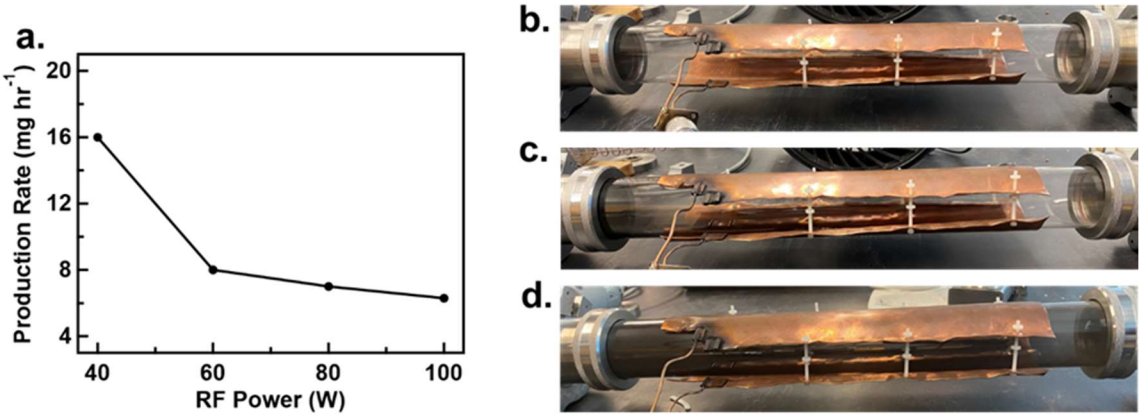


Figure 19: (a) Production rates of h-Mg nanoparticles with RF power varied from 40 W to 100 W. (b) A photograph of the plasma reactor before synthesis. Photographs of the plasma reactor after synthesis at (c) 80 W and (d) 100 W of RF power. Reprinted with permission from [x]. Copyright (2023) American Chemical Society.

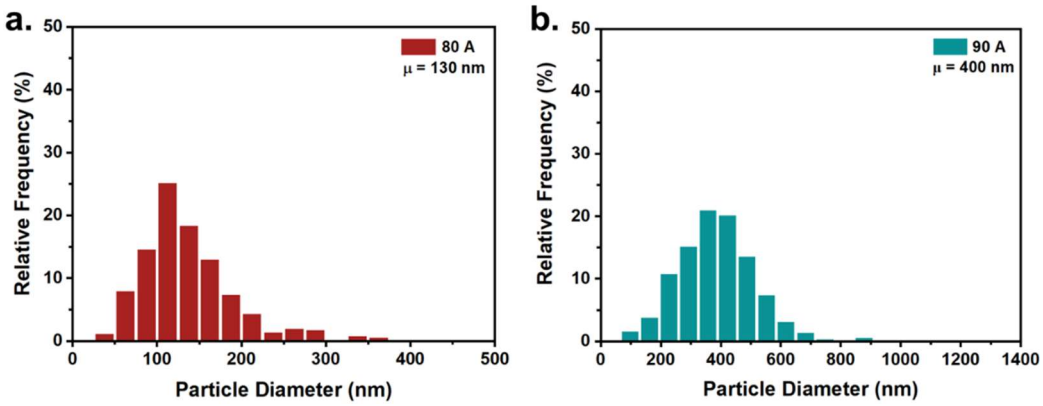


Figure 20: Particle size distributions of h-Mg nanoparticles synthesized using (a) 80 A and (b) 90 A of current. Reprinted with permission from [2]. Copyright (2023) American Chemical Society.

TEM was used to analyze the morphology and size of the Mg and h-Mg nanoparticles. The size distributions of h-Mg and Mg nanoparticles with their respective TEM images are shown in **Figure 21a–c and 21d–20f**, respectively. Both samples exhibit hexagonal crystal morphology commonly found in crystalline Mg nanoparticles, which is

the thermodynamically most favorable structure for Mg.[249] Mg and h-Mg samples have similar average sizes (~150 nm), but the size distributions are dissimilar. Interestingly, the Mg nanoparticles have wider size distributions than h-Mg nanoparticles, signifying that exposure to the hydrogen plasma results in focusing the nanoparticles to narrower size distributions. Similar observations were found for plasma-treating bismuth particles in-flight, in which the particle size distribution narrowed after plasma exposure.[297] There are noticeably fewer nanoparticles below 50 nm upon hydrogen treatment, possibly due to their evaporation within the plasma. Mg nanoparticles of 40 nm have shown an evaporation temperature of about 800 K,[71] which particle temperatures in the plasma can reach 800 K when operating at 80 W of RF power, as discussed later in the manuscript.

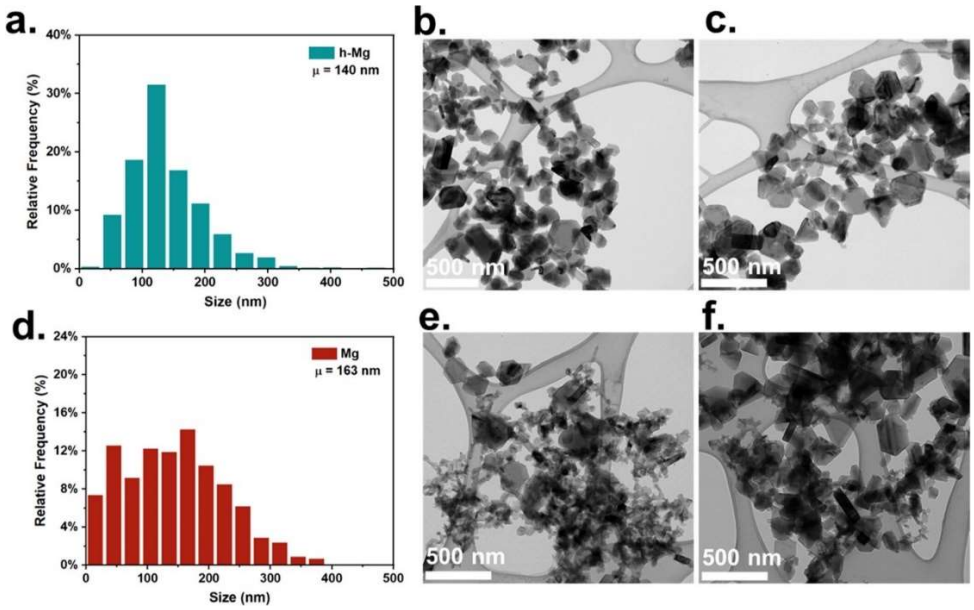


Figure 21: (a) Size distribution of 1000 h of Mg NPs from TEM. (b, c) TEM images representative of the size distribution of h-Mg NPs. (d) Size distribution of 1000 Mg NPs from TEM. (e, f) TEM images representative of the size distribution of Mg NPs. Reprinted with permission from [2]. Copyright (2023) American Chemical Society.

HR-TEM was used to gain insight into MgH_2 growth on the Mg nanoparticles when exposed to a hydrogen plasma. Particles of various sizes were analyzed, showing the presence of MgH_2 at different areas on the Mg crystals according to size. The TEM images of h-Mg crystals with particle sizes of 50–300 nm are shown along with their respective FFT diffraction patterns in **Figure 22a–c**. For ~300 nm particles, the surface consists of an ~45 nm thick MgH_2 layer, whereas the bulk shows only Mg. For particle sizes of ~100 nm, both the surface and bulk of the Mg crystals contain MgH_2. Particles of ~50 nm also have MgH_2 within the bulk, but parts of the crystal lack hydrogenation. Nonthermal plasmas are notorious for generating reactive gas species due to electron collisions, whereby the precursor radicals would react with the surface of nanoparticles or thin films. In the case of hydrogenation, atomic hydrogen generated by the low-temperature plasma using a H_2 gas precursor can react with the Mg nanoparticles aerodynamically carried through the plasma reactor. The atomic H diffuses into the Mg particle to react and nucleate MgH_2, forming crystalline domains and creating a hydride outer layer. Remarkably, MgH_2 is prevalent throughout the entire crystal for 100 nm particles, suggesting that smaller nanoparticles are easier to hydrogenate than larger ones. Previous work has found that the uptake of hydrogen into bulk Mg is a diffusion-controlled process through MgH_2 at the surface. The diffusion coefficient (D) of hydrogen into Mg is 10^{-13} m^2 s^{-1} at 300 K compared to 10^{-17}–10^{-20} m^2 s^{-1} through MgH_2.[277, 298] Therefore, hydrogen diffusion is considerably slower through MgH_2 than Mg. Using the residence time of the particles in the plasma (~185 ms) and Fick's diffusion law, we estimate the hydrogen diffusion length in Mg to be ~105 nm. This value is consistent with the thickness of the MgH_2 layer in the

larger particles (~45 nm). The apparent difference between the estimated diffusion length and the actual thickness of the MgH_2 layer is likely due to the decrease in diffusivity once the MgH_2 lattice is formed. The fact that the MgH_2 formation is diffusion-limited is also consistent with the results shown in **Figure 17e**, with smaller nanoparticles having a higher fraction of MgH_2 compared to larger ones. Overall, the combination of XRD, SEM, and HR-TEM results suggests that particle size must be minimized to achieve a high degree of hydrogenation. On the other hand, other effects, such as nanoparticle heating and hydrogen desorption, play a role in the plasma-induced hydrogenation process. These effects are described in greater detail in **Section 4.4**.

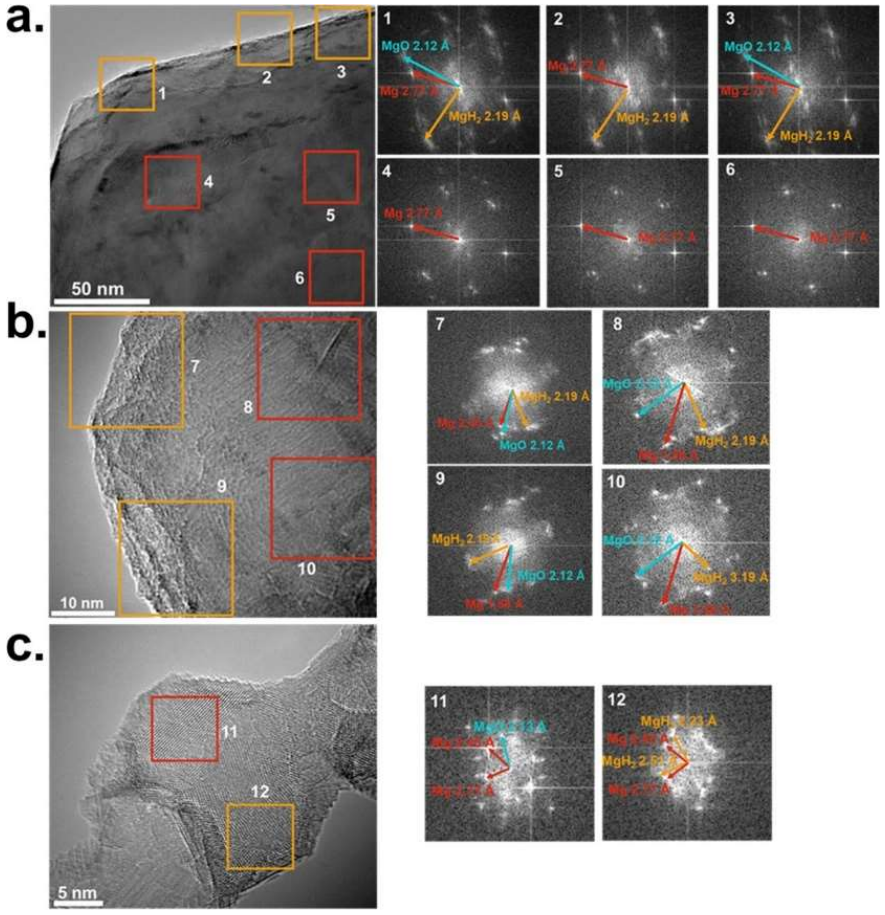


Figure 22: HR-TEM of (a) a 300 nm particle, (b) a 100 nm particle, and (c) a 30 nm particle, along with their respective FFT diffraction patterns. Blue arrows indicate the MgO lattice plane; yellow arrows indicate the MgH_2 lattice plane; and red arrows indicate the Mg lattice plane. Reprinted with permission from [2]. Copyright (2023) American Chemical Society.

The concepts described in the previous paragraph were applied to the plasma system in order to further maximize the MgH_2 content formed by this process. **Figure 23a** shows the change in XRD patterns from samples synthesized at different flow rate conditions. It is important to note that the partial pressure of the composition gas was kept constant in order to rule out factors from evolved gas composition. The original flow rates of Ar and H_2 that were used to produce the 23 wt. % MgH_2 sample were 350 sccm and 30 sccm, respectively. For the 32 wt. % MgH_2 sample, the flow rates of Ar and H_2 were 300 sccm and 25.7 sccm, respectively. Lastly, the flow rates of Ar and H_2 that produced 45 wt. % MgH_2 were 250 sccm and 21.4 sccm. All three of these conditions led to a partial pressure of 0.237 torr. The results indicate that reducing the total flow rate of the gases while keeping the partial pressure of H_2 and total pressure constant in the plasma reactor results in more MgH_2 incorporated within the Mg nanopowder. Reducing the total gas flow within the plasma reactor leads to longer residence times of the Mg particles exposed to the hydrogen plasma. Since the diffusion of atomic hydrogen is sluggish according to Fick's law of diffusion, longer residence times would be helpful to allow the diffusion of atoms across the MgH_2 barrier. To summarize, up to 45 wt. % of MgH_2 can be produced from increasing residence time by reducing the overall flow rate of the gases.

Recall that we observed that smaller nanoparticle sizes lead to more MgH_2 incorporated within the Mg crystals due to the shortened diffusion lengths across the particle. Less time is needed for atomic hydrogen to diffuse across the MgH_2 layer that forms on the surface because it is thinner overall in a smaller particle. **Figure 23b** shows the MgH_2 wt. % when reducing the particle size as well as reducing the overall flow rate

of the gases while maintaining a partial pressure of 0.237 torr. A drastic increase of MgH_2 was produced in the Mg plasma treated powder to 70 wt. % due to the shortened diffusion length across the nanoparticles and longer residence time of Mg exposure to the plasma.

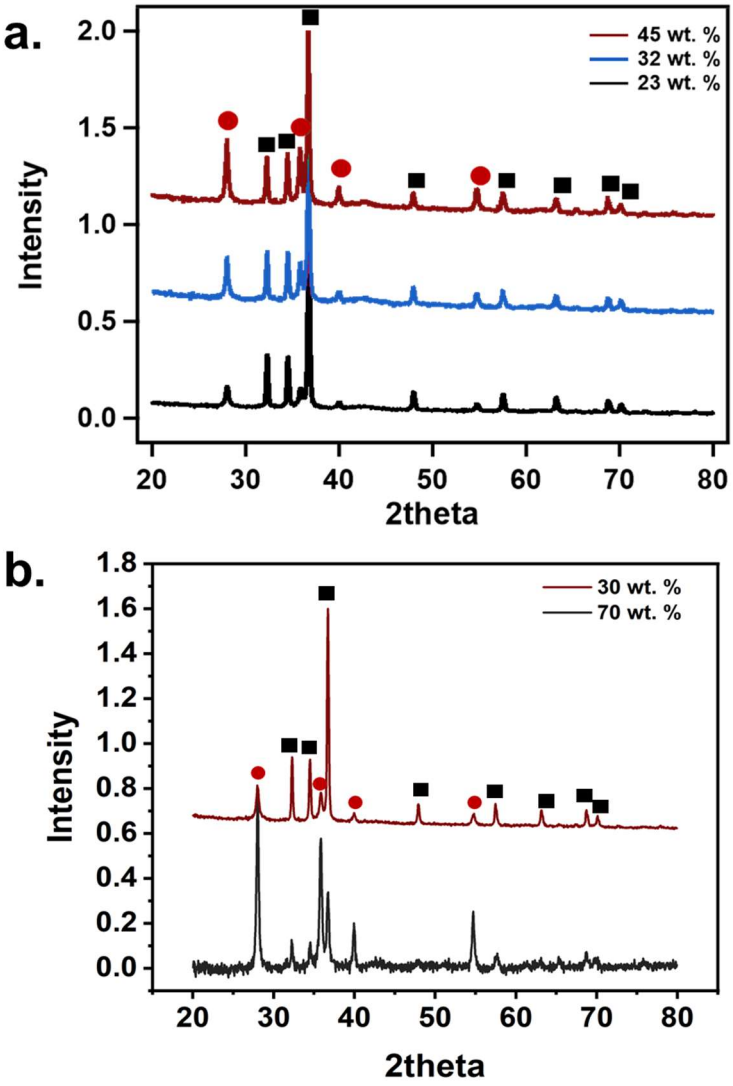


Figure 23: (a) h-Mg nanoparticles synthesized with decreasing total flow rate of gases while maintaining a constant partial pressure of H_2 (0.237 torr). (b) h-Mg nanoparticles synthesized by decreasing the particle size of the Mg crystallites as well as reducing the total flow rate of gases and keeping a constant partial pressure. The red circles indicate the MgH_2 planes of the tetragonal crystal lattice while the black squares indicate the Mg phases of the hexagonal crystal lattice.

4.4: Plasma Characterization

OES was used to characterize the plasma chemistry. **Figure 24a** shows the measured OES spectra at 80 W of RF power. As expected, the emission spectrum is rich with many lines. Emission lines from atomic metals H and Ar are clearly observable. The emission line assignment is based on the broadly utilized NIST atomic spectra database.[299] The Mg emission at 570.4 nm is the most prominent signal from the plasma, followed by the Ar line at 763.51 nm and the H_α line at 656.279 nm. We should note that the Mg emission at 570.4 nm is the second-order emission from the 285.2 nm line corresponding to the $3s3p–3s^2$ transition of neutral Mg. As shown in **Figures 25a-c**, the Mg, Ar, and H emission lines become more intense with increasing RF power, as expected, since the plasma density increases with power. Actinometry is used to estimate the density of atomic hydrogen within the plasma. To that end, we have used the intensity ratio between the H 656 nm and Ar 763 nm lines, coupled with a reasonable estimate of the electron-induced excitation rates as obtained by a commonly utilized Boltzmann solver, Bolsig+.[300] By utilizing the intensity ratio of emission lines obtained from our optical emission spectroscopy (OES) measurements, a relationship summarized by Tatarova et al. is used to derive the atomic hydrogen density (**Equation 12**):[301]

$$\frac{n_H}{n_{Ar}} = \frac{I(656)}{I(763)} \times \frac{656}{763} \left(\frac{X_{Ar}}{X_H}\right) \times \frac{A_{750}/\left(\sum A_{j,Ar} + K_M^{Ar} \times n_M\right)}{A_{656}/\sum A_{j,H}}$$

Equation 12: The relationship between the atomic densities of the gas species to the intensities of the light emission from the atoms, excitation rates, and transition probabilities for optically allowed transitions from excited states of the atoms.

where n_H and n_{Ar} are the densities of atomic hydrogen and argon, respectively. n_{Ar} was obtained by the ideal gas law. The emission intensities $I(656)$ and $I(763)$ represent the respective atomic species of hydrogen and argon at those specific wavelengths. The following emission lines were used to derive the atomic hydrogen density: Ar line at 763.5 nm (transition 4p to 4s) and H line at 656.2 nm (transition from $3d^2D$ to $2P^2P_0$). A_{656} and A_{750} are the transition probabilities for the corresponding lines. $A_{j,Ar}$ and $A_{j,H}$ are the transition probabilities for all other optically allowed transitions from the same excited states for the corresponding atomic species. It is necessary to achieve the accurate branching ratio. The transition probabilities used in this analysis are sourced from the NIST atomic spectra database.[299] K_M^{Ar} is quenching rate that takes into consideration the nonradiative relaxation of the excited state for Ar. The variable n_M is the density of the collision partner, which is determined using the ideal gas law. (M=Ar and H_2) For the specific numerical values in this relation, we refer the reader to our previous report.[302] X_{Ar} and X_H represent the rates of excitation by electron impact to the selected states of Ar and H. These rates were obtained through BOLSIG+ calculation, a commonly used software for the solution of the Boltzmann transport equation.[303] The collision cross-section for Ar, H, and H_2 are acquired from the LXCat database.[304-306] Despite the dependence of excitation rates on the electron temperature, the derived atomic hydrogen density as function of plasma power shows almost same trend according to the electron temperature since emission line intensities are strongly influenced by the plasma power. Uner et al. actually measured electron temperature through quite similar plasma reactor with our reactor, and it was 4 ± 1.5 eV.[297] Therefore, based on our previous estimation for electron

temperature and reactor geometry that used in this study, we assumed that the electron temperature is 5 eV.[33] The atomic hydrogen density values obtained using this approach are shown in **Figure 24b**. As expected, the level steadily increases with the RF power. The atomic hydrogen density is considerable, exceeding 10^{14} cm^{-3}, as it is typically observed in these moderately low-pressure processes. This supports our hypothesis that atomic hydrogen plays a crucial role in the fast hydrogenation of Mg nanoparticles as they travel through the plasma. The conversion of molecular H_2 to atomic H is a well-known process within low-temperature plasmas. There are several pathways through which atomic H is generated. Electron impact with rovibrationally excited H_2 molecules can exceed the energy threshold to break apart the H_2 bonds. The same process can occur for electronically excited H_2 bonds.[307-309] Atomic hydrogen can then readily diffuse into the Mg lattice through the interstitial sites of the hexagonal lattice.[310]

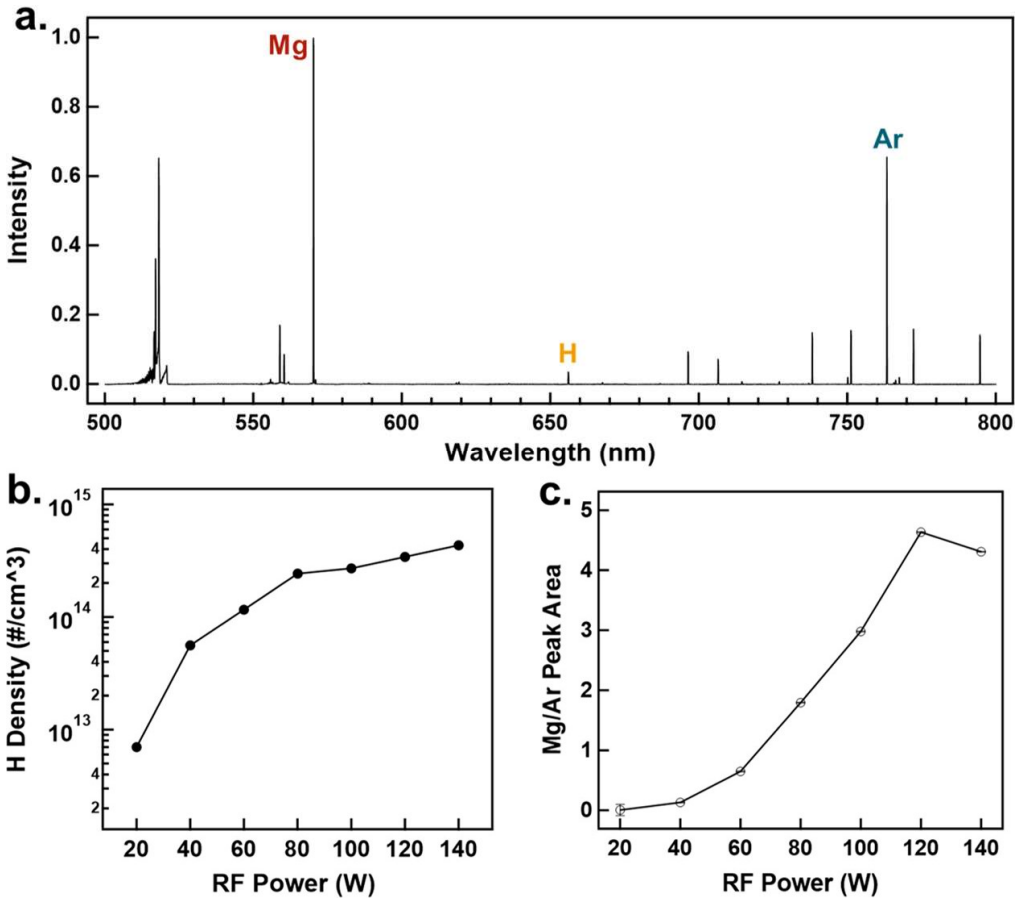


Figure 24: (a) OES spectra of the plasma. (b) Actinometry was used to obtain the atomic H density according to the RF power. The integrated area ratio of the Mg 570 nm and Ar 763 nm lines were obtained from the OES spectra to gain insight into the atomic Mg density at different plasma powers (c). Reprinted with permission from [2]. Copyright (2023) American Chemical Society.

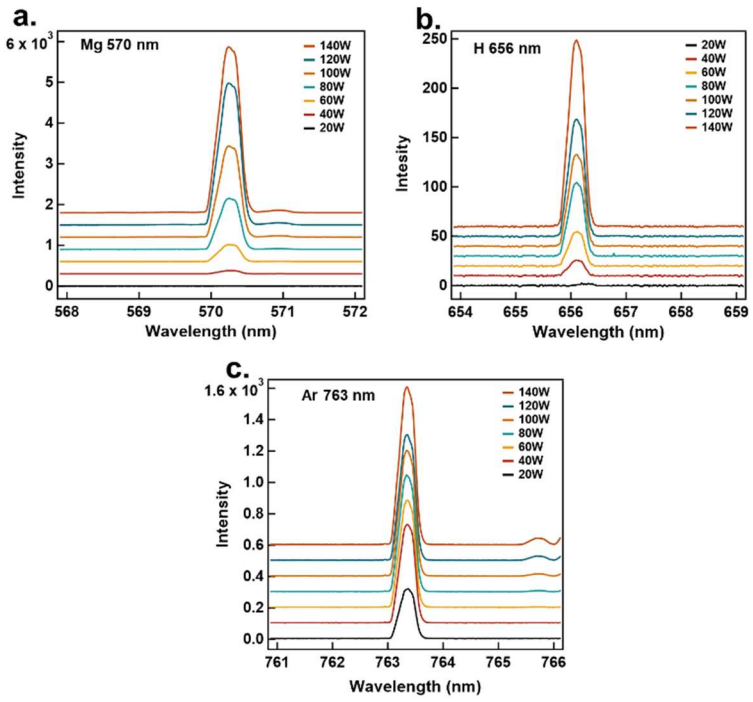


Figure 25: OES measurements showing the emission lines of (a) Mg 570 nm, (b) H 656 nm, and (c) Ar 763 nm. Reprinted with permission from [2]. Copyright (2023) American Chemical Society.

We also note that the Mg atomic line at 570 nm is very intense. While it is possible to estimate the density of atomic magnesium using actinometry, similarly for hydrogen, there are no reported cross-sections for the electron-impact-induced excitation of Mg atoms. Nevertheless, **Figure 24c** shows the ratio between the Mg 570 nm and the Ar 763 nm peak areas with varying RF power, which is strongly dependent on power. As mentioned earlier in the manuscript, the yield of Mg nanoparticles decreases significantly with power (**Figure 19a**), and at higher power, we observe the rapid growth of a metallic film onto the reactor's inner walls. These observations, therefore, suggest that Mg nanoparticles can evaporate as they are exposed to the low-temperature plasma and do so more rapidly at higher RF input power. Ion bombardment could potentially sputter Mg

from condensed particles in the plasma; however, the sputtering yield is high only when ions are accelerated to the target material surface with hundreds of volts of energy, whereas the floating potential of nanoparticles in low-temperature plasmas is only a few volts.[311, 312] Thermal evaporation and gas-condensation of Mg particles within the plasma is a more likely explanation for the presence of atomically charged Mg in the reactor. Condensed particles can experience intense heating through surface reactions in low-temperature plasmas, which we have found can heat the Mg particles to their evaporation temperature.[313-315]

Further insights are obtained by solving a particle energy balance (**Equation 13**) and estimating the particle temperatures at various RF powers, using the approach described by Mangolini et al.[316] In this approach, a steady-state particle temperature is calculated by balancing the heat generation terms, induced by reactions between the particle and plasma-produced species and the cooling to the background gas. The nanoparticle heating (G) and cooling (L) terms are calculated by **Equation 14 and 15**, respectively. Electron–ion recombination and hydrogen recombination at the particle surface account for particle heating, whereas thermal conduction to the background gas causes particle cooling. Electron–ion recombination events at the nanoparticle surface generate heat with an energy release equal to the ionization energy of Ar (15.76 eV) for each impinging ion.[38] The ion density was measured for a similar system to be 10^{11} to 10^{12} cm^{-3} according to the input RF power.[297] For our calculations of electron–ion recombination heat generation, we assumed the ion density to be 10^{11} cm^{-3}. Chemical reactions involving hydrogen at the particle surface also release heat and increase the

particle temperature. Among them, atomic hydrogen recombination at the surface releases the most heat with an energy of 4.5 eV per atomic hydrogen pair.[314] **Figure 26** shows the particle temperature computed from the energy balance using the measured H densities (**Figure 24b**) at various RF powers. While the gas temperature in low-temperature plasmas remains low and close to room temperature, some gas heating does indeed occur. Therefore, we computed the nanoparticle temperature for background gas temperatures of 300 and 400 K. A reasonable electron temperature of 5 eV was used for these calculations. The model suggests that particle temperatures can exceed 1000 K at a high RF power, exceeding not only the Mg evaporation temperature but the hydrogen desorption temperature as well (**Figure 18**).[317-319] This indicates that there may be excessive particle heating within the plasma at an RF power above 60 W, hindering MgH_2 production due to H_2 desorption from the particles. Excessive particle heating is a likely explanation for the plateauing in the MgH_2 fraction observed from XRD when increasing the RF power (**Figure 17b**).

$$G_{e^- - ion\ recombiniation} + G_{H_2\ recombination} = L$$

Equation 13: Particle energy balance equation using the hydrogen recombination and electron-ion recombination reactions as the heating terms. The cooling term is thermal conduction to the background gas.

$$G = (\frac{1}{4} n_H S \sqrt{\frac{8k_B T_{gas}}{\pi m_H}} \times \frac{E_{H_2\ recombination}}{2}) + (\frac{1}{4} n_{ion} S \sqrt{\frac{8k_B T_{e^-}}{\pi m_{Ar}}} \times E_{Ar\ ionization})$$

Equation 14: The additive particle heating term calculations. The hydrogen density (n_H), surface area (S), gas temperature (T_{gas}), Boltzmann constant (k_B), hydrogen mass (m_H), electron temperature (T_{e^-}), and argon mass (m_{Ar}) are used in these equations.

$$L = \frac{1}{4} n_{gas} S \sqrt{\frac{8 k_B T_{gas}}{\pi m_{gas}}} \times \frac{3}{2} k_B (T_p - T_{gas})$$

Equation 15: The cooling term calculation that the heating terms are balanced in order to find the particle temperature (T_p) by isolating it.

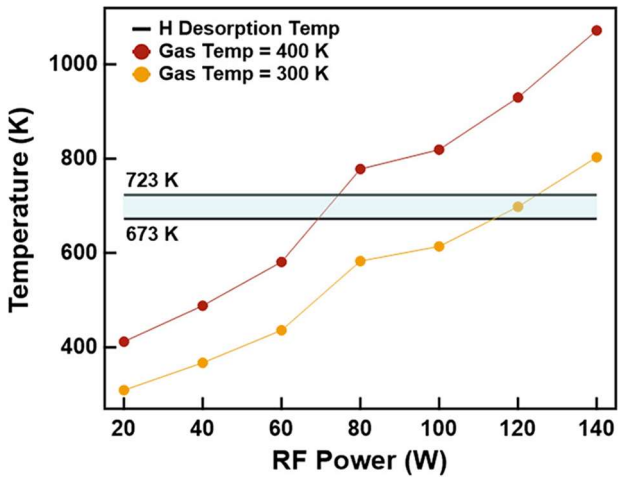


Figure 26: Graph of nanoparticle temperature based on the particle energy balance approach when assuming an electron temperature of 5 eV and two gas temperatures of 300 and 400 K. The area in blue is the range of H_2 desorption temperatures as obtained by TPD. Reprinted with permission from [2]. Copyright (2023) American Chemical Society.

4.5: Energetic Performance

The reaction species of the samples during ignition were characterized using T-jump/TOFMS in an Ar environment. $KClO_4$ was used as the oxidizer because it releases oxygen at a low temperature ($KClO_4 \sim 580$ °C).[71] The ignition mechanism can be investigated by comparing the ignition temperature and time from the sample/oxidizer mixtures to the O_2 release temperatures of the oxidizer. If O_2 releases after ignition, then the relevant reaction mechanism occurs in the solid state instead of a gas-phase reaction when O_2 releases beforehand. The T-jump/TOFMS results of h-Mg and Mg are shown in

Figure 27a, displaying similar spectra, except H_2 is detected for h-Mg nanoparticles. Samples were combusted with the $KClO_4$ oxidizer in the T-jump/TOFMS instrument to determine the Mg release profile according to the temperature and time (**Figure 27b**). Mg releases earlier from h-Mg nanoparticles when reacting with $KClO_4$ compared with Mg nanoparticles. T-jump measurements showed that the ignition temperatures for h-Mg/$KClO_4$ and Mg/$KClO_4$ mixtures were ~480 and ~690 °C, respectively. A high-speed camera was used to record optical emission during ignition to help obtain ignition temperatures of the thermite mixtures, as shown in the time-stamped images in **Figure 27c**. These results indicate that the incorporation of H_2 in the Mg nanoparticles results in lower ignition thresholds with a drastically reduced ignition temperature by over 200 °C when reacting with $KClO_4$. The H_2 in h-Mg nanoparticles facilitates the release of Mg at a lower temperature, making the fuel accessible at a lower temperature and leading to faster ignition.

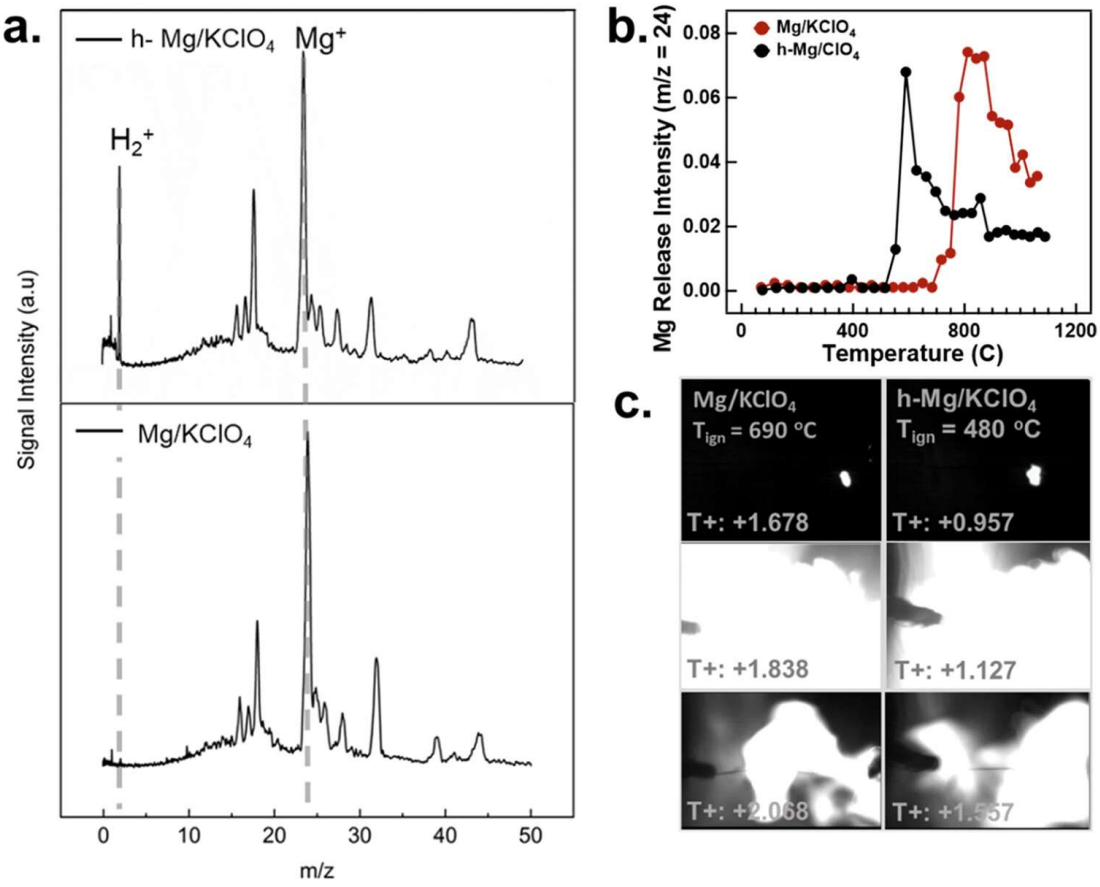


Figure 27: (a) Mass spectrometry spectra of h-Mg and Mg NPs and (b) Mg release profiles from T-jump/TOFMS for h-Mg/$KClO_4$ and Mg/$KClO_4$. (c) High-speed camera images of ignited Mg/$KClO_4$ and h-Mg/$KClO_4$ thermite mixtures. Reprinted with permission from [2]. Copyright (2023) American Chemical Society.

Figure 28 shows the H_2, O_2, and Mg release intensities from the T-jump/TOFMS measurements during the ignition of the nanothermite mixtures. The O_2 release temperature significantly reduces from ~680 to ~500 °C for h-Mg. For Mg nanoparticles, and ignition occurs slightly after O_2 is released. This result indicates that the mechanism for Mg with $KClO_4$ is controlled by the decomposition of the oxidizer to release gas-phase O_2. In contrast, the ignition mechanism changes with the addition of MgH_2. Ignition occurs after the desorption of H_2 but before the release of O_2 from $KClO_4$. This implies that the presence of H_2 and its desorption from MgH_2 controls ignition. Interestingly, the decomposition of $KClO_4$ occurs after ignition begins, indicating that a condensed-phase reaction mechanism may take place between MgH_2 and $KClO_4$. Early H_2 gas generation may have a significant effect on ignition with $KClO_4$ because H_2 can react with O_2 from the oxidizer, effectively releasing supplemental heat to initiate the release of Mg vapor earlier for accelerated combustion. **Equation 16 and 17** show the enthalpies of the MgH_2 and Mg reactions with $KClO_4$.

$$4Mg + KClO_4 \rightarrow 4MgO + KCl \qquad \Delta H_r = -10.2 \text{ kJ g}^{-1}$$

Equation 16: The gravimetric oxidation enthalpy of Mg reaction with $KClO_4$ oxidizer.

$$2MgH_2 + KClO_4 \rightarrow 2MgO + 2H_2O + KCl \qquad \Delta H_r = -7.15 \text{ kJ g}^{-1}$$

Equation 17: The gravimetric oxidation enthalpy of MgH_2 reaction with $KClO_4$ oxidizer.

The gravimetric reaction enthalpy of MgH_2 with $KClO_4$ is lower than Mg; however, T-jump/TOFMS indicates that the reaction kinetics are faster since H_2 reacts with the

oxidizer and initiates Mg release. Another possibility for the greater reactivity of MgH_2 compared to Mg may be related to changes in the surface chemistry. H_2 desorption from the particle outer layer likely exposes reactive Mg sites, providing a pathway for oxygen to interact with and accelerate combustion. In general, we can conclude that MgH_2, which does not increase the energy density based on thermodynamic arguments, offers a pathway to reduce the ignition threshold and acceleration of the overall kinetics.

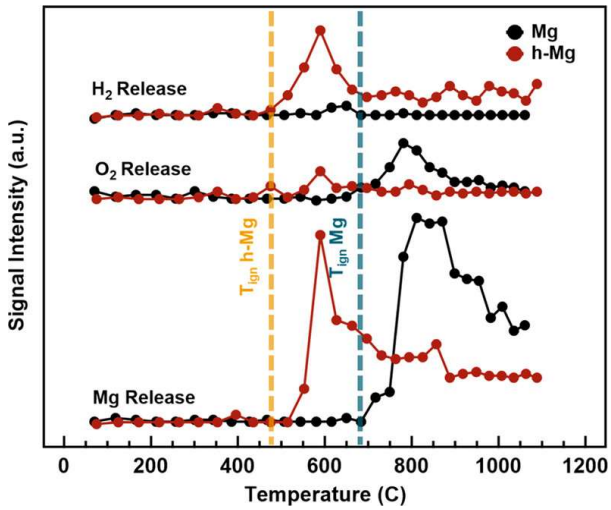


Figure 28: Hydrogen, oxygen, and magnesium release profiles from T-jump/TOFMS for h-Mg and Mg NPs during ignition with $KClO_4$. The yellow dashed line indicates the ignition temperature of h-Mg NPs, while the blue dashed line denotes the ignition temperature of Mg NPs. Reprinted with permission from [2]. Copyright (2023) American Chemical Society.

Pressure cell tests were performed in order to verify the impact of hydrogen gas generation during combustion of Mg nanoparticles. $KClO_4$ was used as the oxidizer in these tests. **Figure 29a-c** shows the peak pressure, pressurization rate, and burn time of Mg nanoparticles, 8 wt.% MgH_2 nanoparticles, and 25 wt. % MgH_2 nanoparticles. For both samples containing MgH_2, the peak pressure released during combustion with $KClO_4$

increased substantially. About double the peak pressure was seen from the composite sample containing 25 wt. % MgH_2. The 8 wt. % MgH_2 sample released almost 1.5 times that of the untreated Mg nanoparticles. Likewise, the pressurization rate of both the MgH_2-containing nanoparticles increased drastically, with over 4 times the rate of the untreated Mg. Interestingly, even little hydrogen content (8 wt. % MgH_2) seems to have a significant impact on the rate that pressure is released from the nanoparticles. The results indicate that incorporating hydrogen within Mg nanoparticles has a large impact on the energy release, especially with $KClO_4$ as the oxidizer. Water vapor forms if the hydrogen reacts with the oxidizer, which can add to the pressure release. The burn time seems to decrease with the hydrogen treated Mg samples, and more MgH_2 content has a larger impact on the burn time. This finding could be due to the supplemental exothermic reaction that occurs between hydrogen and oxygen from the oxidizer. Additionally, if a condensed-phase reaction does indeed occur between the oxidizer and hydrogen from MgH_2, as evidenced by ignition taking place immediately after hydrogen desorbs, then the energy release and burning rate would be significantly impacted from the faster reaction kinetics associated at the condensed-phase. Overall, the results show that hydrogen at the surface of Mg benefits ignition in both hastening reaction kinetics to initiate ignition, but also by generating substantially more pressure in a fast rate during combustion.

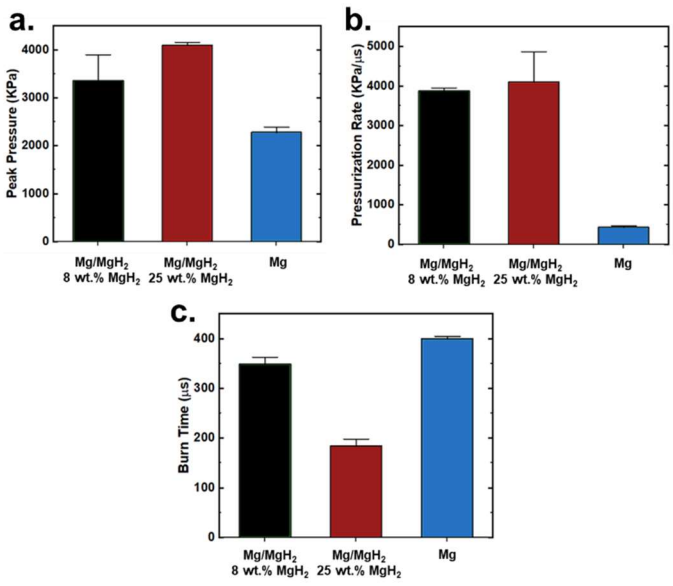


Figure 29: Pressure-cell tests of 8 wt. %, 25 wt. % MgH_2/Mg composites, and untreated Mg nanoparticles. The results indicate that hydrogen incorporation significantly impacts the (a) peak pressure, (b) pressurization rate, and (c) burn time of Mg.

4.6: Summary

Low-temperature plasmas can process Mg nanoparticles in-flight with hydrogen to give nanomaterials with a significant fraction of MgH_2. Careful TEM characterization shows that larger particles (~300 nm) have a hydrogen-rich "crust" with MgH_2 domains in the outer shells of the particles. Smaller particles (~50 nm) appear to be hydrogenated throughout the volume. This is consistent with an inward hydrogen diffusion process where the plasma provides an effective source of atomic hydrogen that can readily dissolve into the Mg lattice. The in-flight plasma treatment has profound effects on the combustion kinetics. The ignition temperature with the $KClO_4$ oxidizer is lowered significantly upon hydrogenation, from ~690 to ~480 °C. The lower ignition temperature correlates well with the desorption of H_2 from MgH_2 in the 400–500 °C range, suggesting that the released

hydrogen is responsible for effectively jump-starting the combustion. The earlier onset of the exothermic reaction, in turn, results in the earlier release of Mg vapor, as observed by T-jump/TOFMS measurements, further enhancing the combustion of the Mg fuel. Pressure cell tests indicate that the energy release and burning rate are drastically higher with hydrogen-treated Mg compared to untreated Mg. We have also performed careful characterization of the plasma process by optical emission spectroscopy. This confirms that the plasma is effective at dissociating molecular hydrogen and driving the in-flight hydrogenation of the Mg particles. On the other hand, the nanoparticle energy balance shows that the particle temperature can be sufficiently high not only to desorb hydrogen but also to initiate the evaporation of Mg. This is consistent with the fraction of MgH_2 reaching a plateau and with the loss of Mg to the reactor walls as a film at high plasma input powers. These findings indicate that excessive plasma power is harmful for hydrogen plasma treatment of Mg particles, providing guidance toward further process optimization. Overall, this work demonstrates that a rapid, in-flight, nonthermal plasma processing step can have significant effects on the combustion of Mg-based energetic nanoparticles, thus providing an additional lever to tune their energy release profile.

Final Conclusions:

The work discussed in this dissertation focuses on the surface engineering of Mg nanoparticles via non-thermal plasma processing. This approach enables a single-step synthesis involving Mg particle nucleation/growth followed by simultaneous surface functionalization within the gas phase. The main contents are comprised of two parts: a silicon coating applied to the surface of Mg in-flight outlined in **Section 3**, and the plasma treatment of airborne Mg with hydrogen. Both works are novel regarding the use of a low-temperature plasma for functionalizing the surface of individual nanoparticles suspended in an aerosol before exposure to ambient conditions that allow an oxide layer to form. As discussed in the preceding sections, little work has previously been conducted to functionalize the surface of metal nanoparticles by plasmas for energetic applications due to the degree of difficulty in achieving conformal coatings on the surface of discrete particles. The topic of energetics as a whole, focuses on engineering nanomaterials to relieve the disadvantages arising from the native oxide layer that inherently forms onto the surface of metals. Therefore, plasma treating nanomaterials to attain nanostructured surfaces while increasing their chemical reactivity in specific environments and conditions is pertinent for ignition applications.

Section 3 explored the ignition effects of applying a partially oxidized Si coating via a silane plasma discharge onto aerosolized Mg nanoparticles. A core-shell nanostructure was achieved by this process, which involved Mg-Si bonds at the interface while the outermost layer of the nanoparticles is composed mainly of silicon oxides. This surface structure essentially corresponds to a nanothermite interface ideal for energetics

because of the high heat release associated with thermite reactions. The nanothermite surface was exploited for ignition of the Mg core with another oxidizer, Bi_2O_3. Two reactions take place according to this heterostructure: an exothermic intermetallic reaction between the Mg core and Si shell at the particle interface, which release heat and expedites the heating of the particle, and a redox reaction between the silica outer layer and the Mg core, which accelerates the release of Mg in the vapor phase to react with the oxidizer. In-situ TEM was performed to visualize the accelerated release of Mg from the particle core. It was found that the particles containing the partially oxidized Si coating started to release the Mg from the core earlier. Despite the Mg vaporizing and diffusing out of the core at a lower temperature, hollowing of the Mg core was slow and prolonged. Yet, ignition is dramatically accelerated according to Tjump/TOFMS. This indicates that an earlier—albeit slower and more sustained—release of the Mg from the core has a large impact on the ignition threshold and ignition kinetics of Mg.

Section 4 focused on how hydrogen plasma treatment of Mg nanoparticles was achieved, and described how the processing parameters that maximize MgH_2 formation were investigated. The results indicated that balancing the plasma power and partial pressure of hydrogen are important to hydrogenating Mg. High enough power is necessary in order to create atomic hydrogen; however, excessive power consequently heats Mg particles to temperatures that surpasses the hydrogen desorption temperature of MgH_2. Excessive partial pressure of hydrogen lowers the power distribution of the plasma due to losses of energy from rotovibrational excitation of hydrogen. Reducing particle size and increasing residence time are the major factors that significantly impact the hydrogenation

of Mg. A diffusion rate across into Mg as well as across a MgH_2 layer that thickens over time exists. A smaller distance for hydrogen to travel (smaller size of Mg particles) as well as longer time for hydrogen to allow hydrogen to travel according to its diffusion rate will enable more MgH_2 nucleation from the Mg nanoparticles. The ignition tests suggest that the presence of hydrogen at the Mg surface increases the reactivity of the nanoparticles. More pressure is generated at a fast rate because hydrogen gas is generated upon heating of the particles. Additionally, hydrogen reacts with the oxidizer exothermically, releasing supplemental heat to liberate Mg from particle cores at a faster rate. Instantly after hydrogen desorbs from Mg, ignition occurs and then Mg is vaporized and released to react with the oxidizer.

In conclusion, low-temperature plasma processing is a versatile method to creating core-shell nanostructures and functionalized surfaces. The two cases in this dissertation highlight the potential of non-thermal plasmas to tune the reactivity at the interface of nanoparticles, which affect the macroscale properties of the nanomaterial. It is important to emphasize that non-thermal plasmas hold value for nanostructuring materials for energetic applications. Since the surface reactivity of materials is critical for ignition, coating or treating energetic materials to enhance their surface properties is necessary. The work outlined in this dissertation highlights that low-temperature plasmas is a highly valuable method for manipulating the interfaces of nanomaterials to improve their surface reactivity for energetics.

Bibliography:

(1) Wagner, B.; Ghildiyal, P.; Biswas, P.; Chowdhury, M.; Zachariah, M. R.; Mangolini, L. In-Flight Synthesis of Core–Shell Mg/Si–SiO Particles with Greatly Reduced Ignition Temperature. *Advanced Functional Materials* **2023**, *33* (21), 2212805. DOI: https://doi.org/10.1002/adfm.202212805 (acccessed 2024/08/25).

(2) Wagner, B.; Kim, M.; Chowdhury, M.; Vidales Pasos, E.; Hizon, K.; Ghildiyal, P.; Zachariah, M. R.; Mangolini, L. Enhancing the Combustion of Magnesium Nanoparticles via Low-Temperature Plasma-Induced Hydrogenation. *ACS Applied Materials & Interfaces* **2023**, *15* (44), 51639-51649.

(3) Boulos, M. I.; Fauchais, P. L.; Pfender, E. Handbook of thermal plasmas. **2023**.

(4) Taylor, P. R.; Pirzada, S. A. Thermal plasma processing of materials: A review. *Advanced Performance Materials* **1994**, *1*, 35-50.

(5) Lieberman, M. *Principles of Plasma Discharges and Materials Processing*; John Wiley & Sons Inc, 1994.

(6) Boulos, M. I. Thermal plasma processing. *IEEE transactions on Plasma Science* **1991**, *19* (6), 1078-1089.

(7) Kortshagen, U. R.; Sankaran, R. M.; Pereira, R. N.; Girshick, S. L.; Wu, J. J.; Aydil, E. S. Nonthermal plasma synthesis of nanocrystals: fundamental principles, materials, and applications. *Chemical reviews* **2016**, *116* (18), 11061-11127.

(8) Hartgers, A. Modelling of a fluorescent lamp plasma. **2003**.

(9) Waymouth, J. F.; Bitter, F. Analysis of the plasma of fluorescent lamps. *Journal of Applied Physics* **1956**, *27* (2), 122-131.

(10) Trelles, J.; Chazelas, C.; Vardelle, A.; Heberlein, J. Arc plasma torch modeling. *Journal of thermal spray technology* **2009**, *18*, 728-752.

(11) Hopwood, J. Review of inductively coupled plasmas for plasma processing. *Plasma Sources Science and Technology* **1992**, *1* (2), 109.

(12) Gorla, C.; Liang, S.; Tompa, G.; Mayo, W.; Lu, Y. Silicon and germanium nanoparticle formation in an inductively coupled plasma reactor. *Journal of Vacuum Science & Technology A: Vacuum, Surfaces, and Films* **1997**, *15* (3), 860-864.

(13) Conrads, H.; Schmidt, M. Plasma generation and plasma sources. *Plasma sources science and technology* **2000**, *9* (4), 441.

(14) Zhilinsky, A. *Fundamentals of plasma physics*; John Wiley & Sons, 1980.

(15) Girshick, S. L.; Warthesen, S. J. Nanoparticles and plasmas. *Pure and applied chemistry* **2006**, *78* (6), 1109-1116.

(16) Mattox, D. M. *Handbook of physical vapor deposition (PVD) processing*; William Andrew, 2010.

(17) Ivchenko, I. N.; Loyalka, S. K.; Tompson Jr, R. *Analytical methods for problems of molecular transport*; Springer, 2007.

(18) Agarwal, P.; Girshick, S. L. Numerical modeling of an RF argon–silane plasma with dust particle nucleation and growth. *Plasma Chemistry and Plasma Processing* **2014**, *34*, 489-503.

(19) Mendoza Gonzalez, N. Y.; El Morsli, M.; Proulx, P. Production of nanoparticles in thermal plasmas: a model including evaporation, nucleation, condensation, and fractal aggregation. *Journal of thermal spray technology* **2008**, *17*, 533-550.

(20) Girshick, S. L. Particle nucleation and growth in thermal plasmas. *Plasma Sources Science and Technology* **1994**, *3* (3), 388.

(21) Mangolini, L. Monitoring non-thermal plasma processes for nanoparticle synthesis. *Journal of Physics D: Applied Physics* **2017**, *50* (37), 373003.

(22) Horanyi, M.; Goertz, C. Coagulation of dust particles in a plasma. *Astrophysical Journal, Part 1 (ISSN 0004-637X), vol. 361, Sept. 20, 1990, p. 155-161.* **1990**, *361*, 155-161.

(23) Ravi, L.; Girshick, S. L. Coagulation of nanoparticles in a plasma. *Physical Review E—Statistical, Nonlinear, and Soft Matter Physics* **2009**, *79* (2), 026408.

(24) Laroussi, M. Plasma medicine: a brief introduction. *Plasma* **2018**, *1* (1), 47-60.

(25) Mumtaz, S.; Khan, R.; Rana, J. N.; Javed, R.; Iqbal, M.; Choi, E. H.; Han, I. Review on the biomedical and environmental applications of nonthermal plasma. *Catalysts* **2023**, *13* (4), 685.

(26) Stoffels, E.; Kieft, I.; Sladek, R.; Van den Bedem, L.; Van der Laan, E.; Steinbuch, M. Plasma needle for in vivo medical treatment: recent developments and perspectives. *Plasma Sources Science and Technology* **2006**, *15* (4), S169.

(27) Ghimire, B.; Lee, G. J.; Mumtaz, S.; Choi, E. H. Scavenging effects of ascorbic acid and mannitol on hydroxyl radicals generated inside water by an atmospheric pressure plasma jet. *AIP Advances* **2018**, *8* (7).

(28) Jung, S.-N.; Oh, C.; Chang, J. W.; Liu, L.; Lim, M. A.; Jin, Y. L.; Piao, Y.; Kim, H. J.; Won, H.-R.; Lee, S. E. EGR1/GADD45α activation by ROS of non-thermal plasma mediates cell death in thyroid carcinoma. *Cancers* **2021**, *13* (2), 351.

(29) Liu, X.; Li, Y.; Wang, S.; Huangfu, L.; Zhang, M.; Xiang, Q. Synergistic antimicrobial activity of plasma-activated water and propylparaben: Mechanism and applications for fresh produce sanitation. *Lwt* **2021**, *146*, 111447.

(30) Lukes, P.; Clupek, M.; Babicky, V.; Sunka, P. Ultraviolet radiation from the pulsed corona discharge in water. *Plasma sources science and technology* **2008**, *17* (2), 024012.

(31) Snoeckx, R.; Bogaerts, A. Plasma technology–a novel solution for CO 2 conversion? *Chemical Society Reviews* **2017**, *46* (19), 5805-5863.

(32) Foote, A.; Dedrick, J.; O'Connell, D.; North, M.; Gans, T. Conversion of CO 2 to CO using radio-frequency atmospheric pressure plasmas. In *APS Annual Gaseous Electronics Meeting Abstracts*, 2016; p DT3. 005.

(33) Kim, M.; Biswas, S.; Nava, G.; Wong, B. M.; Mangolini, L. Reduced energy cost of ammonia synthesis via RF plasma pulsing. *ACS Sustainable Chemistry & Engineering* **2022**, *10* (46), 15135-15147.

(34) Zhang, J.; Li, X.; Zheng, J.; Du, M.; Wu, X.; Song, J.; Cheng, C.; Li, T.; Yang, W. Non-thermal plasma-assisted ammonia production: A review. *Energy Conversion and Management* **2023**, *293*, 117482.

(35) Zhou, D.; Zhou, R.; Zhou, R.; Liu, B.; Zhang, T.; Xian, Y.; Cullen, P. J.; Lu, X.; Ostrikov, K. K. Sustainable ammonia production by non-thermal plasmas: Status, mechanisms, and opportunities. *Chemical Engineering Journal* **2021**, *421*, 129544.

(36) Ma, X.; Li, S.; Hessel, V.; Lin, L.; Meskers, S.; Gallucci, F. Synthesis of luminescent carbon quantum dots by microplasma process. *Chemical Engineering and Processing-Process Intensification* **2019**, *140*, 29-35.

(37) Rasal, A. S.; Yadav, S.; Yadav, A.; Kashale, A. A.; Manjunatha, S. T.; Altaee, A.; Chang, J.-Y. Carbon quantum dots for energy applications: a review. *ACS Applied Nano Materials* **2021**, *4* (7), 6515-6541.

(38) Mangolini, L.; Thimsen, E.; Kortshagen, U. High-Yield Synthesis of Luminescent Silicon Quantum Dots in a Continuous Flow Nonthermal Plasma Reactor. *MRS Online Proceedings Library (OPL)* **2005**, *862*, A4. 3.

(39) Mangolini, L. Synthesis, properties, and applications of silicon nanocrystals. *Journal of Vacuum Science & Technology B* **2013**, *31* (2).

(40) Sahu, B. B.; Yin, Y.; Han, J. G.; Shiratani, M. Low temperature synthesis of silicon quantum dots with plasma chemistry control in dual frequency non-thermal plasmas. *Physical Chemistry Chemical Physics* **2016**, *18* (23), 15697-15710.

(41) Wu, J. J.; Kondeti, V. S. S. K.; Bruggeman, P. J.; Kortshagen, U. R. Luminescent, water-soluble silicon quantum dots via micro-plasma surface treatment. *Journal of Physics D: Applied Physics* **2016**, *49* (8), 08LT02.

(42) Hunter, K. I.; Held, J. T.; Mkhoyan, K. A.; Kortshagen, U. R. Nonthermal plasma synthesis of core/shell quantum dots: strained Ge/Si nanocrystals. *ACS Applied Materials & Interfaces* **2017**, *9* (9), 8263-8270.

(43) Kortshagen, U.; Anthony, R.; Gresback, R.; Holman, Z.; Ligman, R.; Liu, C.-Y.; Mangolini, L.; Campbell, S. A. Plasma synthesis of group IV quantum dots for luminescence and photovoltaic applications. *Pure and Applied Chemistry* **2008**, *80* (9), 1901-1908.

(44) Arts, K.; Hamaguchi, S.; Ito, T.; Karahashi, K.; Knoops, H. C.; Mackus, A. J.; Kessels, W. M. E. Foundations of atomic-level plasma processing in nanoelectronics. *Plasma Sources Science and Technology* **2022**, *31* (10), 103002.

(45) Sharma, S. K.; Barthwal, S.; Singh, V.; Kumar, A.; Dwivedi, P. K.; Prasad, B.; Kumar, D. PECVD based silicon oxynitride thin films for nano photonic on chip interconnects applications. *Micron* **2013**, *44*, 339-346.

(46) Knoops, H.; Faraz, T.; Arts, K.; Kessels, W. M. Status and prospects of plasma-assisted atomic layer deposition. *Journal of Vacuum Science & Technology A* **2019**, *37* (3).

(47) Oehrlein, G. S. Reactive-Ion Etching. *Physics Today* **1986**, *39* (10), 26-33.

(48) Schwartz, G.; Schaible, P. Reactive ion etching of silicon. *Journal of Vacuum Science and Technology* **1979**, *16* (2), 410-413.

(49) Bhattacharya, S.; Agarwal, A. K.; Rajagopalan, T.; Patel, V. K. *Nano-Energetic Materials*; Springer, 2019.

(50) De Luca, L. T.; Shimada, T.; Sinditskii, V. P.; Calabro, M. Chemical rocket propulsion: A comprehensive survey of energetic materials. **2016**.

(51) Badgujar, D.; Talawar, M.; Asthana, S.; Mahulikar, P. Advances in science and technology of modern energetic materials: an overview. *Journal of hazardous materials* **2008**, *151* (2-3), 289-305.

(52) Jena, S.; Gupta, A. Nano-energetic materials for defense application. *Nano-energetic materials* **2019**, 81-108.

(53) Piercey, D. G.; Klapoetke, T. M. Nanoscale aluminum-metal oxide (thermite) reactions for application in energetic materials. *Central European Journal of Energetic Materials* **2010**, *7* (2), 115-129.

(54) Sundaram, D.; Yang, V.; Yetter, R. A. Metal-based nanoenergetic materials: synthesis, properties, and applications. *Progress in Energy and Combustion Science* **2017**, *61*, 293-365.

(55) Sundaram, D. S.; Puri, P.; Yang, V. A general theory of ignition and combustion of nano-and micron-sized aluminum particles. *Combustion and Flame* **2016**, *169*, 94-109.

(56) Trunov, M. A.; Schoenitz, M.; Dreizin, E. Effect of polymorphic phase transformations in alumina layer on ignition of aluminium particles. *Combustion Theory and Modelling* **2006**, *10* (4), 603-623.

(57) Yetter, R. A.; Risha, G. A.; Son, S. F. Metal particle combustion and nanotechnology. *Proceedings of the combustion institute* **2009**, *32* (2), 1819-1838.

(58) Yeh, C.-L.; Kuo, K. Ignition and combustion of boron particles. *Progress in Energy and Combustion Science* **1996**, *22* (6), 511-541.

(59) Dreizin, E.; Keil, D.; Felder, W.; Vicenzi, E. Phase changes in boron ignition and combustion. *Combustion and Flame* **1999**, *119* (3), 272-290.

(60) Taylor, T. P.; Ding, M.; Ehler, D. S.; Foreman, T. M.; Kaszuba, J. P.; Sauer, N. N. Beryllium in the environment: a review. *Journal of Environmental Science and Health, Part A* **2003**, *38* (2), 439-469.

(61) Maček, A. Fundamentals of combustion of single aluminum and beryllium particles. In *Symposium (International) on Combustion*, 1967; Elsevier: Vol. 11, pp 203-217.

(62) Davydov, D.; Kholopova, O.; Kolbasov, B. Some characteristics of fine beryllium particle combustion. *Journal of nuclear materials* **2007**, *367*, 1079-1084.

(63) Glotov, O. G. Ignition and combustion of titanium particles: experimental methods and results. *Physics-Uspekhi* **2019**, *62* (2), 131.

(64) Chavoshi, S. Z.; Xu, S.; Goel, S. Addressing the discrepancy of finding the equilibrium melting point of silicon using molecular dynamics simulations. *Proceedings of the Royal Society A: Mathematical, Physical and Engineering Sciences* **2017**, *473* (2202), 20170084.

(65) Helms, C. R.; Poindexter, E. H. The silicon-silicon dioxide system: Its microstructure and imperfections. *Reports on progress in physics* **1994**, *57* (8), 791.

(66) Xu, F.; Nava, G.; Biswas, P.; Dulalia, I.; Wang, H.; Alibay, Z.; Gale, M.; Kline, D. J.; Wagner, B.; Mangolini, L. Energetic characteristics of hydrogenated amorphous silicon nanoparticles. *Chemical Engineering Journal* **2022**, *430*, 133140.

(67) Liao, Y.-C.; Nienow, A. M.; Roberts, J. T. Surface chemistry of aerosolized nanoparticles: thermal oxidation of silicon. *The Journal of Physical Chemistry B* **2006**, *110* (12), 6190-6197.

(68) Futko, S.; Koznacheev, I.; Rabinovich, O.; Penyazkov, O.; Krivosheyev, P. On the mechanism of combustion of thin nanostructurized silicon plates in oxygen at an elevated pressure. *Journal of Engineering Physics and Thermophysics* **2019**, *92*, 1-11.

(69) Plessis, M. d. A Decade of Porous Silicon as Nano-Explosive Material. *Propellants, Explosives, Pyrotechnics* **2014**, *39* (3), 348-364.

(70) Kovalev, D.; Timoshenko, V. Y.; Künzner, N.; Gross, E.; Koch, F. Strong explosive interaction of hydrogenated porous silicon with oxygen at cryogenic temperatures. *Physical Review Letters* **2001**, *87* (6), 068301.

(71) Ghildiyal, P.; Biswas, P.; Herrera, S.; Xu, F.; Alibay, Z.; Wang, Y.; Wang, H.; Abbaschian, R.; Zachariah, M. R. Vaporization-controlled energy release mechanisms

underlying the exceptional reactivity of magnesium nanoparticles. *ACS Applied Materials & Interfaces* **2022**, *14* (15), 17164-17174.

(72) Shafirovich, E.; Diakov, V.; Varma, A. Combustion of novel chemical mixtures for hydrogen generation. *Combustion and Flame* **2006**, *144* (1), 415-418.

(73) Machado, M. A.; Rodriguez, D. A.; Aly, Y.; Schoenitz, M.; Dreizin, E. L.; Shafirovich, E. Nanocomposite and mechanically alloyed reactive materials as energetic additives in chemical oxygen generators. *Combustion and Flame* **2014**, *161* (10), 2708-2716.

(74) Kabra, S.; Gharde, S.; Gore, P. M.; Jain, S.; Khire, V. H.; Kandasubramanian, B. Recent trends in nanothermites: Fabrication, characteristics and applications. *Nano Express* **2020**, *1* (3), 032001.

(75) Hobosyan, M. A.; Martirosyan, K. S. Novel nanoenergetic materials: emerging trends and applications. *IEEE Nanotechnology Magazine* **2019**, *14* (1), 30-36.

(76) Sullivan, K.; Piekiel, N.; Chowdhury, S.; Wu, C.; Zachariah, M.; Johnson, C. Ignition and combustion characteristics of nanoscale Al/AgIO3: A potential energetic biocidal system. *Combustion Science and Technology* **2010**, *183* (3), 285-302.

(77) Clark, B. R.; Pantoya, M. L. The aluminium and iodine pentoxide reaction for the destruction of spore forming bacteria. *Physical Chemistry Chemical Physics* **2010**, *12* (39), 12653-12657.

(78) Gottardi, W. Iodine and iodine compounds. **1983**.

(79) Davila, I. *Biocidal Defeat Agents Produced by Silver-Iodine Nanoenergetic Gas Generators*; The University of Texas Rio Grande Valley, 2017.

(80) Morones, J. R.; Elechiguerra, J. L.; Camacho, A.; Holt, K.; Kouri, J. B.; Ramírez, J. T.; Yacaman, M. J. The bactericidal effect of silver nanoparticles. *Nanotechnology* **2005**, *16* (10), 2346.

(81) Yoo, J.-Y.; Jang, E.-Y.; Jeong, S.-Y.; Hwang, D.-Y.; Son, H.-J. Bacterial indoleacetic acid-induced synthesis of colloidal Ag 2 O nanocrystals and their biological activities. *Bioprocess and biosystems engineering* **2019**, *42*, 401-414.

(82) Liao, C.; Li, Y.; Tjong, S. C. Bactericidal and cytotoxic properties of silver nanoparticles. *International journal of molecular sciences* **2019**, *20* (2), 449.

(83) Ghildiyal, P.; Ke, X.; Biswas, P.; Nava, G.; Schwan, J.; Xu, F.; Kline, D. J.; Wang, H.; Mangolini, L.; Zachariah, M. R. Silicon nanoparticles for the reactivity and energetic density enhancement of energetic-biocidal mesoparticle composites. *ACS Applied Materials & Interfaces* **2020**, *13* (1), 458-467.

(84) Reverberi, A. P.; Meshalkin, V. P.; Butusov, O. B.; Chistyakova, T. B.; Ferretti, M.; Cardinale, A. M.; Fabiano, B. Organic and inorganic biocidal energetic materials for agent defeat weapons: An overview and research perspectives. *Energies* **2023**, *16* (2), 675.

(85) Senyurt, E. I.; Schoenitz, M.; Dreizin, E. L. Rapid destruction of sarin surrogates by gas phase reactions with focus on diisopropyl methylphosphonate (DIMP). *Defence Technology* **2021**, *17* (3), 703-714.

(86) Senyurt, E. I.; Watson, K.; Zambon, A. C.; Feldman, G.; Sinha, N.; Hoffmann, V. K.; Schoenitz, M.; Dreizin, E. L. Experimental characterization of the low-temperature thermal decomposition of diisopropyl methylphosphonate (DIMP). *Chemical Engineering Journal* **2024**, *479*, 147832.

(87) Senyurt, E. I.; Das, S.; Kenny, T.; Groven, L. J.; Schoenitz, M.; Dreizin, E. L. Interaction of Diisopropyl methyl Phosphonate (DIMP) with magnesium oxide at elevated temperatures. *Applied Surface Science* **2024**, 160853.

(88) Ghosh Chaudhuri, R.; Paria, S. Core/shell nanoparticles: classes, properties, synthesis mechanisms, characterization, and applications. *Chemical reviews* **2012**, *112* (4), 2373-2433.

(89) Song, Y.-l.; Huang, Q.; Jin, B.; Peng, R.-f. Preparation and characterization of HMX/NH2-GO composite with enhanced thermal safety and desensitization. *Defence Technology* **2022**, *18* (11), 2074-2082.

(90) Yang, Z.; Ding, L.; Wu, P.; Liu, Y.; Nie, F.; Huang, F. Fabrication of RDX, HMX and CL-20 based microcapsules via in situ polymerization of melamine–formaldehyde resins with reduced sensitivity. *Chemical Engineering Journal* **2015**, *268*, 60-66.

(91) Berner, M.; Zarko, V. E.; Talawar, M. B. Nanoparticles of energetic materials: synthesis and properties. *Combustion, Explosion, and Shock Waves* **2013**, *49*, 625-647.

(92) Kwon, Y.-S.; Gromov, A. A.; Ilyin, A. P.; Rim, G.-H. Passivation process for superfine aluminum powders obtained by electrical explosion of wires. *Applied Surface Science* **2003**, *211* (1-4), 57-67.

(93) Guo, L.; Song, W.; Hu, M.; Xie, C.; Chen, X. Preparation and reactivity of aluminum nanopowders coated by hydroxyl-terminated polybutadiene (HTPB). *Applied Surface Science* **2008**, *254* (8), 2413-2417.

(94) Lijun, Q.; Ting, G.; Haixia, H.; Keyong, W.; Hao, F. Influences of metal oxide encapsulation by atomic layer deposition on the sensitivities of octogen. *Gaodeng Xuexiao Huaxue Xuebao/Chemical Journal of Chinese Universities* **2015**, *36*, 420-427.

(95) Wang, J.; Liu, D.; Zhang, J.; Gong, F.; Zhao, X.; Yang, Z. Design of conductive polymer coating layer for effective desensitization of energetic materials. *Chemical Engineering Journal* **2024**, *482*, 148874.

(96) Duan, B.; Mo, H.; Tan, B.; Xu, M.; Lu, X.; Liu, N.; Wang, B. In situ coating of energetic crystals: A compact core-shell structure with highly reduced sensitivity. *FirePhysChem* **2023**, *3* (2), 89-97.

(97) Dubois, C.; Lafleur, P. G.; Roy, C.; Brousseau, P.; Stowe, R. A. Polymer-grafted metal nanoparticles for fuel applications. *Journal of Propulsion and Power* **2007**, *23* (4), 651-658.

(98) Brousseau, P.; Dubois, C. Polymer-coated ultra-fine particles. *MRS Online Proceedings Library (OPL)* **2005**, *896*, 0896-H0802-0802.

(99) Cao, Z.; Hu, A.; Xia, B.; Pang, A. m.; Cai, S. Preparation and characterization of aluminum-lithium alloy powder coated by in-situ polymerization of styrene. *Propellants, Explosives, Pyrotechnics* **2020**, *45* (7), 1141-1152.

(100) Pourmortazavi, S. M.; Babaee, S.; Ashtiani, F. S. Statistical optimization of microencapsulation process for coating of magnesium particles with Viton polymer. *Applied Surface Science* **2015**, *349*, 817-825.

(101) Wang, J.; Li, Y.; Han, Z.; Song, S.; Li, J. Study on the preparation and combustion performance of AlF composites prepared by a solvent/non-solvent method. *Surface and Coatings Technology* **2022**, *440*, 128455.

(102) Hosseini, S. G.; Sharifnezhad, H.; Fathollahi, M.; Abotorabe, A.; Ghaenii, H. R. Improvement of electrostatic discharge sensitivity of lead styphnate particles using some polymer coating agents. *Journal of Energetic Materials* **2023**, *41* (1), 117-128.

(103) Liu, W.-J.; Cheng, Y.-F.; Fang, H.; Yao, Y.-L.; Tao, C.; Chen, Y.; Shen, Z.-W. Fabrication and characterization of PMMA/TiH2 energetic microcapsules with a hollow structure. *Journal of Energetic Materials* **2020**, *38* (4), 406-417.

(104) Wang, J.; Chen, J.; Mao, Y.; Zhang, X.; Wang, J.; Nie, F. Synergistic reaction of spherical B/Al/PTFE fuel prepared by confinement-emulsion-templated strategy to achieve high energy and reactivity. *Combustion and Flame* **2024**, *259*, 113113.

(105) Fischer, S. H.; Grubelich, M. *Theoretical energy release of thermites, intermetallics, and combustible metals*; Sandia National Lab.(SNL-NM), Albuquerque, NM (United States), 1998.

(106) Chrifi-Alaoui, F.; Nassik, M.; Mahdouk, K.; Gachon, J. Enthalpies of formation of the Al–Ni intermetallic compounds. *Journal of Alloys and Compounds* **2004**, *364* (1-2), 121-126.

(107) Chung, H.; Lee, J.-Y. Hydriding and dehydriding reaction rate of FeTi intermetallic compound. *International journal of Hydrogen energy* **1985**, *10* (7-8), 537-542.

(108) Novák, P.; Michalcová, A.; Marek, I.; Mudrová, M.; Saksl, K.; Bednarčík, J.; Zikmund, P.; Vojtěch, D. On the formation of intermetallics in Fe–Al system–An in situ XRD study. *Intermetallics* **2013**, *32*, 127-136.

(109) Ma, E. Alloys created between immiscible elements. *Progress in materials science* **2005**, *50* (4), 413-509.

(110) HUANG, Y.; DU, J.; WANG, Z. Progress in research on the alloying of binary immiscible metals. *Acta Metall Sin* **2020**, *56* (6), 801-820.

(111) Foley, T. J.; Johnson, C. E.; Higa, K. T. Inhibition of oxide formation on aluminum nanoparticles by transition metal coating. *Chemistry of Materials* **2005**, *17* (16), 4086-4091.

(112) Nguyen, N. H.; Hu, A.; Persic, J.; Wen, J. Z. Molecular dynamics simulation of energetic aluminum/palladium core–shell nanoparticles. *Chemical Physics Letters* **2011**, *503* (1-3), 112-117.

(113) Wen, J. Z.; Nguyen, N. H.; Rawlins, J.; Petre, C. F.; Ringuette, S. Influence of shell thickness on thermal stability of bimetallic Al–Pd nanoparticles. *Journal of nanoparticle research* **2014**, *16*, 1-12.

(114) Ha Nguyen, N.; Z Wen, J. Theoretical Investigations on Diffusion Induced Thermite Reactions of Core-Shell Aluminum/Palladium Nanoparticles. *The Open Surface Science Journal* **2011**, *3* (1).

(115) Pan, B.; Yan, S.; Yuan, Q.; Li, S.; Guo, X.; Nie, J.; Jiao, Q. Exploding wire preparation of core–shell aluminum–silicon nanoparticles and characterization as energetic material. *Journal of Nanoparticle Research* **2021**, *23*, 1-11.

(116) Wang, C.; Zou, X.; Yin, S.; Wang, J.; Li, H.; Liu, Y.; Wang, N.; Shi, B. Improvement of ignition and combustion performance of micro-aluminum particles by double-shell nickel-phosphorus alloy coating. *Chemical Engineering Journal* **2022**, *433*, 133585.

(117) Chintersingh, K.-L.; Schoenitz, M.; Dreizin, E. L. Effect of purity, surface modification and iron coating on ignition and combustion of boron in air. *Combustion Science and Technology* **2021**, *193* (9), 1567-1586.

(118) Ma, K.; Zhu, B.; Chen, J.; Zhao, X.; Sun, Y. Nickel improving the combustion of boron powder. *Thermochimica Acta* **2022**, *718*, 179368.

(119) Rosenband, V.; Natan, B.; Gany, A. Ignition of boron particles coated by a thin titanium film. *Journal of Propulsion and Power* **1995**, *11* (6), 1125-1131.

(120) Pace, K.; Jarymowycz, T.; Yang, V. Effect of magnesium-coated boron particles on burning characteristics of solid fuels in high-speed crossflows. *International Journal of Energetic Materials and Chemical Propulsion* **1993**, *2* (1-6).

(121) Yeh, C.-L.; Hsieh, W.; Felder, W. Ignition and combustion of Mg-coated and uncoated boron particles. *International Journal of Energetic Materials and Chemical Propulsion* **1994**, *3* (1-6).

(122) Liu, L.-l.; Liu, P.-j.; He, G.-q. Ignition and combustion characteristics of compound of magnesium and boron. *Journal of Thermal Analysis and Calorimetry* **2015**, *121* (3), 1205-1212. DOI: 10.1007/s10973-015-4653-6.

(123) Wang, L. L.; Munir, Z.; Maximov, Y. M. Thermite reactions: their utilization in the synthesis and processing of materials. *Journal of Materials Science* **1993**, *28*, 3693-3708.

(124) Kang, X.; Li, C.; Zheng, Z.; Cui, X. Facile preparation of micrometer KClO4/Zr energetic composite particles with enhanced light radiation. *Materials* **2019**, *12* (2), 199.

(125) Yang, F.; Kang, X.; Luo, J.; Yi, Z.; Tang, Y. Preparation of core-shell structure KClO4@ Al/CuO Nanoenergetic material and enhancement of thermal behavior. *Scientific Reports* **2017**, *7* (1), 3730.

(126) Zhang, J.; Ding, L.; Zhang, H.; Hu, L.; Lin, K.; Yang, Y. Preparation and study on combustion performance of AP@ ZrH2 core-shell composite energetic materials with high volume energy density. *Advanced Powder Technology* **2024**, *35* (4), 104402.

(127) Liao, X.; Liu, J.; Xu, P.; Sun, M. AP and nFe2O3 synergistically improve the ignition and combustion performance of aluminum particles. *Journal of Thermal Analysis and Calorimetry* **2023**, *148* (21), 11669-11681.

(128) Xu, R.; Yu, M.; Xue, Z.; Zhang, H.; Yan, Q.-L. Enhancing the Ignition and Combustion Performances of Solid Propellants Incorporating Al Particles Inside Oxidizers. *ACS Applied Materials & Interfaces* **2023**, *15* (48), 56442-56453.

(129) Nie, H.; Yang, S.-L.; Yan, Q.-L. Enhancement in ignition and combustion of solid propellants by interfacial modification of Al/AP composites with transition metals. *Combustion and Flame* **2023**, *256*, 112968.

(130) He, W.; Lyu, J.-Y.; Tang, D.-Y.; He, G.-Q.; Liu, P.-J.; Yan, Q.-L. Control the combustion behavior of solid propellants by using core-shell Al-based composites. *Combustion and Flame* **2020**, *221*, 441-452.

(131) Ao, W.; Wen, Z.; Liu, L.; Wang, Y.; Zhang, Y.; Liu, P.; Qin, Z.; Li, L. K. Combustion and agglomeration characteristics of aluminized propellants containing Al/CuO/PVDF metastable intermolecular composites: A highly adjustable functional catalyst. *Combustion and Flame* **2022**, *241*, 112110.

(132) Kappagantula, K. S.; Pantoya, M. L.; Horn, J. Effect of surface coatings on aluminum fuel particles toward nanocomposite combustion. *Surface and Coatings Technology* **2013**, *237*, 456-459.

(133) Zhang, L.; Wang, S.; Su, X.; Li, X.; Zou, M. Preparation and characterization of core-shell Al@ PFHP with improving the combustion and ignition properties of aluminum powder. *Particuology* **2023**, *77*, 62-70.

(134) Prakash, A.; McCormick, A.; Zachariah, M. Tuning the reactivity of energetic nanoparticles by creation of a core− shell nanostructure. *Nano Letters* **2005**, *5* (7), 1357-1360.

(135) Yan, N.; Qin, L.; Hao, H.; Hui, L.; Zhao, F.; Feng, H. Iron oxide/aluminum/graphene energetic nanocomposites synthesized by atomic layer deposition: Enhanced energy

release and reduced electrostatic ignition hazard. *Applied Surface Science* **2017**, *408*, 51-59.

(136) Zhou, X.; Wang, Y.; Cheng, Z.; Ke, X.; Jiang, W. Facile preparation and energetic characteristics of core-shell Al/CuO metastable intermolecular composite thin film on a silicon substrate. *Chemical Engineering Journal* **2017**, *328*, 585-590.

(137) Ma, X.; Cheng, S.; Hu, Y.; Ye, Y.; Shen, R. Integrating micro-ignitors with Al/Bi2O3/graphene oxide composite energetic films to realize tunable ignition performance. *Journal of Applied Physics* **2018**, *123* (9).

(138) Xu, D.; Yang, Y.; Cheng, H.; Li, Y. Y.; Zhang, K. Integration of nano-Al with Co3O4 nanorods to realize high-exothermic core–shell nanoenergetic materials on a silicon substrate. *Combustion and Flame* **2012**, *159* (6), 2202-2209.

(139) Kopacz, W.; Okninski, A.; Kasztankiewicz, A.; Nowakowski, P.; Rarata, G.; Maksimowski, P. Hydrogen peroxide–A promising oxidizer for rocket propulsion and its application in solid rocket propellants. *FirePhysChem* **2022**, *2* (1), 56-66.

(140) Dennis, C.; Bojko, B. On the combustion of heterogeneous AP/HTPB composite propellants: A review. *Fuel* **2019**, *254*, 115646.

(141) Yang, S.-L.; Yu, M.-H.; He, W.; Nie, H.; Yan, Q.-L. The ignition and combustion performances of core-shell Al-based intermetallic nanocomposites surrounded with AP. *Combustion and Flame* **2023**, *248*, 112555.

(142) Liu, Y.; Wang, Y.; Liu, Y.; Zhao, B.; Liu, W.; Yan, Q.; Fu, X. High calorific values boron powder: Ignition and combustion mechanism, surface modification strategies and properties. *Molecules* **2023**, *28* (7), 3209.

(143) Yang, S.-L.; Xu, R.; He, W.; Nie, H.; Yan, Q.-L. Enhancing the thermal reactivity of AP crystals by coating of Al-based bi-metal nanocomposites. *Fuel* **2022**, *324*, 124588.

(144) Zhou, Z.; Tian, S.; Zeng, D.; Tang, G.; Xie, C. MOX (M= Zn, Co, Fe)/AP shell–core nanocomposites for self-catalytical decomposition of ammonium perchlorate. *Journal of Alloys and compounds* **2012**, *513*, 213-219.

(145) Wu, X.-z.; Ren, H.; Xie, L.-j. Enhancement of aluminum powder reaction behavior at high temperatures—Aluminum powders with “sea urchin structure” coated by AP. *Fuel* **2024**, *375*, 132596.

(146) Zhou, X.; Xu, R.; Nie, H.; Yan, Q.; Liu, J.; Sun, Y. Insight into the precise catalytic mechanism of CuO on the decomposition and combustion of core–shell Al@ AP particles. *Fuel* **2023**, *346*, 128294.

(147) Lyu, J.-Y.; Xu, G.; Zhang, H.; Yang, W.; Yan, Q.-L. Thermal decomposition and combustion behavior of the core-shell Al@ AP composite embedded with CuO as a catalyst. *Fuel* **2024**, *356*, 129587.

(148) Valluri, S. K.; Schoenitz, M.; Dreizin, E. Fluorine-containing oxidizers for metal fuels in energetic formulations. *Defence Technology* **2019**, *15* (1), 1-22.

(149) Shen, C.; Yan, S.; Tan, Y.; Ou, Y.; Jiao, Q.; Luo, Y. Enhancing energy release of aluminized propellants and explosives through fluorinated binder. *Propellants, Explosives, Pyrotechnics* **2024**, *49* (3), e202300199.

(150) Tang, W.; Yang, R.; Li, J.; Li, J.; Liu, Z.; Huo, Z.; Hu, J.; Zeng, T.; Zhou, X. Core-shell particle of aluminum-copper perfluorooctanoate configurations and its ignition and combustion properties. *Combustion and Flame* **2022**, *245*, 112270.

(151) Xiao, F.; Zhang, H.; Liu, W.; Zhang, J.; Liang, T.; Hu, J.; Zhang, Y.; Luo, P. Enhanced combustion performance of core-shell aluminum with poly (vinylidene fluoride) interfacial layer: Constructing the combination bridge of aluminum powder and poly (vinylidene fluoride). *Surface and Coatings Technology* **2022**, *439*, 128410.

(152) Zhou, X.; Gong, L.; Huang, F.; Yang, R.; Li, J. Mechanism of the organic fluoride effect on the formation of agglomerates and condensed products in the combustion of aluminised solid propellants. *Combustion Theory and Modelling* **2020**, *24* (1), 1-14.

(153) Hu, Y.; Hao, D.; Tao, B.; Wang, F.; Wang, D.; Fan, R.; Xia, D.; Wang, P.; Yang, Y.; Pang, A. Core-shell nAl@ Fc-Fx nanocomposites with dual function: Combustion and anti-migration performance. *Chemical Engineering Journal* **2020**, *394*, 124884.

(154) Ao, W.; Liu, P.; Liu, H.; Wu, S.; Tao, B.; Huang, X.; Li, L. K. Tuning the agglomeration and combustion characteristics of aluminized propellants via a new functionalized fluoropolymer. *Chemical Engineering Journal* **2020**, *382*, 122987.

(155) Liu, Y.; Wang, W.; Zhao, B.; Chen, B.; Wang, Y.; Yan, Q. Synergistic Enhancement on Ignition and Combustion Properties of Boron via Viton Core–Shell Coating. *Langmuir* **2024**, *40* (23), 12239-12249. DOI: 10.1021/acs.langmuir.4c01316.

(156) Xu, Y.; Cui, Q.-z.; Zhao, C.-w. Liquid phase in-situ synthesis of LiF coated boron powder composite and performance study. *Defence Technology* **2020**, *16* (3), 635-641. DOI: https://doi.org/10.1016/j.dt.2019.08.016.

(157) Valluri, S. K.; Schoenitz, M.; Dreizin, E. Bismuth fluoride-coated boron powders as enhanced fuels. *Combustion and Flame* **2020**, *221*, 1-10. DOI: https://doi.org/10.1016/j.combustflame.2020.07.023.

(158) Zuo, B.; Wang, S.-Z.; Yang, S.; Liu, P.; Yan, Q.-L. Thermal decomposition and combustion behavior of solid propellant containing Si-based composites. *Combustion and Flame* **2022**, *240*, 111959. DOI: https://doi.org/10.1016/j.combustflame.2021.111959.

(159) Zhuang, Z.; Xu, K.; Liu, B.; Shi, Y.; Li, S.; Liu, Z.; He, C.; Liu, J. Improved reactivity and energy release performance of core-shell structured fuel-rich Si/PTFE energetic composites. *Combustion and Flame* **2023**, *255*, 112889. DOI: https://doi.org/10.1016/j.combustflame.2023.112889.

(160) Shancita, I.; Vaz, N. G.; Fernandes, G. D.; Aquino, A. J. A.; Tunega, D.; Pantoya, M. L. Regulating magnesium combustion using surface chemistry and heating rate. *Combustion and Flame* **2021**, *226*, 419-429. DOI: https://doi.org/10.1016/j.combustflame.2020.12.024.

(161) Zhou, X.; Xu, D.; Yang, G.; Zhang, Q.; Shen, J.; Lu, J.; Zhang, K. Highly Exothermic and Superhydrophobic Mg/Fluorocarbon Core/Shell Nanoenergetic Arrays. *ACS Applied Materials & Interfaces* **2014**, *6* (13), 10497-10505. DOI: 10.1021/am502078e.

(162) Rider, K. B.; Little, B. K.; Emery, S. B.; Lindsay, C. M. Thermal Analysis of Magnesium/Perfluoropolyether Pyrolants. *Propellants, Explosives, Pyrotechnics* **2013**, *38* (3), 433-440. DOI: https://doi.org/10.1002/prep.201200118 (acccessed 2024/08/25).

(163) Valliappan, S.; Swiatkiewicz, J.; Puszynski, J. A. Reactivity of aluminum nanopowders with metal oxides. *Powder Technology* **2005**, *156* (2), 164-169. DOI: https://doi.org/10.1016/j.powtec.2005.04.027.

(164) Kaplowitz, D. A.; Jian, G.; Gaskell, K.; Jacob, R.; Zachariah, M. R. Synthesis and Reactive Properties of Iron Oxide–Coated Nanoaluminum. *Journal of Energetic Materials* **2014**, *32* (2), 95-105. DOI: 10.1080/07370652.2013.767288.

(165) Hübner, J.; Klaumünzer, M.; Comet, M.; Martin, C.; Vidal, L.; Schäfer, M.; Kryschi, C.; Spitzer, D. Insights into combustion mechanisms of variable aluminum-based iron oxide/-hydroxide nanothermites. *Combustion and Flame* **2017**, *184*, 186-194. DOI: https://doi.org/10.1016/j.combustflame.2017.06.006.

(166) Maini, S.; Wang, A.; Wen, J. Z. Fluctuating Flame from Suspending Ferrimagnetic Core/Shell Al@Fe3O4 Nanoparticles in a Magnetic Field. *Advanced Materials Interfaces* **2024**, *n/a* (n/a), 2400328. DOI: https://doi.org/10.1002/admi.202400328 (acccessed 2024/08/25).

(167) Ferguson, J. D.; Buechler, K. J.; Weimer, A. W.; George, S. M. SnO2 atomic layer deposition on ZrO2 and Al nanoparticles: Pathway to enhanced thermite materials. *Powder Technology* **2005**, *156* (2), 154-163. DOI: https://doi.org/10.1016/j.powtec.2005.04.009.

(168) Maini, S.; Wang, A.; Wen, J. Z. Characteristics of Gasless Combustion of Core–Shell Al@NiO Microparticles with Boosted Exothermic Performance. *ACS Omega* **2024**. DOI: 10.1021/acsomega.4c04107.

(169) Chen, J.; Ren, W.; Hu, B.; Zheng, Z.; Chen, Y.; Chen, J.; Yu, C.; Song, C.; Wang, J.; Zhang, W. Effect of the Ni and NiO Interface Layer on the Energy Performance of Core/Shell CuO/Al Systems. *Langmuir* **2020**, *36* (43), 12858-12865. DOI: 10.1021/acs.langmuir.0c02045.

(170) Alibay, Z.; Olsen, D.; Biswas, P.; England, C.; Xu, F.; Ghildiyal, P.; Zhou, M.; Zachariah, M. R. Microwave Stimulation of Energetic Al-Based Nanoparticle Composites for Ignition Modulation. *ACS Applied Nano Materials* **2022**, *5* (2), 2460-2469. DOI: 10.1021/acsanm.1c04157.

(171) Qin, L.; Gong, T.; Hao, H.; Wang, K.; Feng, H. Core–shell-structured nanothermites synthesized by atomic layer deposition. *Journal of Nanoparticle Research* **2013**, *15* (12), 2150. DOI: 10.1007/s11051-013-2150-z.

(172) Zhang, J.; Wang, E.; Yu, C.; Xie, J.; Tang, C.; Jia, Y. Reaction mechanism of core–shell Al@SiO2 nanoparticles from molecular dynamics simulations. *Modelling and Simulation in Materials Science and Engineering* **2022**, *30* (8), 085009. DOI: 10.1088/1361-651X/ac9d55.

(173) Ke, X.; Zhou, X.; Gao, H.; Hao, G.; Xiao, L.; Chen, T.; Liu, J.; Jiang, W. Surface functionalized core/shell structured CuO/Al nanothermite with long-term storage stability and steady combustion performance. *Materials & Design* **2018**, *140*, 179-187. DOI: https://doi.org/10.1016/j.matdes.2017.11.068.

(174) Deshmukh, P. R.; Lee, H.; Kim, Y.; Shin, W. G. Ignition and oxidation performance of SnO2 coated boron particles: A solid fuel for energetic applications. *Journal of Alloys and Compounds* **2021**, *886*, 161123. DOI: https://doi.org/10.1016/j.jallcom.2021.161123.

(175) Mondal, J.; Singh, S. K.; Shin, W. G. Enhanced ignition and combustion performance of boron-based energetic materials through surface modification and titanium dioxides coating. *Ceramics International* **2024**, *50* (9, Part B), 16598-16614. DOI: https://doi.org/10.1016/j.ceramint.2024.02.150.

(176) Huang, Q.; Zhang, C.; Guo, K.; Zeng, Y.; Mingxing, Z.; Wen-long, R.; Xiong, D.; Lin, Z.; Zhu, C. High-efficiency synthesis of B@Mg@KNO3 by solvent extraction enhances the ignition and energy release performance of B. *Journal of Alloys and Compounds* **2024**, *1004*, 175780. DOI: https://doi.org/10.1016/j.jallcom.2024.175780.

(177) Agarwal, P. P. K.; Jensen, D.; Chen, C.-H.; Rioux, R. M.; Matsoukas, T. Synthesis and Characterization of Magnesium/Boron Solid Solutions for Energetic Applications. *ACS Applied Energy Materials* **2022**, *5* (6), 6716-6723. DOI: 10.1021/acsaem.2c00312.

(178) Zhou, X.; Xu, D.; Zhang, Q.; Lu, J.; Zhang, K. Facile Green In Situ Synthesis of Mg/CuO Core/Shell Nanoenergetic Arrays with a Superior Heat-Release Property and Long-Term Storage Stability. *ACS Applied Materials & Interfaces* **2013**, *5* (15), 7641-7646. DOI: 10.1021/am401955u.

(179) Huang, S.; Deng, S.; Jiang, Y.; Zhao, J.; Zheng, X. Electroless Deposition and Ignition Properties of Si/Fe2O3 Core/Shell Nanothermites. *ACS Omega* **2017**, *2* (7), 3596-3600. DOI: 10.1021/acsomega.7b00652.

(180) Qin, L.; Gong, T.; Li, J.; Yan, N.; Hui, L.; Feng, H. Tuning ignition and energy release properties of Zirconium powder by atomic layer deposited metal oxide coatings. *Journal of Hazardous Materials* **2019**, *378*, 120655. DOI: https://doi.org/10.1016/j.jhazmat.2019.05.048.

(181) Friedrich, J. F.; Meichsner, J. *Nonthermal Plasmas for Materials Processing*; John Wiley & Sons, 2022.

(182) Kouprine, A.; Gitzhofer, F.; Boulos, M.; Fridman, A. Kinetics of ultrafine coating of SiO2 nanoparticles, suspended in non-thermal CH4/C2H6 plasma. *Experimental thermal and fluid science* **2007**, *31* (8), 1005-1019.

(183) Post, P.; Jidenko, N.; Weber, A. P.; Borra, J.-P. Post-plasma SiO x coatings of metal and metal oxide nanoparticles for enhanced thermal stability and tunable photoactivity applications. *Nanomaterials* **2016**, *6* (5), 91.

(184) Abdollahi Far, M.; Shariat, M.; Sadeghzadeh Lari, E.; Hassani Matin, M. M. In-situ deposition of silver nanoparticles onto glass by non-thermal plasma jet. *The European Physical Journal D* **2024**, *78* (7), 82.

(185) Sangghaleh, F.; Sychugov, I.; Yang, Z.; Veinot, J. G.; Linnros, J. Near-unity internal quantum efficiency of luminescent silicon nanocrystals with ligand passivation. *ACS nano* **2015**, *9* (7), 7097-7104.

(186) Müller, M.; Galář, P.; Stuchlík, J.; Kočka, J.; Kupka, J.; Kůsová, K. Synthesis and surface modification of light emitting silicon nanoparticles using non-thermal plasma techniques. *The European Physical Journal Applied Physics* **2020**, *89* (2), 20401.

(187) Mangolini, L.; Jurbergs, D.; Rogojina, E.; Kortshagen, U. High efficiency photoluminescence from silicon nanocrystals prepared by plasma synthesis and organic surface passivation. *physica status solidi c* **2006**, *3* (11), 3975-3978.

(188) Reichel, C.; Reusch, M.; Kotula, S.; Granek, F.; Richter, A.; Hermle, M.; Glunz, S. W. Insulating and passivating plasma-enhanced atomic layer deposited aluminum oxide thin films for silicon solar cells. *Thin Solid Films* **2018**, *656*, 53-60.

(189) Ashok, A.; Vasanth, A.; Nagaura, T.; Eguchi, M.; Motta, N.; Phan, H. P.; Nguyen, N. T.; Shapter, J. G.; Na, J.; Yamauchi, Y. Plasma-induced nanocrystalline domain engineering and surface passivation in mesoporous chalcogenide semiconductor thin films. *Angewandte Chemie International Edition* **2022**, *61* (14), e202114729.

(190) Shahravan, A.; Desai, T.; Matsoukas, T. Passivation of aluminum nanoparticles by plasma-enhanced chemical vapor deposition for energetic nanomaterials. *ACS applied materials & interfaces* **2014**, *6* (10), 7942-7947.

(191) Agarwal, P. P.; Jensen, D.; Chen, C.-H.; Rioux, R. M.; Matsoukas, T. Surface-functionalized boron nanoparticles with reduced oxide content by nonthermal plasma processing for nanoenergetic applications. *ACS Applied Materials & Interfaces* **2021**, *13* (5), 6844-6853.

(192) Agarwal, P. P.; Matsoukas, T. Enhanced energetic performance of aluminum nanoparticles by plasma deposition of perfluorinated nanofilms. *ACS Applied Materials & Interfaces* **2022**, *14* (30), 35255-35264.

(193) Agarwal, P. P.; Haley, E. J.; Matsoukas, T. Synthesis and Characterization of Energetic Aluminum Boride Particles Coated with Reactive Plasma Nanofilms. *ACS Applied Engineering Materials* **2024**, *2* (2), 467-477.

(194) Hao, Y.; Huang, A.; Han, S.; Huang, H.; Song, J.; Sun, X.; Wang, Z.; Li, L.; Hu, F.; Xue, J. Plasma-treated ultrathin ternary FePSe3 nanosheets as a bifunctional electrocatalyst for efficient zinc–air batteries. *ACS applied materials & interfaces* **2020**, *12* (26), 29393-29403.

(195) Tang, J.; Su, C.; Shao, Z. Nonthermal plasma treatment for electrocatalysts structural and surface engineering. *Energy Technology* **2022**, *10* (9), 2200235.

(196) Kuang, Y.; Qiao, W.; Wang, S.; Yang, F.; Feng, L. Doping and Interfacial Engineering of MoSe2 Nanosheets by NH3 Plasma Promoted Pt for Methanol Electrolysis. *ACS Materials Letters* **2024**, *6* (5), 1722-1731.

(197) He, Y.; Sun, C.; Fang, S.; Shaban, M.; Chen, C. Facile synthesis of N-doped NiCo-LDH nanowire with rich oxygen vacancies by nonthermal plasma for high-performance asymmetric capacitor electrode. *Applied Surface Science* **2024**, *648*, 159006.

(198) Yang, J.; Zhu, X.; Yu, Q.; Zhou, G.; Li, Q.; Wang, C.; Hua, Y.; She, Y.; Xu, H.; Li, H. Plasma-induced defect engineering: Boosted the reverse water gas shift reaction performance with electron trap. *Journal of Colloid and Interface Science* **2020**, *580*, 814-821.

(199) Kuo, Y.-L.; Chen, H.-W.; Sun, Y.-S.; Liao, S.-C.; Su, Y.-M.; Lo, Y.-H. Nonthermal atmospheric pressure plasma jet-assisted formation of oxygen vacancies stabilized tetragonal zirconia particles. *Advanced Powder Technology* **2023**, *34* (9), 104109.

(200) Maillet, C.; Klein, F. M.; Le Bras, F.; Velard, F.; Guillaume, C.; Gangloff, S. C.; Gelle, M.-P. Cytocompatibility of titanium and poly (etheretherketone) surfaces after O2 non-thermal plasma sterilization. *Plos one* **2023**, *18* (8), e0290820.

(201) Tucker, B. S.; Aliakbarshirazi, S.; Vijayan, V. M.; Thukkaram, M.; De Geyter, N.; Thomas, V. Nonthermal plasma processing for nanostructured biomaterials and tissue engineering scaffolds: A mini review. *Current Opinion in Biomedical Engineering* **2021**, *17*, 100259.

(202) Udachin, V.; Wegewitz, L.; Szafarska, M.; Dahle, S.; Gustus, R.; Maus-Friedrichs, W. Atmospheric Non-thermal Plasma Reduction of Natively Oxidized Iron Surfaces. *Plasma Chemistry and Plasma Processing* **2023**, *43* (5), 957-974.

(203) Tu, Q.; Poerschke, D. L.; Kortshagen, U. R. Nonthermal Plasma Synthesis of Metallic Ti Nanocrystals. *Nanomaterials* **2024**, *14* (3), 264.

(204) Xu, F.; Biswas, P.; Ghildiyal, P.; Zachariah, M. R. Inducing oxygen vacancies to modulate ignition threshold of nanothermites. *Energy & Fuels* **2022**, *36* (11), 5878-5884.

(205) Wu, X.-l.; Xu, S.; Pang, A.-m.; Cao, W.-g.; Liu, D.-b.; Zhu, X.-y.; Xu, F.-y.; Wang, X. Hazard evaluation of ignition sensitivity and explosion severity for three typical MH2 (M= Mg, Ti, Zr) of energetic materials. *Defence Technology* **2021**, *17* (4), 1262-1268.

(206) Miller, K. K.; Shancita, I.; Bhattacharia, S. K.; Pantoya, M. L. Surface modifications of plasma treated aluminum particles and direct evidence for altered reactivity. *Materials & Design* **2021**, *210*, 110119.

(207) Wu, C.-C.; Miller, K. K.; Walck, S. D.; Pantoya, M. Material Characterization of Plasma-Treated Aluminum Particles via Different Gases. *MRS Advances* **2019**, *4* (27), 1589-1595. DOI: 10.1557/adv.2019.159 From Cambridge University Press Cambridge Core.

(208) Miller, K. K.; Gottfried, J. L.; Walck, S. D.; Pantoya, M. L.; Wu, C.-C. Plasma surface treatment of aluminum nanoparticles for energetic material applications. *Combustion and Flame* **2019**, *206*, 211-213. DOI: https://doi.org/10.1016/j.combustflame.2019.04.042.

(209) Micus, J. L.; Wu, C.-C.; Walck, S. D.; Thapa, D.; Pantoya, M. L. Hydration-induced plasma surface modification of aluminum nanoparticles for power generation in oxygen deficient environments. *Surface and Coatings Technology* **2024**, *488*, 131054.

(210) Zhang, Y.; Yang, F.; Zhao, F.; Xu, S. Interaction mechanism between metal hydrides and energetic compounds: an extensive literature survey. *FirePhysChem* **2022**, *2* (4), 303-314.

(211) Zhu, C.; Gao, W.; Jiang, H.; Xue, C.; Zhu, Z.; Tang, G. A comparative investigation of the explosion mechanism of metal hydride AlH3 dust and Al/H2 mixture. *International Journal of Hydrogen Energy* **2024**, *50*, 1296-1305.

(212) Agarwal, P. P.; Matsoukas, T. Engineered Surface Chemistry and Enhanced Energetic Performance of Aluminum Nanoparticles by Nonthermal Hydrogen Plasma Treatment. *Nano letters* **2023**, *23* (12), 5541-5547.

(213) Yetter, R. A. Progress towards nanoengineered energetic materials. *Proceedings of the Combustion Institute* **2021**, *38* (1), 57-81.

(214) Hawa, T.; Zachariah, M. Development of a phenomenological scaling law for fractal aggregate sintering from molecular dynamics simulation. *Journal of Aerosol Science* **2007**, *38* (8), 793-806.

(215) Van Devener, B.; Perez, J. P. L.; Jankovich, J.; Anderson, S. L. Oxide-free, catalyst-coated, fuel-soluble, air-stable boron nanopowder as combined combustion catalyst and high energy density fuel. *Energy & Fuels* **2009**, *23* (12), 6111-6120.

(216) Lomba, R.; Bernard, S.; Gillard, P.; Mounaïm-Rousselle, C.; Halter, F.; Chauveau, C.; Tahtouh, T.; Guézet, O. Comparison of combustion characteristics of magnesium and aluminum powders. *Combustion Science and Technology* **2016**, *188* (11-12), 1857-1877.

(217) Akiyama, M.; Nishii, K.; Mannami, Y.; Murohara, M.; Koizumi, H.; Komurasaki, K. Feasibility study of a hybrid thruster using wire-shaped magnesium and water for application to small spacecraft. *Transactions of the Japan Society for Aeronautical and Space Sciences* **2021**, *64* (4), 223-233.

(218) Law, C.; Williams, F. Combustion of magnesium particles in oxygen-inert atmospheres. *Combustion and Flame* **1974**, *22* (3), 383-405.

(219) Shancita, I.; Vaz, N. G.; Fernandes, G. D.; Aquino, A. J.; Tunega, D.; Pantoya, M. L. Regulating magnesium combustion using surface chemistry and heating rate. *Combustion and Flame* **2021**, *226*, 419-429.

(220) Zolotko, A.; Matsko, A.; Polishchuk, D.; Buinovskii, S.; Gaponenko, L. Ignition of a two-component gas suspension of metal particles. *Combustion, Explosion and Shock Waves* **1980**, *16* (1), 20-23.

(221) Kim, D. W.; Kim, K. T.; Kwon, G. H.; Song, K.; Son, I. Self-propagating heat synthetic reactivity of fine aluminum particles via spontaneously coated nickel layer. *Scientific Reports* **2019**, *9* (1), 1033.

(222) Jouet, R. J.; Warren, A. D.; Rosenberg, D. M.; Bellitto, V. J.; Park, K.; Zachariah, M. R. Surface passivation of bare aluminum nanoparticles using perfluoroalkyl carboxylic acids. *Chemistry of Materials* **2005**, *17* (11), 2987-2996.

(223) Kaplowitz, D. A.; Jian, G.; Gaskell, K.; Ponce, A.; Shang, P.; Zachariah, M. R. Aerosol synthesis and reactivity of thin oxide shell aluminum nanoparticles via fluorocarboxylic acid functional coating. *Particle & Particle Systems Characterization* **2013**, *30* (10), 881-887.

(224) Guan, F.-y.; Ren, H.; Zhao, W.-j.; Wu, X.-z.; Jiao, Q.-j. Novel aluminum-based fuel: Facile preparation to improve thermal reactions. *Defence Technology* **2022**, *18* (10), 1852-1862.

(225) Jiang, Y.; Wang, Y.; Baek, J.; Wang, H.; Gottfried, J. L.; Wu, C.-C.; Shi, X.; Zachariah, M. R.; Zheng, X. Ignition and combustion of Perfluoroalkyl-functionalized aluminum nanoparticles and nanothermite. *Combustion and Flame* **2022**, *242*, 112170.

(226) Ali, R.; Ali, F.; Zahoor, A.; Shahid, R. N.; Tariq, N. U. H.; Ali, G.; Ullah, S.; Shah, A.; Awais, H. B. Preparation and oxidation of aluminum powders with surface alumina replaced by iron coating. *Journal of Energetic Materials* **2022**, *40* (3), 243-257.

(227) ZHANG, S.-h. Coating of magnesium powder by rapid expansion of supercritical solution method. *Transactions of Nonferrous Metals Society of China* **2006**, *16*, s285-s288.

(228) Hastings, D.; Schoenitz, M.; Ryan, K. M.; Dreizin, E. L.; Krumpfer, J. W. Stability and Ignition of a Siloxane-Coated Magnesium Powder. *Propellants, Explosives, Pyrotechnics* **2020**, *45* (4), 621-627.

(229) Woodard, A.; Xu, L.; Barragan, A. A.; Nava, G.; Wong, B. M.; Mangolini, L. On the non-thermal plasma synthesis of nickel nanoparticles. *Plasma Processes and Polymers* **2018**, *15* (1), 1700104.

(230) Schwan, J.; Wagner, B.; Kim, M.; Mangolini, L. Controlled growth of silicon particles via plasma pulsing and their application as battery material. *Journal of Physics D: Applied Physics* **2021**, *55* (9), 094002.

(231) Barragan, A. A.; Hanukovich, S.; Bozhilov, K.; Yamijala, S. S.; Wong, B. M.; Christopher, P.; Mangolini, L. Photochemistry of plasmonic titanium nitride nanocrystals. *The Journal of Physical Chemistry C* **2019**, *123* (35), 21796-21804.

(232) Cech, V.; Branecky, M. Nonthermal tetravinylsilane plasma used for thin-film deposition: Plasma chemistry controls thin-film chemistry. *Plasma Processes and Polymers* **2022**, *19* (4), 2100192.

(233) Thimsen, E.; Johnson, M.; Zhang, X.; Wagner, A. J.; Mkhoyan, K. A.; Kortshagen, U. R.; Aydil, E. S. High electron mobility in thin films formed via supersonic impact deposition of nanocrystals synthesized in nonthermal plasmas. *Nature communications* **2014**, *5* (1), 5822.

(234) Liston, E.; Martinu, L.; Wertheimer, M. R. Plasma surface modification of polymers for improved adhesion: a critical review. *Journal of adhesion science and technology* **1993**, *7* (10), 1091-1127.

(235) Gu, M.; Kilduff, J. E.; Belfort, G. High throughput atmospheric pressure plasma-induced graft polymerization for identifying protein-resistant surfaces. *Biomaterials* **2012**, *33* (5), 1261-1270.

(236) He, W.; Guo, Z.; Pu, Y.; Yan, L.; Si, W. Polymer coating on the surface of zirconia nanoparticles by inductively coupled plasma polymerization. *Applied physics letters* **2004**, *85* (6), 896-898.

(237) Anthony, R. J.; Rowe, D. J.; Stein, M.; Yang, J.; Kortshagen, U. Routes to Achieving High Quantum Yield Luminescence from Gas-Phase-Produced Silicon Nanocrystals. *Advanced functional materials* **2011**, *21* (21), 4042-4046.

(238) Kortshagen, U.; Bhandarkar, U. Modeling of particulate coagulation in low pressure plasmas. *Physical Review E* **1999**, *60* (1), 887.

(239) Matsoukas, T.; Russell, M. Particle charging in low-pressure plasmas. *Journal of Applied Physics* **1995**, *77* (9), 4285-4292.

(240) Graves, D.; Daugherty, J.; Kilgore, M.; Porteous, R. Charging, transport and heating of particles in radiofrequency and electron cyclotron resonance plasmas. *Plasma Sources Science and Technology* **1994**, *3* (3), 433.

(241) Yasar-Inceoglu, O.; Zhong, L.; Mangolini, L. Core/shell silicon/polyaniline particles via in-flight plasma-induced polymerization. *Journal of Physics D: Applied Physics* **2015**, *48* (31), 314009.

(242) Chaukulkar, R. P.; Peuter, K. d.; Stradins, P.; Pylypenko, S.; Bell, J. P.; Yang, Y.; Agarwal, S. Single-step plasma synthesis of carbon-coated silicon nanoparticles. *ACS applied materials & interfaces* **2014**, *6* (21), 19026-19034.

(243) Berrospe Rodriguez, C.; Alvarez Barragan, A.; Nava, G.; Exarhos, S.; Mangolini, L. Stabilizing the plasmonic response of titanium nitride nanocrystals with a silicon oxynitride shell: Implications for refractory optical materials. *ACS Applied Nano Materials* **2020**, *3* (5), 4504-4511.

(244) Coleman, D.; Mangolini, L. Plasmonic core–shell silicon carbide–graphene nanoparticles. *ACS omega* **2019**, *4* (6), 10089-10093.

(245) Rajput, N. Methods of preparation of nanoparticles-a review. *International Journal of Advances in Engineering & Technology* **2015**, *7* (6), 1806.

(246) Zhou, L.; Piekiel, N.; Chowdhury, S.; Zachariah, M. R. T-Jump/time-of-flight mass spectrometry for time-resolved analysis of energetic materials. *Rapid Communications in Mass Spectrometry: An International Journal Devoted to the Rapid Dissemination of Up-to-the-Minute Research in Mass Spectrometry* **2009**, *23* (1), 194-202.

(247) Biswas, P.; Xu, F.; Ghildiyal, P.; Zachariah, M. R. In-situ thermochemical shock-induced stress at the metal/oxide interface enhances reactivity of aluminum nanoparticles. *ACS Applied Materials & Interfaces* **2022**, *14* (23), 26782-26790.

(248) DeLisio, J. B.; Hu, X.; Wu, T.; Egan, G. C.; Young, G.; Zachariah, M. R. Probing the reaction mechanism of aluminum/poly (vinylidene fluoride) composites. *The Journal of Physical Chemistry B* **2016**, *120* (24), 5534-5542.

(249) Ringe, E. Shapes, plasmonic properties, and reactivity of magnesium nanoparticles. *The Journal of Physical Chemistry C* **2020**, *124* (29), 15665-15679.

(250) Raffi, M.; Rumaiz, A. K.; Hasan, M.; Shah, S. I. Studies of the growth parameters for silver nanoparticle synthesis by inert gas condensation. *Journal of Materials Research* **2007**, *22* (12), 3378-3384.

(251) Sun, Y.; Feldman, A.; Farabaugh, E. X-ray photoelectron spectroscopy of O 1s and Si 2p lines in films of SiOx formed by electron beam evaporation. *Thin Solid Films* **1988**, *157* (2), 351-360.

(252) Burke, P. J.; Bayindir, Z.; Kipouros, G. J. X-ray photoelectron spectroscopy (XPS) investigation of the surface film on magnesium powders. *Applied spectroscopy* **2012**, *66* (5), 510-518.

(253) Mishra, I.; Majumder, S.; Joshi, S. R.; Subudhi, U.; Varma, S. Integrated X-ray photoelectron spectroscopy and DFT investigations of DNA adsorption on nanostructured SiOx surface. *Chemical Physics* **2022**, *562*, 111665.

(254) Tsuboi, Y.; Ura, S.; Takahiro, K.; Henmi, T.; Okada, A.; Wakasugi, T.; Kadono, K. Magnesiothermic reduction of silica glass substrate—Chemical states of silicon in the generated layers. *Journal of Asian Ceramic Societies* **2017**, *5* (3), 341-349.

(255) Khairallah, F.; Glisenti, A. XPS study of MgO nanopowders obtained by different preparation procedures. *Surface Science Spectra* **2006**, *13* (1), 58-71.

(256) Rehwoldt, M. C.; Wang, Y.; Xu, F.; Ghildiyal, P.; Zachariah, M. R. High-temperature interactions of metal oxides and a PVDF binder. *ACS Applied Materials & Interfaces* **2022**, *14* (7), 8938-8946.

(257) Wang, X.; Wu, T.; Wang, H.; DeLisio, J. B.; Yang, Y.; Zachariah, M. R. Boron ignition and combustion with doped δ-Bi2O3: Bond energy/oxygen vacancy relationships. *Combustion and Flame* **2018**, *197*, 127-133.

(258) Jung, I.-H.; Kang, D.-H.; Park, W.-J.; Kim, N. J.; Ahn, S. Thermodynamic modeling of the Mg–Si–Sn system. *Calphad* **2007**, *31* (2), 192-200.

(259) Cordova, S.; Shafirovich, E. Combustion synthesis of nanocrystalline silicon from silica and magnesium silicide. *Materials Chemistry and Physics* **2020**, *254*, 123288.

(260) Zhang, B.; Wang, F.; Chen, J.; Li, B.; Liu, K.; Han, Q. A Study on the Heat Effect during Magnesiothermic Reduction of Porous SiO 2. *Silicon* **2022**, 1-8.

(261) Zakaryan, M.; Aydinyan, S.; Kharatyan, S. Preparation of fine-grained silicon from serpentine mineral by magnesiothermic reduction of silica in the presence of reaction products as diluents. *Silicon* **2017**, *9*, 841-846.

(262) Faraji, M.; Adeli, M.; Soltanieh, M. Efficient production of magnesium silicide from elemental powders by combustion synthesis. *Ceramics International* **2021**, *47* (2), 2822-2827. DOI: https://doi.org/10.1016/j.ceramint.2020.09.136.

(263) Su, X.; Fu, F.; Yan, Y.; Zheng, G.; Liang, T.; Zhang, Q.; Cheng, X.; Yang, D.; Chi, H.; Tang, X.; et al. Self-propagating high-temperature synthesis for compound thermoelectrics and new criterion for combustion processing. *Nature Communications* **2014**, *5* (1), 4908. DOI: 10.1038/ncomms5908.

(264) Darghouth, A.; Aouida, S.; Bessais, B. High Purity Porous Silicon Powder Synthesis by Magnesiothermic Reduction of Tunisian Silica Sand. *Silicon* **2021**, *13* (3), 667-676. DOI: 10.1007/s12633-020-00433-1.

(265) Matsubara, K.; Shiomi, H.; Shiono, T.; Okada, A.; Wakasugi, T.; Kadono, K. Porous silicon prepared from monolithic porous silica glass using a two-step magnesiothermic reduction. *International Journal of Ceramic Engineering & Science* **2020**, *2* (6), 310-319. DOI: https://doi.org/10.1002/ces2.10069 (acccessed 2024/08/28).

(266) Mahadevan, R.; Lee, D.; Sakurai, H.; Zachariah, M. R. Measurement of Condensed-Phase Reaction Kinetics in the Aerosol Phase Using Single Particle Mass Spectrometry. *The Journal of Physical Chemistry A* **2002**, *106* (46), 11083-11092. DOI: 10.1021/jp025784c.

(267) Yokota, T.; Murayama, M.; Howe, J. M. In situ Transmission-Electron-Microscopy Investigation of Melting in Submicron Al-Si Alloy Particles under Electron-Beam Irradiation. *Physical Review Letters* **2003**, *91* (26), 265504. DOI: 10.1103/PhysRevLett.91.265504.

(268) Calizzi, M.; Venturi, F.; Ponthieu, M.; Cuevas, F.; Morandi, V.; Perkisas, T.; Bals, S.; Pasquini, L. Gas-phase synthesis of Mg–Ti nanoparticles for solid-state hydrogen storage. *Physical Chemistry Chemical Physics* **2016**, *18* (1), 141-148.

(269) Zhang, X.; Liu, Y.; Zhang, X.; Hu, J.; Gao, M.; Pan, H. Empowering hydrogen storage performance of MgH2 by nanoengineering and nanocatalysis. *Materials Today Nano* **2020**, *9*, 100064.

(270) Sadhasivam, T.; Kim, H.-T.; Jung, S.; Roh, S.-H.; Park, J.-H.; Jung, H.-Y. Dimensional effects of nanostructured Mg/MgH2 for hydrogen storage applications: a review. *Renewable and Sustainable Energy Reviews* **2017**, *72*, 523-534.

(271) Ismail, M. Effect of LaCl3 addition on the hydrogen storage properties of MgH2. *Energy* **2015**, *79*, 177-182.

(272) Maggi, F.; Gariani, G.; Galfetti, L.; DeLuca, L. T. Theoretical analysis of hydrides in solid and hybrid rocket propulsion. *international journal of hydrogen energy* **2012**, *37* (2), 1760-1769.

(273) Nanda, S.; Vo, D.-V. N.; Tri, P. N. *New dimensions in production and utilization of hydrogen*; Elsevier, 2020.

(274) Xi, J.; Liu, J.; Wang, Y.; Liang, D.; Zhou, J. Effect of metal hydrides on the burning characteristics of boron. *Thermochimica Acta* **2014**, *597*, 58-64.

(275) Fang, H.; Deng, P.; Liu, R.; Han, K.; Zhu, P.; Nie, J.; Guo, X. Energy-releasing properties of metal hydrides (MgH2, TiH2 and ZrH2) with molecular perovskite energetic material DAP-4 as a novel oxidant. *Combustion and Flame* **2023**, *247*, 112482.

(276) Young, G.; Piekiel, N.; Chowdhury, S.; Zachariah, M. Ignition behavior of α-AlH3. *Combustion science and technology* **2010**, *182* (9), 1341-1359.

(277) Zaluska, A.; Zaluski, L.; Ström–Olsen, J. Nanocrystalline magnesium for hydrogen storage. *Journal of Alloys and Compounds* **1999**, *288* (1-2), 217-225.

(278) Wu, J.-x.; Liu, Q.; Feng, B.; Yin, Q.; Li, Y.-c.; Wu, S.-z.; Yu, Z.-s.; Huang, J.-y.; Ren, X.-x. Improving the energy release characteristics of PTFE/Al by doping magnesium hydride. *Defence Technology* **2022**, *18* (2), 219-228.

(279) Perez, J. P. L.; McMahon, B. W.; Yu, J.; Schneider, S.; Boatz, J. A.; Hawkins, T. W.; McCrary, P. D.; Flores, L. A.; Rogers, R. D.; Anderson, S. L. Boron Nanoparticles with High Hydrogen Loading: Mechanism for B–H Binding and Potential for Improved Combustibility and Specific Impulse. *ACS Applied Materials & Interfaces* **2014**, *6* (11), 8513-8525.

(280) Young, G.; Wang, H.; Zachariah, M. R. Application of nano-aluminum/nitrocellulose mesoparticles in composite solid rocket propellants. *Propellants, Explosives, Pyrotechnics* **2015**, *40* (3), 413-418.

(281) Mulamba, O.; Hunt, E. M.; Pantoya, M. L. Neutralizing bacterial spores using halogenated energetic reactions. *Biotechnology and bioprocess engineering* **2013**, *18*, 918-925.

(282) Zhang, Q.; Huang, Y.; Ma, T.; Li, K.; Ye, F.; Wang, X.; Jiao, L.; Yuan, H.; Wang, Y. Facile synthesis of small MgH2 nanoparticles confined in different carbon materials for hydrogen storage. *Journal of Alloys and Compounds* **2020**, *825*, 153953.

(283) Paskevicius, M.; Sheppard, D. A.; Buckley, C. E. Thermodynamic changes in mechanochemically synthesized magnesium hydride nanoparticles. *Journal of the American chemical Society* **2010**, *132* (14), 5077-5083.

(284) Porcheddu, A.; Cincotti, A.; Delogu, F. Kinetics of MgH2 formation by ball milling. *International Journal of Hydrogen Energy* **2021**, *46* (1), 967-973.

(285) Ouyang, L.; Cao, Z.; Wang, H.; Hu, R.; Zhu, M. Application of dielectric barrier discharge plasma-assisted milling in energy storage materials–a review. *Journal of Alloys and Compounds* **2017**, *691*, 422-435.

(286) Li, Z.-Y.; Sun, Y.-J.; Zhang, C.-C.; Wei, S.; Zhao, L.; Zeng, J.-L.; Cao, Z.; Zou, Y.-J.; Chu, H.-L.; Xu, F. Optimizing hydrogen ad/desorption of Mg-based hydrides for energy-storage applications. *Journal of Materials Science & Technology* **2023**, *141*, 221-235.

(287) Klopčič, N.; Grimmer, I.; Winkler, F.; Sartory, M.; Trattner, A. A review on metal hydride materials for hydrogen storage. *Journal of Energy Storage* **2023**, *72*, 108456.

(288) Song, M.; Zhang, L.; Wu, F.; Zhang, H.; Zhao, H.; Chen, L.; Li, H. Recent advances of magnesium hydride as an energy storage material. *Journal of Materials Science & Technology* **2023**, *149*, 99-111.

(289) Ouyang, L.; Cao, Z.; Wang, H.; Liu, J.; Sun, D.; Zhang, Q.; Zhu, M. Enhanced dehydriding thermodynamics and kinetics in Mg (In)–MgF2 composite directly synthesized by plasma milling. *Journal of alloys and compounds* **2014**, *586*, 113-117.

(290) Dan, L.; Wang, H.; Liu, J.; Ouyang, L.; Zhu, M. H2 plasma reducing Ni nanoparticles for superior catalysis on hydrogen sorption of MgH2. *ACS Applied Energy Materials* **2022**, *5* (4), 4976-4984.

(291) Le-Quoc, H.; Lacoste, A.; Miraglia, S.; Béchu, S.; Bès, A.; Laversenne, L. MgH2 thin films deposited by one-step reactive plasma sputtering. *International journal of hydrogen energy* **2014**, *39* (31), 17718-17725.

(292) Le-Quoc, H.; Coste, M.; Lacoste, A.; Laversenne, L. Magnesium hydride films deposited on flexible substrates: Structure, morphology and hydrogen sorption properties. *Journal of Alloys and Compounds* **2023**, *955*, 170272.

(293) Izadi, A.; Anthony, R. J. A plasma-based gas-phase method for synthesis of gold nanoparticles. *Plasma Processes and Polymers* **2019**, *16* (7), e1800212.

(294) Loh, K. Q.; Andaraarachchi, H. P.; Ferry, V. E.; Kortshagen, U. R. Photoluminescent Si/SiO2 Core/Shell Quantum Dots Prepared by High-Pressure Water Vapor Annealing for Solar Concentrators, Light-Emitting Devices, and Bioimaging. *ACS Applied Nano Materials* **2023**, *6* (7), 6444-6453.

(295) Beaudette, C. A.; Andaraarachchi, H. P.; Wu, C.-C.; Kortshagen, U. R. Inductively coupled nonthermal plasma synthesis of aluminum nanoparticles. *Nanotechnology* **2021**, *32* (39), 395601.

(296) Uner, N. B.; Thimsen, E. Nonequilibrium plasma aerotaxy of size controlled GaN nanocrystals. *Journal of Physics D: Applied Physics* **2019**, *53* (9), 095201.

(297) Uner, N. B.; Thimsen, E. In-flight size focusing of aerosols by a low temperature plasma. *The Journal of Physical Chemistry C* **2017**, *121* (23), 12936-12944.

(298) Borgschulte, A.; Bösenberg, U.; Barkhordarian, G.; Dornheim, M.; Bormann, R. Enhanced hydrogen sorption kinetics of magnesium by destabilized MgH2− δ. *Catalysis Today* **2007**, *120* (3-4), 262-269.

(299) *NIST Atomic Spectra Database (version 5.10)*. https://www.nist.gov/pml/atomic-spectra-database (accessed 01-20-2023).

(300) Hagelaar, G.; Pitchford, L. C. Solving the Boltzmann equation to obtain electron transport coefficients and rate coefficients for fluid models. *Plasma sources science and technology* **2005**, *14* (4), 722.

(301) Tatarova, E.; Dias, F. M.; Gordiets, B.; Ferreira, C. M. Molecular dissociation in N2–H2 microwave discharges. *Plasma Sources Science and Technology* **2005**, *14* (1), 19. DOI: 10.1088/0963-0252/14/1/003.

(302) Yamijala, S. S. R. K. C.; Nava, G.; Ali, Z. A.; Beretta, D.; Wong, B. M.; Mangolini, L. Harnessing Plasma Environments for Ammonia Catalysis: Mechanistic Insights from Experiments and Large-Scale Ab Initio Molecular Dynamics. *The Journal of Physical Chemistry Letters* **2020**, *11* (24), 10469-10475. DOI: 10.1021/acs.jpclett.0c03021.

(303) Hagelaar, G. J. M.; Pitchford, L. C. Solving the Boltzmann equation to obtain electron transport coefficients and rate coefficients for fluid models. *Plasma Sources Science and Technology* **2005**, *14* (4), 722. DOI: 10.1088/0963-0252/14/4/011.

(304) BSR Database. (acccessed 01-20-2023).

(305) IST-Lisbon database. (acccessed 01-20-2023).

(306) Itikawa database. (acccessed 01-20-2023).

(307) Mosbach, T. Population dynamics of molecular hydrogen and formation of negative hydrogen ions in a magnetically confined low temperature plasma. *Plasma Sources Science and Technology* **2005**, *14* (3), 610.

(308) Sabat, K. C.; Murphy, A. B. Hydrogen plasma processing of iron ore. *Metallurgical and Materials Transactions B* **2017**, *48* (3), 1561-1594.

(309) Celiberto, R.; Janev, R.; Laricchiuta, A.; Capitelli, M.; Wadehra, J.; Atems, D. Cross section data for electron-impact inelastic processes of vibrationally excited molecules of hydrogen and its isotopes. *Atomic Data and Nuclear Data Tables* **2001**, *77* (2), 161-213.

(310) Tao, S.; Notten, P.; Van Santen, R.; Jansen, A. Density functional theory studies of the hydrogenation properties of Mg and Ti. *Physical Review B—Condensed Matter and Materials Physics* **2009**, *79* (14), 144121.

(311) Thornton, J. A. Magnetron sputtering: basic physics and application to cylindrical magnetrons. *Journal of Vacuum Science and Technology* **1978**, *15* (2), 171-177.

(312) Gatti, M.; Kortshagen, U. Analytical model of particle charging in plasmas over a wide range of collisionality. *Physical Review E—Statistical, Nonlinear, and Soft Matter Physics* **2008**, *78* (4), 046402.

(313) Coleman, D.; Lopez, T.; Yasar-Inceoglu, O.; Mangolini, L. Hollow silicon carbide nanoparticles from a non-thermal plasma process. *Journal of Applied Physics* **2015**, *117* (19).

(314) Kramer, N.; Anthony, R.; Mamunuru, M.; Aydil, E.; Kortshagen, U. Plasma-induced crystallization of silicon nanoparticles. *Journal of Physics D: Applied Physics* **2014**, *47* (7), 075202.

(315) Gulbransen, E. A. The Oxidation and Evaporation of Magnesium at Temperatures from 400 to 500 C. *Transactions of the Electrochemical Society* **1945**, *87* (1), 589.

(316) Mangolini, L.; Kortshagen, U. Selective nanoparticle heating: Another form of nonequilibrium in dusty plasmas. *Physical Review E* **2009**, *79* (2), 026405. DOI: 10.1103/PhysRevE.79.026405.

(317) Shao, H.; Wang, Y.; Xu, H.; Li, X. Hydrogen storage properties of magnesium ultrafine particles prepared by hydrogen plasma-metal reaction. *Materials Science and Engineering: B* **2004**, *110* (2), 221-226. DOI: https://doi.org/10.1016/j.mseb.2004.03.013.

(318) Xie, L.; Liu, Y.; Wang, Y. T.; Zheng, J.; Li, X. G. Superior hydrogen storage kinetics of MgH2 nanoparticles doped with TiF3. *Acta Materialia* **2007**, *55* (13), 4585-4591. DOI: https://doi.org/10.1016/j.actamat.2007.04.020.

(319) Bösenberg, U.; Ravnsbæk, D. B.; Hagemann, H.; D'Anna, V.; Minella, C. B.; Pistidda, C.; van Beek, W.; Jensen, T. R.; Bormann, R.; Dornheim, M. Pressure and Temperature Influence on the Desorption Pathway of the LiBH4−MgH2 Composite System. *The Journal of Physical Chemistry C* **2010**, *114* (35), 15212-15217. DOI: 10.1021/jp104814u.